COMMUNICATIONS

Dear reader,

The current volume of the journal Communications is focused on physical research and its applications to material investigation for a broad spectrum of technological fields.

The scientific-research activities of the physicists of Zilina University are oriented into two basic fields of physics. Traditionally, one group of the physicists is concerned with the utilization of acoustic methods for the investigation of condensed matter. Currently a wide range of ultrasonic techniques utilizing also the acoustoelectric and acousto-optic phenomena is used to investigate semiconductors, metals, ferroelectrics and magnetic liquids as well as new ultrasonic techniques are developed. The second group studies physical properties of conventional telecommunication optic fibres, twin core optic fibres, photonic crystal fibres, biological photonic structures, semiconductor structures and semiconductor laser diodes based on quantum wells using optical techniques. Self-diffraction of light in magnetic fluids and photorefractive phenomenon in selected condensed matter materials are also studied within the group. In spite of the fact that most of these activities are carried out within intro-basic research they represent actually the application of physical methods and physical phenomena in materials research orientated mostly on materials, structures and devices for electronic and electrical engineering. However, in recent years the research programme has been extended to theoretical high-energy physics. One research group works in the area of electroweak symmetry breaking.

We are grateful for the opportunity given by the editorial board of the Communications to present on the pages of the journal a part of results achieved by physicists, both from the Department of Physics at the Faculty of Electrical Engineering of Zilina University and some cooperating institutions. The papers provide evidence of mutual close interrelation between physical research and possible technical applications, thus fostering mutual communication between physics and technology.

Peter Bury

Ladislav Harmatha – Peter Valent – Juraj Racko *

DIELECTRIC PROPERTIES AND BREAKDOWN OF THE GATE OXIDE IN THE MOS STRUCTURE

The article treats the methodology of measuring the breakdown voltage on Si-based MOS structures. Identification of defects in the thin gate oxide is performed using the Weibull statistical analysis. By comparing the current and capacitance measurements on MOS structures we determined the influence of the defect charge in the oxide upon the parameters characterizing the breakdown. A higher occurrence of defects was correlated with elevated values of the flat band voltages. This verifies the hypothesis of an increased destruction of MOS structures caused by electrically active defects arising in the course of thermic oxidation and pre-oxidation treatment of the surface of silicon.

1. Introduction

In unipolar semiconductor technology, the preparation of a high quality gate insulating layer plays an important role. In silicon technology the thin SiO_2 layer is prepared by thermic oxidation. The properties of this insulating layer and of its interfaces with silicon affect the performance of unipolar devices and integrated circuits markedly [1].

The fundament of unipolar circuits is the MOS (Metal Oxide Semiconductor) structure. Its diagnostics is performed by current and capacitance methods [2]. The progress and utilization of theses methods determine the new trends in technology. The steep growth in the density of integration while keeping the performance parameters requires ever thinner SiO_2 layers. The properties of such thin layers strongly depend on the type and distribution of defects in the oxide. The defect charge in the oxide deteriorates the overall stability of MOS structures and increases the threshold and leakage currents. For eliminating these undesirable phenomena it is inevitable to know the type of defects and their electric activity.

The measurement of the breakdown voltage properly completes the analysis of defects in the oxide, and under certain measuring conditions and statistical evaluation of the measured data allows their identification.

We discuss the methodology of time independent measurement of the breakdown voltage (TZDB, Time Zero Dielectric Breakdown) employing the Weibull statistics for data evaluation. In accordance with the JEDEC Standard JESD35-A (Procedure for the Wafer-Level Testing of Thin Dielectrics) [3] the method is divided into the V-RAMP test (linear growth of the voltage and measurement of the current) and the J-RAMP test (exponential growth of the current and measurement of the voltage). The V-RAMP test is used to characterize defects in weak electric fields. On the other hand, the J-RAMP test is suitable for analysis of defects that manifest themselves in strong electric fields and for MOS structures with small areas of the gates.

The model of the electric breakdown of thin insulating layers becomes gradually more sophisticated. The first model believed that the cause of breakdown was impact ionization due to charge carriers injected from the gate electrode through the insulator into the substrate. A model followed of electron-hole generation in which the breakdown was assumed to be caused by a conductive channel consisting of high-density defects generated by the increased current of injected charge carriers. In this case one can also assume an effect of predominantly positive induced mobile ions in the insulating layer. The advanced model considers a simultaneous existence of several processes. The methodology of measuring the time dependent breakdown is suitable for their separation.

The latest knowledge on the breakdown mechanism of the insulating layer in the MOS structure are utilized in two models: thermo-chemical, the so-called linear *E*-model of the electric field [4], and the model of hole generation, the so-called reciprocal $1/E$ model of the electric field [5]. They assume that the electrons that can tunnel through the potential barrier of the insulating layer may induce a local increase of the electric field E in the layer. The places with a critical value of the electric field E_{cri} trigger the breakdown.

2. Measurement and Evaluation Methodology

For optimizing the methodology of measuring the breakdown voltage V_{BD} we used sample G00T with MOS structures containing a thin gate oxide layer. The N-type (100)-oriented silicon substrate had a resistivity of 2–5 Ωcm. The SiO_2 layer grown at a temper-

* **Ladislav Harmatha, Peter Valent, Juraj Racko**
Microelectronics Department, Faculty of Electrical Engineering and Information Technology, Slovak University of Technology, Bratislava, Slovakia, E-mail: ladislav.harmatha@stuba.sk

ature of 1050 °C in dry O_2 had a thickness of t_{OX} = 28 nm. Aluminium gates were sputter deposited and patterned photolithographically using a CV mask with various areas of the gates, A_G. The oxide was removed from the back side of the Si wafer and a good Al ohmic contact was sputter deposited. Finally, stabilizing annealing was performed in N_2+H_2 at 450 °C for 30 minutes. Figures 1a, b compare the two methods of breakdown measurement on the same wafer with MOS structures using the Keithley 237 instrument.

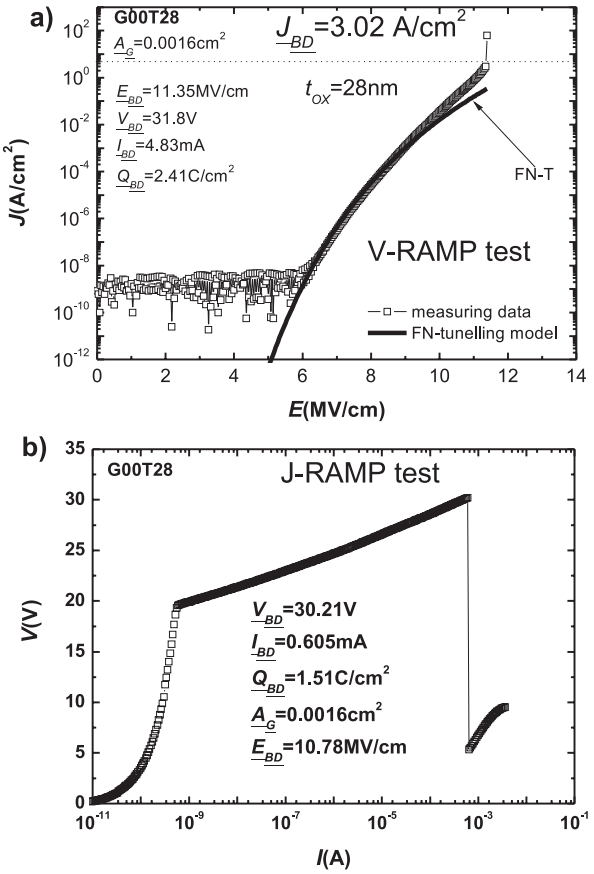

Fig. 1 Breakdown measurement: a) V-RAMP test, b) J-RAMP test

In the V-RAMP test, the measured values are given directly by a purpose written code. A voltage of such polarity is applied to the structure that brings it into accumulation and the current is measured that flows through the gate oxide. As long as breakdown does not occur, the charge accumulated in the oxide can be expressed as

$$Q_{BD} = \sum_{i=1}^{i=N} I_{meas}(i) t_{step}\,, \tag{1}$$

where I_{meas} is the current measured at the time step t_{step}, and N is the number of time steps prior to the breakdown. As a criterion of breakdown, such a current was used exceeds the value of

$$I_{BD} = 10 I_{exp}\,. \tag{2}$$

A typical value of I_{exp} is between 20 and 30 A/cm^2. If this current is too small, a breakdown need not occur at all. On the contrary, if I_{exp} is too large, the breakdown will not be detected because the series resistance of the structure begins to play a significant role that decreases the value of I_{BD}. The second criterion of breakdown is based on the change of the slope of the I-V curve. If the slope exceeds a certain (2 to 5-fold) value of the initial slope, one detects the breakdown.

In MOS structures with thermic SiO_2 one can assume the Fowler-Nordheim charge transport through the oxide. This model is applicable if the field intensity ranges from 6 to 10 MV/cm. The current density can be written as

$$J_{FN} = A E_{OX}^2 \exp\left(\frac{-B}{E_{ox}}\right) \tag{3}$$

where

$$A = \frac{q^3 (m/m_{OX})}{8\pi h} \frac{1}{\Phi_B} = 1.54 \times 10^{-6} \frac{m}{m_{OX}} \frac{1}{\Phi_B}\,, \tag{4}$$

$$B = \frac{8\pi\sqrt{2 m_{OX} \Phi_B^3}}{3qh} = 6.83 \times 10^7 \sqrt{\frac{m_{OX} \Phi_B^3}{m}}\,. \tag{5}$$

Here, m_{OX} is the effective mass of electrons in the oxide, m is the free electron mass and Φ_B is the barrier height at the Si/SiO_2 interface. Equation (3) can be written as

$$\ln\left(\frac{J_{EN}}{E_{OX}^2}\right) = \ln(A) - \frac{B}{E_{OX}} \tag{6}$$

whereby we get the Fowler-Nordheim formula $\ln(J_{FN}/E_{OX}^2) = = f(1/E_{OX})$. The barrier height Φ_B is obtained from the slope of the line fitted through the measured dependence.

For getting the characteristic breakdown parameters, statistical evaluation methods are used. This assumes a large set of measurements with acceptable uniformity of the parameters across the wafer. Problems may occur in the case of a small amount of measured structures on the wafer. The minimum number of measurements is 30.

The most often exploited method of statistical evaluation is the Weibull distribution. This is characterized by two functions, probability density function (PDF) and cumulative density function (CDS). We used the CDF that has the form

$$F(x) = 1 - \exp\left[-\left(\frac{x}{\theta}\right)^b\right]\,, \tag{7}$$

where θ is the characteristic time (scale parameter) and b is the Weibull slope (shape parameter). Formula (7) can be written as

$$\ln(-\ln(1 - F(x)) = b(\ln(x)) - b(\ln(\theta))\,, \tag{8}$$

which is the so-called Weibull graph, see Fig. 2. The change in the slope (b) of the curve allows to determine the nature of the break-

down. The extrinsic breakdown is caused by defects created during the technology (metallic impurities, vacancies, clusters),

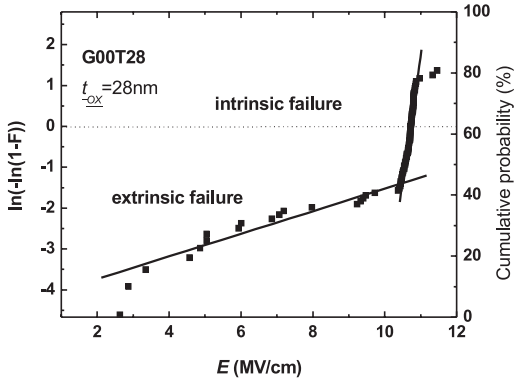

Fig. 2 The Weibull graph for sample G00T28

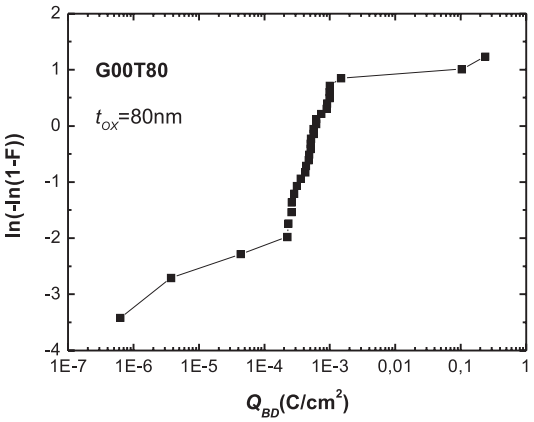

Fig. 3 Distribution of the accumulated charge displayed as a Weibull graph

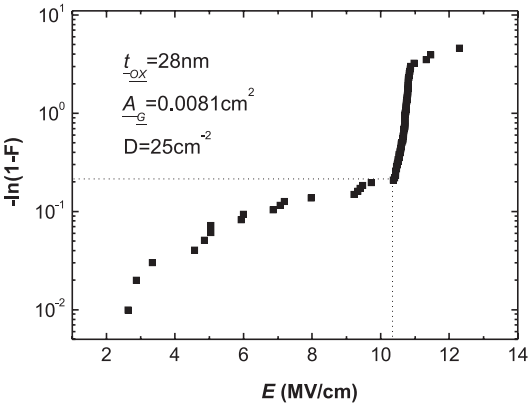

Fig. 4 Defectiveness in dependence on the field strength

intrinsic breakdown is due to primary defects inevitably created during thermic oxidation.

A useful parameter characterizing the breakdown is the accumulated charge Q_{BD} that can be shown graphically as in Fig. 3.

The distribution of the accumulated charge allows to detect those defects that are not seen in the graph showing the distribution of the electric field E_{BD}.

In unipolar technology the defectiveness in the wafer is regularly checked by measuring the breakdown voltage and statistical evaluation. For calculating the defectiveness the following formula is used:

$$F = 1 - \exp(-A_G D), \tag{8}$$

where A_G is the area of the MOS structure and D is the defectiveness. If we again rewrite function F into the form

$$-\ln(1 - F) = A_G D, \tag{9}$$

it is possible to construct the graph shown in Fig. 4. It allows to find the defectiveness at various field intensities. The defectiveness is often read at the kink of the curve between the intrinsic and extrinsic parts of defects.

3. Breakdown of MOS Structures with Various Flat Band Voltages

The effect of the defect charge of mobile ions and traps in the SiO_2 insulating layer and at the interfaces with the silicon substrate and the metallic gate of the MOS structure upon the breakdown voltage was observed on two series of samples. The first series (G00P) are MOS structures with a small value of the flat band voltage V_{FB}. In this case the density of defects in the oxide is low. The other series (G00R) are MOS structures with a large-scale value of V_{FB}, thus with a high density of defects in the oxide.

The MOS structures were prepared in the production as test samples, thus they might be contaminated in the course of Al gate sputtering. The SiO_2 gate oxide was created by thermic oxidation in O_2+HCl at a temperature of 1060 °C for 30 minutes. The substrate was N-type (100)-oriented silicon with resistivity from 2 to 5 Ωcm. After sputter depositing the back Al ohmic contact the structures were annealed in N_2+H_2 at 450 °C for 30 minutes.

The quality of MOS structures was checked by C–V measurements. The concentration of impurities N_{sub} and the total density of defect charge N_{eff} were determined from the flat band voltage V_{FB}. Figure 5 shows the high-frequency C–V curves of G00P and G00R samples.

The MOS structures of G00R sample have a high negative value of the flat band voltage ($V_{FB} = -2$ V). The total defect charge was positive with a high density, $N_{eff} = 5.3\times10^{11}$ cm^{-2}. High quality MOS structures of G00P sample have a flat band voltage $V_{FB} = -0.1$ V, which is related to the low total positive defect density, $N_{eff} = 2.4\times1010$ cm^{-2}.

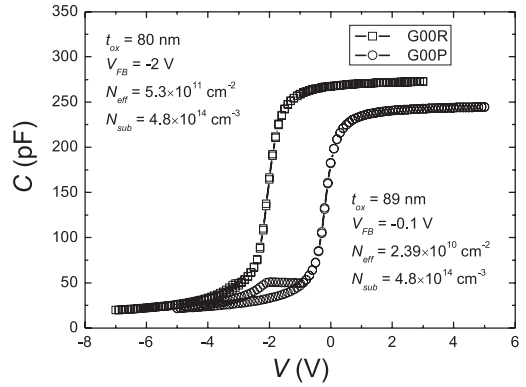

Fig. 5 Voltage dependence of the capacitance of MOS structures with various values of the flat band voltage.

The influence of the defect charge in the oxide was assessed by measuring the breakdown voltage and evaluating the data by the Weibull statistics. In Fig. 6 one can distinguish the extrinsic region characterized by defect that had been created in the process of Si surface treatment and during thermic oxidation. These include mainly metallic impurities, traps in the bulk and mobile ions that accelerate creation of a conductive path through the oxide. In this case we observed breakdowns at field intensities up to 9 MV/cm for sample G00P and 9.3 MV/cm for sample G00R.

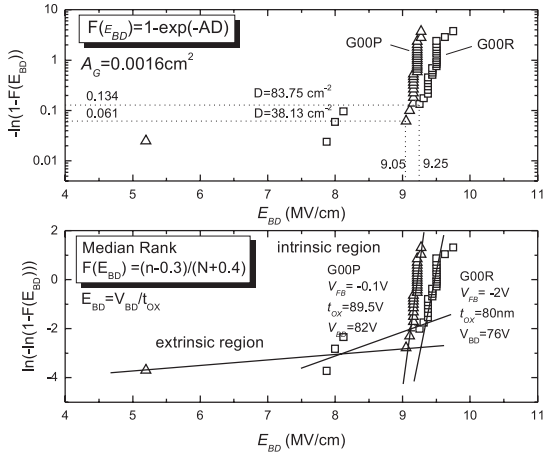

Fig. 6 Weibull distribution of the measured breakdowns expressing the defectiveness D, and classifying the defects into intrinsic and extrinsic

For the intrinsic region, breakdowns are typical due to breaking the oxygen-silicon bonds. Such traps contained in the bulk of SiO_2 and at the SiO_2/Si interface are electrically active generation-recombination centres. By means of these traps a sharp increase in the magnitude of current occurs, up to a breakdown [6].

From the Weibull analysis (Fig. 6) we deter-mined the defectiveness 33 cm^{-2} for sample G00P and 89 cm^{-2} for sample G00R.

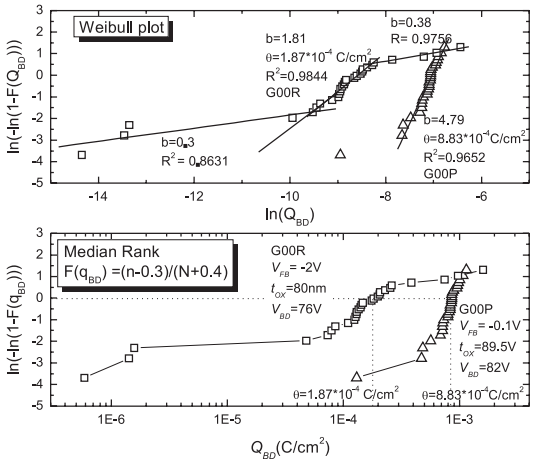

Fig. 7 Weibull distribution of the measured breakdowns allowing to identify the type of defects from the shape and value of the cumulative charge

The values were evaluated for the kink on the curve, where the extrinsic region changes into the intrinsic region.

Applying the Weibull analysis, the slope of the curve was found to be $b = 1.81$ for sample G00R and $b = 4.79$ for sample G00P with characteristic charge values $\theta = 1.87\times10^{-4}$ C/cm^2 (G00R) and $\theta = 8.83\times10^{-4}$ C/cm^2 (G00P). The slope expresses the type of defects taking part in the breakdown. The slope below 2 is typical for a breakdown caused by defects having their origin in the production (traps in the bulk of SiO_2, metallic impurities). This type of defects was detected in sample G00R. If the slope is larger than 2, it suggests defects caused by rapid wear out or fatigue of the material. In the case of breakdowns of the insulating layer, such defects can be classified in the intrinsic region. A steeper curve (smaller dispersion of the measured parameters) means a higher quality of the oxide. The Weibull analysis of the insulating layer allows to conclude that SiO_2 in sample G00P is of higher quality in comparison with that in sample G00R, as confirmed also by capacitance measurements. The MOS structures with a large defect charge (G00R) exhibited a lower quality also from the point of view of the breakdown voltage.

3. Conclusion

In semiconductor industry, the quality of the gate SiO_2 oxide in the MOS structure is checked by measuring the breakdown voltage and by capacitance methods. It has been proved that a large change of the defect charge measured by capacitance techniques does not mean a marked variation in the breakdown voltage. The Weibull analysis, however, allows to identify the type of defects and their non-uniform distribution on the wafer. Good correlation between capacitance and current measurement was not achieved before the type of defects had been determined. The samples with high values of the flat band voltage, thus with a large defect charge in the oxide exhibited also a high defectiveness. Such wafers do

not reach a satisfactory quality required for the unipolar CMOS technology.

Acknowledgement

This work has been conducted in the Centre of Excellence CENAMOST (Slovak Research and Development Agency Contract No. VVCE-0049-07) and supported by grant VEGA 1/0507/09 and VEGA 1/0601/10 of the Ministry of Education of the Slovak Republic.

References

[1] NICOLLIAN, E. H., BREWS, J. R.: *MOS (Metal Oxide Semiconductor) Physics and Technology*, Wiley, New York, 1982.
[2] SCHRODER, D. K.: *Semiconductor Material and Device Characterization*, New York, Wiley, 1998.
[3] *https://www.jedec.org*
[4] McPHERSON, J. W., MOGUL, H. C.: *Underlying Physics of the Thermo-chemical E Model in Describing Low-field Time Dependent Dielectrics Breakdown in* SiO_2 *Thin Films,* J. of Applied Physics, Vol. 84, 1998, pp. 1513–1523.
[5] KIMURA, M., KOYAMA, H.: *Mechanism of Time Dependent Oxide Breakdown in Thin Thermally Grown* SiO_2 *Films*, J. of Applied Physics, Vol.85, 1999, pp. 7671–7681
[6] RACKO, J., GRMANOVÁ, A., HARMATHA, L., BREZA, J., DONOVAL, D., SCHWIERZ, F., GRANZNER, R., FROHLICH, K.: *Traps Assisted Tunnelling Current in MIM Structures,* Proc. of EDS´09, Electronic Devices and Systems. IMAPS CS Intern. Conference 2009, Brno, Czech Republic, 2009, pp. 111–116 .

Ivan Martincek – Dusan Pudis *

A THEORETICAL STUDY OF THE TEMPERATURE SENSOR BASED ON THE LP_{01}–LP_{02} INTERMODAL INTERFERENCE IN OPTICAL FIBER WITH A LIQUID CORE

We theoretically propose the temperature sensor based on optical fiber consisting of fused silica and core of 2.5 μm radius filled in with toluene. In such an optical fiber the intermodal interference of modes LP_{01}-LP_{02} shows a characteristic dependence of the equalization wavelength λ_0 on temperature. The optical fiber sensor was theoretically investigated in the temperature range of 0–40 °C, where the equalization wavelength λ_0 for modes LP_{01}-LP_{02} changes from 1284.2 nm to 844.1 nm. Such considerable wavelength change with temperature favors this sensor for temperature measurements with sensitivity better than 0.1 °C.

1. Introduction

Various detection methods of physical quantities employ optical fibers where typical dependence of intensity, wavelength or phase of a propagating electromagnetic radiation on a measured physical quantity is monitored. Different devices have been proposed for the measurement of a large number of physical parameters including temperature, acoustic, electric and magnetic fields, pressure, strain rotation, displacement, etc.

A subset of group of optical fiber sensors is represented by sensors which use intermodal interference of propagating modes of electromagnetic radiation. The most attractive from this group are sensors using intermodal interference of fundamental mode LP_{01} and first higher order mode LP_{11} which propagate in optical fibers with an elliptical core. Various sensors of pressure, temperature and distributed strain based on interference of presented modes were published [1, 2].

Another group of optical fiber sensors based on intermodal interference typically uses interference of modes LP_{01} a LP_{02} propagating in a cylindrical optical fiber. From this group of optical fiber sensors were published sensors of acoustics waves, fiber elongation, longitudinal strain, temperature and hydrostatic pressure [3, 4, 5].

Hollow-core optical fibers belong to a special class of optical fibers with an air core surrounded by a higher refractive index material. A hollow-core optical fiber filled with certain kinds of liquids forms the liquid-core optical fiber.

In this paper an exploitation of intermodal interference between LP_{01} and LP_{02} modes in a liquid-core optical fiber for temperature measurement is theoretically described. We suppose the hollow-core optical fiber with a fused silica cladding and a core filled with toluene. In such a liquid-core optical fiber the waveguide properties are sensitive to temperature due to a different thermal coefficient of a refractive index core and cladding. It can be used for sensing applications where the intermodal interference of defined modes is measured in a wide temperature range.

2. Theoretical approach

Light in an optical fiber propagates by means of modes of electromagnetic fields. An individual mode propagates with a phase constant β which depends on parameters of an optical fiber and can be different for individual modes. The difference between phase constants allows for observation of intermodal interference under special conditions.

The interference signal s for monochromatic light detected at the end of an optical fiber is in the case of two-mode interference proportional to term [6]

$$s \approx \cos[(\beta_m - \beta_n)l], \tag{1}$$

where l is the length of optical fiber and β_m, β_n are the phase constants of the individual interfering modes. For the cylindrical optical fiber the phase constant of the mth mode can be expressed as [6]

$$\beta_m = \frac{2\pi}{\lambda}\sqrt{n_{co}^2 - \frac{U_m^2(V)}{V^2}\left(n_{co}^2 - n_{cl}^2\right)}\,, \tag{2}$$

* **Ivan Martincek, Dusan Pudis**
Department of Physics, Faculty of Electrical Engineering, University of Zilina, E-mail: ivmar@fel.uniza.sk

where λ is the wavelength of light in vacuum, n_{co} and n_{cl} are maximal and minimal refractive indices of the core and cladding of optical fiber, U_m is the normalized propagation constant in the transverse direction of the mth mode and V is the normalized frequency defined by [7]

$$V = \frac{2\pi r}{\lambda}\sqrt{n_{co}^2 - n_{cl}^2}\,, \tag{3}$$

where r is the core diameter of optical fiber.

Taken into account the optical fiber filled in with toluene, the core refractive index n_{co} can be described by the dispersion equation for toluene at the temperature $T = 20$ °C [8]

$$n_{toluene}(\lambda, 20\,^{\circ}\mathrm{C}) = 1.474775 + \frac{6990.31}{\lambda^2} + \frac{2.177810^8}{\lambda^4}, \tag{4}$$

where λ is the light wavelength in nanometers.

Dispersion of the cladding refractive index n_{cl} can be described by the Sellmeier equation for fused silica at the temperature $T = 20$ °C [9]

$$n_{SiO_2}^2(\lambda, 20\,^{\circ}\mathrm{C}) = 1 + \frac{0.6961663\lambda^2}{\lambda^2 - 0.0684043^2} + \\ + \frac{0.4079426\lambda^2}{\lambda^2 - 0.1162414^2} + \frac{0.8974794\lambda^2}{\lambda^2 - 9.896161^2}, \tag{5}$$

where λ is the light wavelength in micrometers.

Toluene was chosen as an appropriate core medium in this approach because of a higher thermal coefficient of refractive index compared to fused silica. While the thermal coefficient of refractive index for fused silica at the temperature $T = 20$ °C and at wavelength 644 nm is 1×10^{-5} K^{-1} [10], the refractive index for toluene at the temperature $T = 20$ °C and at wavelength 633 nm is -5.55×10^{-4} K^{-1} [11]. This considerable difference of the thermal coefficient of the refractive index favors this material combination for designing the optical fiber sensor sensitive to temperature.

Generally, the material and geometrical parameters of optical fibers are changing with temperature. For an optical fiber where the core is represented by toluene and cladding by fused silica, the change of geometrical parameters with temperature can be neglected because the coefficient of thermal expansion for fused silica is 5.5×10^{-7} K^{-1} [10]. Then only changes of the material parameters with temperature are taken into account. The phase constants of the propagating modes are a function of material parameters and then they depend on temperature. The change of the phase constants of the propagating modes with temperature will modify the interference dependence of interfering modes. Investigation of an interference signal as a dependence on temperature can reveal a relation between parameters of intermodal interference and temperature.

The temperature dependence of the refractive index for toluene and fused silica near $T = 20$ °C using eq. (4) and (5) can be expressed

$$n_{toulene}(\lambda, T) = n_{toulene}(\lambda, 20\,^{\circ}\mathrm{C}) + \frac{dn_{toulene}}{dT}(T - 20) \tag{6}$$

and

$$n_{SiO_2}(\lambda, T) = n_{SiO_2}(\lambda, 20\,^{\circ}\mathrm{C}) + \frac{dn_{SiO_2}}{dT}(T - 20) \tag{7}$$

where $\mathrm{d}n/\mathrm{d}T$ are the thermal coefficients of refractive index for toluene and fused silica and T is the temperature in °C.

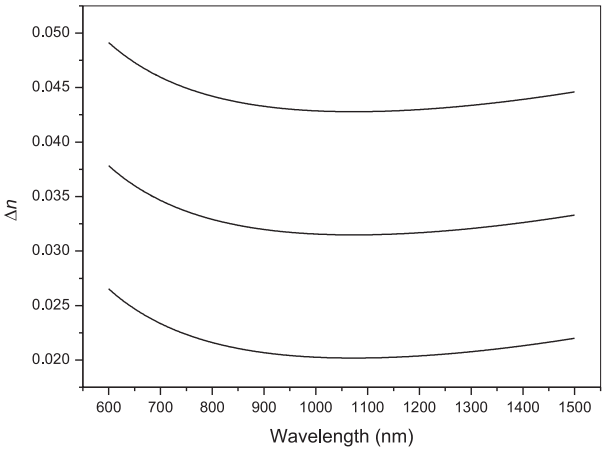

Fig. 1 Refractive index contrast as a function of wavelength calculated at different temperatures of 0 °C, 20 °C, 40 °C from above.

Fig. 1 shows the dependence of the refractive index contrast $\Delta n = n_{toulene} - n_{SiO_2}$ between toluene and fused silica given by (6) and (7) in the wavelength range of 600–1500 nm for the temperatures of 0, 20 and 40 °C. We suppose a constant thermal coefficient of the refractive index of both materials in the calculated wavelength range and for all the temperatures.

The refractive index contrast between toluene and fused silica is positive and small ($\Delta n < 0.05$) in the all considered wavelength range what allows to use the weakly guiding approximation for a description of waveguide properties of the mentioned optical fiber [7].

3. Numerical results

The calculated difference Δβ for modes LP_{01} and LP_{02} is shown in Fig. 2 at the temperatures of 0, 20 and 40 °C. The weakly guiding approximation was used in this calculation for a step-index optical fiber with cladding from fused silica and core with radius $r = 2.5$ μm filled in with toluene.

As shown in Fig. 2 the evident decrease of Δβ is caused by a temperature increase. Maxima in these Δβ spectral dependencies correspond to the equalization wavelength λ_0. The equalization wavelength of the fiber is the wavelength at which the group velocities of two modes are the same [12]. Its value for the optical

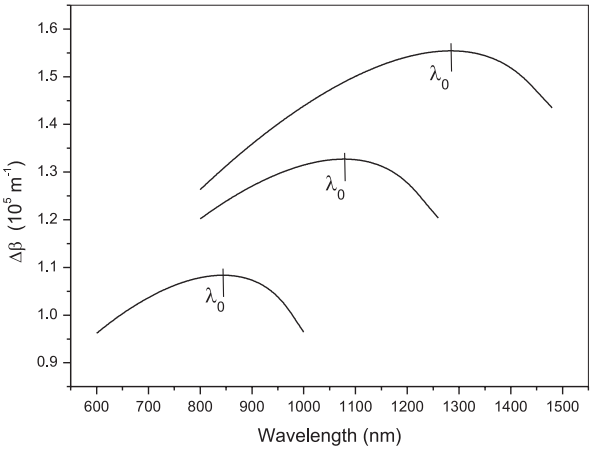

Fig. 2 Δβ as a function of wavelength calculated at different temperatures of 0 °C, 20 °C, 40 °C from above.

fiber with a constant profile of refractive index and radius is a function of only refractive indices of core and cladding [13]. Then the refractive index changes caused by the temperature change the equalization wavelength λ_0. Therefore, the measurement of equalization wavelength in spectral domain can be used for the temperature sensing applications. In the spectral dependencies of Δβ (Fig. 2) the equalization wavelength λ_0 shows the 440 nm blue shift as the temperature increases in the temperature range of 40 °C.

Fig. 3 summarizes calculated results of the equalization wavelength λ_0 in the temperature dependence from 0 °C to 40 °C. In this graph the nearly linear decrease of λ_0 is demonstrated as the temperature increases.

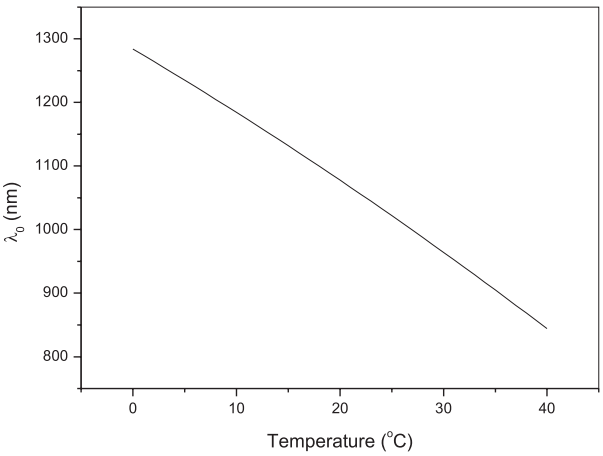

Fig. 3 Equalization wavelength λ_0 in temperature dependence.

From Fig. 3 $\lambda_0 = 1284.2$ nm at 0 °C and $\lambda_0 = 844.1$ nm at 40 °C were estimated. Such a considerable decay of λ_0 in the investigated temperature range favors this method for high sensitive temperature sensing applications based on optical fiber sensors.

In order to characterize the sensitivity, the $d\lambda_0/dT$ dependence on temperature in the temperature range of 0–40 °C was calculated from data shown in Fig. 3 (Fig. 4). For the temperature of 0 °C $d\lambda_0/dT = -9.7$ nmK^{-1} and for the temperature of 40 °C $d\lambda_0/dT = -12.2$ nmK^{-1}.

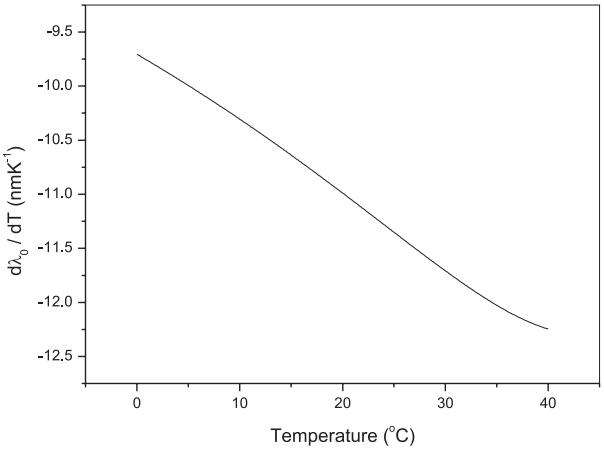

Fig. 4 Sensitivity of this method documented by the dependence of $d\lambda_0/dT$ on temperature.

Methods of the intermodal interference of modes LP_{01} and LP_{02} are well described enabling exact measurement of an interference signal in spatial and spectral domains [14]. In Fig. 5 numerically calculated interference curves of modes LP_{01}–LP_{02} given by (1) for the considered optical fiber 5 cm long at the temperatures of 0, 20 and 40 °C are shown.

It is evident that the equalization wavelength λ_0 can be well identified with resolution better than 1 nm. If $d\lambda_0/dT$ is in the interval from -9.7 nmK^{-1} to -12.2 nmK^{-1} in the investigated temperature range, then the temperature can be determined with resolution better than 0.1 °C.

The exact detection of the equalization wavelength λ_0 is conditioned by the intermodal interference of only modes LP_{01} and LP_{02}. Therefore, this method requires the confinement of propagation of higher cylindric-symmetrical mode LP_{03} near λ_0. For the designed optical fiber sensor for λ_0 at the temperature of 0 °C the cut-off wavelength for LP_{03} is 795 nm and at the temperature of 40 °C it is 562 nm. The position of λ_0 from the presented figures is in the range from 844 nm to 1284 nm in the all investigated temperature range. Thus a good identification of the equalization wavelength λ_0 is guaranteed for such an optical fiber sensor in the proposed temperature range.

4. Conclusion

The temperature sensor based on an optical fiber consisting of fused silica and core of 2.5 μm radius filled in with toluene is proposed in this paper. For temperature sensing the dependence

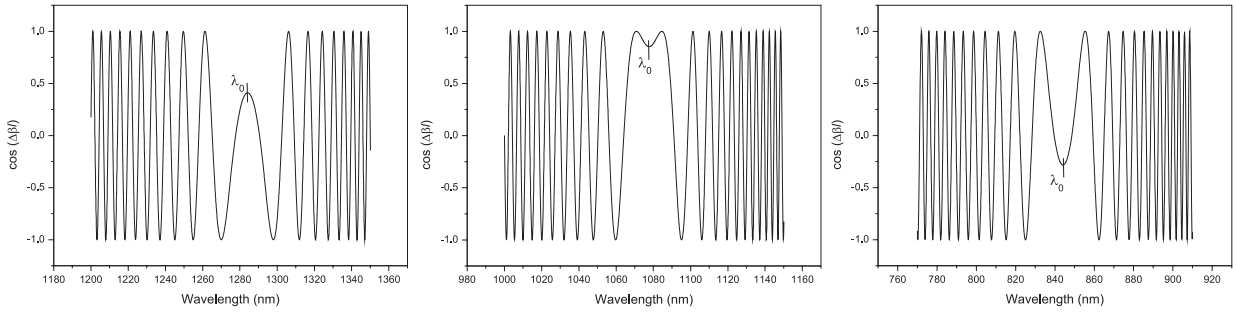

Fig. 5 Spectral dependence of cos (Δβl) with evident decline corresponding to λ_0 shown for temperatures of a) 0 °C, b) 20 °C, c) 40 °C.

of the equalization wavelength λ_0 on temperature is here taken into account using the interfering modes LP_{01}-LP_{02}. The optical fiber sensor was theoretically investigated in the temperature range of 0–40 °C, where we suppose the temperature coefficient of the refractive indices to be constant and independent on wavelength. Then, in the investigated temperature range the equalization wavelength λ_0 for modes LP_{01}-LP_{02} changes from 1284.2 nm to 844.1 nm which favors this method for temperature measurements with resolution better than 0.1 °C.

Such a proposed sensor can be used for temperature measurements in all range of liquid state of toluene from −93 °C to 110 °C. In this wide temperature interval for exact analysis of sensitivity the dependence of refractive indices of toluene and fused silica on the wavelength and temperature should be included in calculations. Then including such relations allows exploitation of this method in a wide temperature range with good accuracy.

Other modifications of the proposed optical fiber sensor are possible where another liquid medium could be used in the core of the optical fiber. Such variability opens a new area of temperature sensing elements where the requested sensitivity and temperature range can be selected by an appropriate choice of liquid medium.

Acknowledgement

This work was partly supported by the Slovak National Grant Agency No. VEGA 1/0868/08 and 1/0683/10. The authors wish to thank for the support to the R&D operational program Centre of excellence of power electronics systems and materials for their components. The project is funded by the European Community, ERDF – European regional development fund.

References

[1] KUMAR, D. SENGUPTA, S., GHORAI, S.K.: *Meas. Sci. Technol.* 19, 2008, p. 065201.
[2] BOCK, W.J., EFTIMOV, T.A.: *Opt. Lett.* 18, 1993, pp. 1979–1981.
[3] LAYTON, M.R., BUCARO, J.A.: *Appl. Opt.* 18, 1979, pp. 666–670.
[4] SPAJER, M.: *Opt. Lett.* 13, 1988, pp. 239–241.
[5] EFTIMOV, T.A., BOCK, W.J.: *J. Lightwave Technol.* 11, 1993, pp. 2150–2156.
[6] TUREK, I., MARTINCEK, I., STRANSKY, R.: *Opt. Eng.* 39, 2000, pp. 1304–1309.
[7] SNYDER, A., LOVE, J.: *Optical waveguide theory,* Chapman and Hall, London, 1983.
[8] SAMOC, A.: *J. Appl. Phys.* 94, 2003, pp. 6167–6174.
[9] MALITSON, I.H.: *J. Opt. Soc. Am.* 55, 1965, pp. 1205–1209.
[10] WEBER, M.J.: *Handbook of Optical Materials,* CRC Press, New York, 2003.
[11] NIKOGOSYAN, D.N.: *Properties of Optical and Laser-Related Materials.* A Handbook, Wiley, Chichester, 1997.
[12] BOUCOUVALAS, A.C., ROBERTSON, S.C.: *Electron. Lett.* 23, 1987, pp. 215–216.
[13] MARTINCEK, I., KACIK, D., TUREK, I., PETERKA, P.: *Optik* 115, 2004, pp. 86-88.
[14] TUREK, I., MARTINCEK, I., KACIK, D., PETERKA, P., GRONDZAK, K.: *Recent Res. Devel. Optical Eng.* 5, 2003, pp. 61–81.

Daniel Kacik – Norbert Tarjanyi – Ivan Turek *

LOW-COHERENCE INTERFEROMETRY FOR MEASUREMENT OF PROPERTIES OF OPTICAL COMPONENTS

We present a modification of the interferometric method for the measurement of refractive index or thickness of optical devices using an easily aligned, almost all-fiber Michelson interferometer. Applicability of the method is demonstrated by the chromatic dispersion measurement of photonic crystal fiber sample. The birefringence of the optical device based on $LiNbO_3$ obtained from the measurement of refractive indices is demonstrated and its value is determined for two different crystal samples. It is also shown that when the thickness of, for example, photopolymer material is known the refractive index of the device can be determined. The described method can be a practical tool for laboratories with the need of inexpensive and easily built setup for measurement of refractive index or thickness of optical devices even in a broad spectral range.

1. Introduction

Generally, the techniques of optical interferometry play a crucial role among the measurement techniques used in optics. Nowadays, many of the techniques employ optical fibers as function part of the interferometer and both, the time-domain and the spectral-domain optical interferometric techniques can be applied to measure various parameters of optical fibers and devices [1, 2]. One of the possibilities of investigation of optical devices' parameters is low coherence interferometry [3]. The appropriate interferometer can be built using bulk optical components [4] or as all (or almost all) fiber interferometer [5, 6]. The principle of methods lies in balancing the optical lengths of two arms of interferometer, where the measured sample is placed in the test arm and the reference arm contains the variable optical delay line.

In the paper the authors discuss the utilisation of the low coherence interferometry for the determination of useful parameters of simple devices for integrated optics such as wave plates and thin photopolymer substrate layers for optical memories. The applicability of the method is demonstrated on the measurement of chromatic dispersion of a sample of photonic crystal fiber.

Photonic crystal fibers [7] offer new optical properties comparing to conventional optical fibers. Especially their dispersion characteristics open up the space for new applications (e.g. supercontinuum generation even in the visible spectrum). Due to the fact that photonic crystal fibers may exhibit large longitudinal inhomogeneity or have large attenuation the interferometric method of chromatic dispersion measurement is often preferred. The dispersion characteristics can be obtained by measuring the group delays τ_g from the interferograms' envelope for several discrete wavelengths λ_i. The measured data $\tau_g(\lambda_i)$ are fitted by an analytical function, e.g. by three- or five- term Sellmeier function. The dispersion coeficient is then given by the relation $D(\lambda) = 1/Ld\tau_g/d\lambda$, where L is the length of the investigated fiber.

Photosensitive crystal lithium niobate ($LiNbO_3$) is one of the best and widely used materials for integrated optics due to its excellent electrooptical and photorefractive properties. Most often the thin plates of the bulk material are used either as simple retarders (wave plates) or as substrates for elements of integrated optics such as waveguides, gratings, switches, directional couplers, optical modulators etc. The bulk crystal is also often regarded as a promissing medium for holographic memory. Except the crystals there are the various kinds of photopolymers the photosensitive properties and cost of which started competing with the crystalline materials during last decade. Nevertheless, the important physical parameters of optical devices whether made of crystalline or photopolymer materials are the refractive index and their thickness. Both these parameters can be determined by low coherence interferometry.

2. Theory

The intensity I of interference pattern of two polychromatic beams with angular frequency falling into interval $\omega_0 \pm \Delta\omega/2$ can be expressed as [8]

$$I = I_1 + I_2 + 2\gamma_{1,2}\sqrt{I_1 I_1}\cos(\varphi), \qquad (1)$$

* **Daniel Kacik, Norbert Tarjanyi, Ivan Turek**
Department of Physics, Faculty of Electrical Engineering, University of Zilina, Slovakia, E mail: kacik@fel.uniza.sk

where I_1 and I_2 are intensities of interfering beams, $\phi = \omega\tau$ is the phase difference between the interfering beams, and γ_{12} is the interference visibility (or "interference contrast").

If the spectral density of ligth intensity is constant in the interval $\omega_0 \pm \Delta\omega/2$, then

$$\gamma_{1,2} = \frac{\sin(\Delta\omega\tau_g)}{\Delta\omega\tau} \tag{2}$$

where $\tau = \frac{(n_1 l_1 - n_2 l_2)}{c}$ is the time delay difference between the beams ($n_{1,2}$ and $l_{1,2}$ means refractive indices and lengths of the arms of the interferometer, respectively).

One arm of the interferometer contains

$$n_1 l_1 = n_{eff}^{SMF} \times L^{ref} + L^{air} + n_{eff}^{objejtive} \times L^{objective} + \\ + n_{eff}^{sample} \times L^{sample} \tag{3}$$

and second arm

$$n_2 l_2 = n_{eff}^{SMF} \times L^{test} + n_{eff}^{FUT} \times L^{FUT} \tag{4}$$

where n_{eff} is the effective refractive index of the particular media, L^{ref} and L^{test} are the fiber lengths of the coupler branch in the reference and test arm, respectively. The difference of fiber lengths of the coupler was less than 0.3%. L^{FUT}, L^{air} and L^{sample} are the lengths of the optical fiber, the air path and thickness of optical devices, respectively. $L^{objective}$ is the length of the microscope objective. In our preliminary work [9] we showed the influence of the microscopic objective on determination of chromatic dispersion of a conventional telecommunication fiber.

The interference term (the third term in right hand side of Eq.(1)) has a maximum when $n_1 l_1 = n_2 l_2$ which allows to determine the refractive index of one arm if the lengths of the arms and refractive index of the second arm are known.

2. Experiment

Schematic layout of the experimental setup is shown in Fig.1. The beam splitter of the Michelson interferometer is made of a fiber coupler with 50:50 coupling ratio at the wavelength of 1550 nm. However, the coupling ratio is still suitable at the range of wavelengths from 1200 nm to 1700 nm.

A halogen lamp and Carl Zeiss monochromator or broadband optical fiber light source OFLS B-15-75-C-F-A was used as the wideband, low coherent light source. The reference arm of the interferometer is composed of a variable-optical-delay line and microscope objective (Meopta 6x, NA = 0.15) to project the end of the fiber onto a mirror. The advantage of this setup is that eventual imperfections of the used mirror are minimized. Additionally, the focusing of the beam is easier than its colimation. The reflected

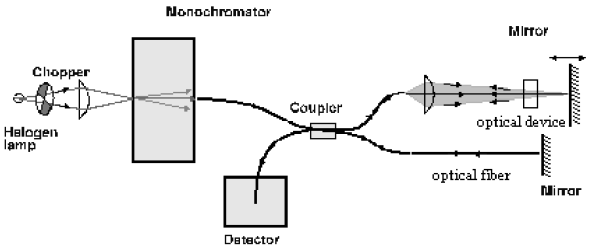

Fig. 1 The experimental setup of the interferometer

beam can be aimed right into the core of the fiber by proper orientation of the mirror. Moreover, the samples (optical devices) under investigation are put into the path of the ligth beam in the air line arm. The length of the variable-optical-delay line is changed using coarse translation in a range of 20–150 cm and fine translation controlled by a micrometric screw in the range of 25 mm. This allows us to find very precisely the position of maximal interference visibility. The microscope objective is also located on a translation stage with micrometric sensitivity – this enables us to correct the spectral dependence of the focal length of the lens. A change of its location is needed for projecting the fiber core back to the fiber core so it does not influence the optical path in the variable-optical-delay line like it is in the case when the mirror is moving. Another way to make the variable optical delay line is to put the fiber into reference arm and balance the optical lengths of two arms interferometer by the change of fiber length [5]. Thus the interferometer can be made all-fiber and alignment-free.

The fiber under test is usually connected to the fiber coupler using bare-fiber adapters. In case of characterisation of fibers with non-standard diameter or with highly off-set core, the fibers have to be aligned using 3D micro-stage. The reflection at the end-face of the measured fiber is usually obtained by a chemical deposition of silver at the cleaved end-face [10]. When investigating the PCF a mirror cannot be created at the end of a fiber because of the air holes in structure of waveguide. For this reason we put PCF into a connector and placed it perpendicular to the mirror using the jig for polishing of the fiber end-face [3]. A disadvantage of the arrangement is a risk of damage of the mirror and fiber end-face.

Interference of the signal from the output end of the fiber coupler was detected by a detector with GaAs or Si photodiode and recorded by a phase sensitive amplifier and an oscilloscope, respectively.

According to Eq. (2) the width of the interval of delay (i.e. the interval of optical path difference), in which the interference contrast significantly differs from zero, depends on the spectral width $\Delta\lambda$ of the beams and for $\Delta\lambda = 20$ nm it is about 0.08 mm as illustrated in Fig. 2.

The measured interferogram is the Fourier transform of an almost rectangular spectrum determined by a monochromator output slit aperture.

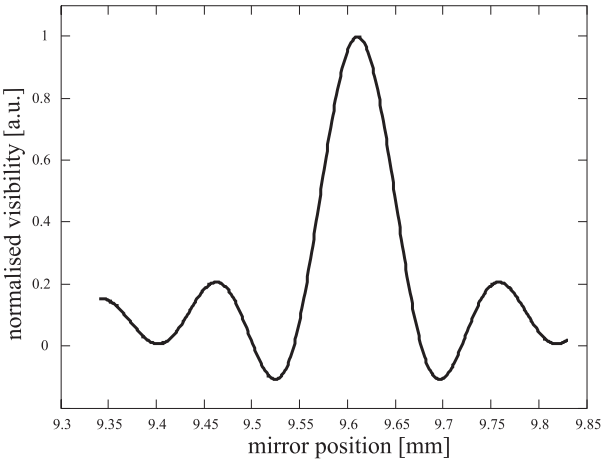

Fig. 2 The mirror position dependence of the interference term of conventional fiber measured at 1550 nm and $\Delta\lambda = 20nm$

The accuracy of determination of optical path difference between the arms (given by the accuracy of determination of the visibility maximum position) is better than 0.01 mm for the light with a spectral width of 20 nm. The resolution of delay difference of interfering beams is of order of 0.01 ps.

3. Results and Discussion

We measured chromatic dispersion of PCF labeled as ASC014_B5a fabricated at OFTC (Optical Fibre Technology Centre) University of Sydney. This fiber is singlemode starting at 1000 nm and has a core diameter of 13 μm. An SEM image of a cleaved cross-section of its triangular lattice is shown in Fig. 3a.

The group delay, τ, as a function of wavelength is measured and this is used to extract the fiber dispersion from the equation:

$$D(\lambda) = \frac{1}{L}\frac{d\tau_g}{d\lambda}$$

where L is the length of measured fiber. The obtained dependencies are shown in Fig. 3b.

The analysis of the measurement of chromatic dispersion of PCF implies that using the experimental set up allows to determine the refractive index of transparent, about 1 cm thick samples with accuracy as precise as 10^{-4}. Such precision allows, for example, to determine the birefringence of crystals, investigate the dependence of their refractive index value on impurities or when the refractive index is known then the thickness of the sample is possible to determine from this measurement. For investigation of the birefringence of crystals two samples of $LiNbO_3$ with different amount of Fe ions and thicknesses were used. The optical axis of the crystal sample was perpendicular to the centre-line of the interferometer's test arm. Due to uniaxiality of the crystal and its alignment according to the centre-line of the interferometer's arm light incident on the crystal's front side is propagating in two polarization states inside the crystal. The ordinary and extraordinary waves travel different optical paths due to different values of refractive indices the waves experience while propagating throughout the crystal. The optical lengths of the test arm are different for ordinary and extraordinary polarized beams. It means that the interference patterns (visibility of interference) for ordinary and extraordinary polarizations will be separated from each other (Fig. 4). The separation of the maxima in the interference pattern is proportional to the birefringence of the crystal. For crystals measured we got values $\Delta n = 0.081$ and $\Delta n = 0.078$. Since the composition of the crystals was slightly different (different Fe doping level) the result implies the possibility to use the low-coherence interferometry for investigation of the dependence of the refractive index value of crystals on impurities.

A similar measurement can be done for any appropriate sample not necessarily a birefringent one. For the results presented here

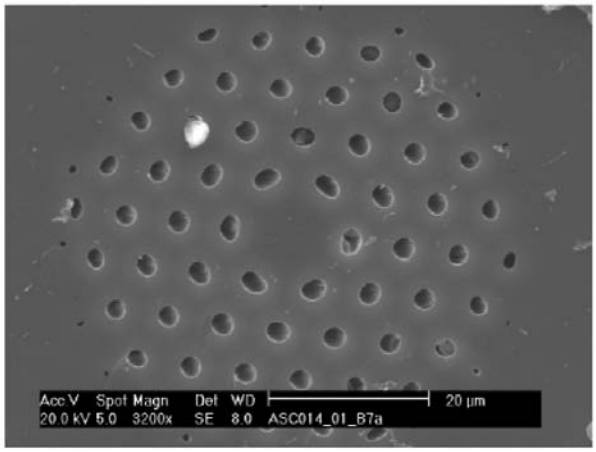

a)

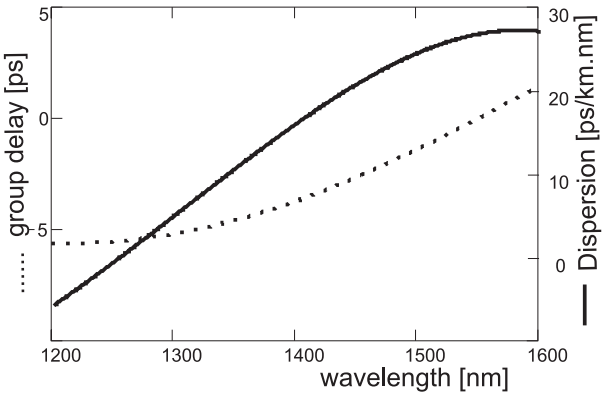

b)

Fig. 3 a) SEM image of cross section of photonic crystal fiber, b) spectral dependance of group delay and dispersion

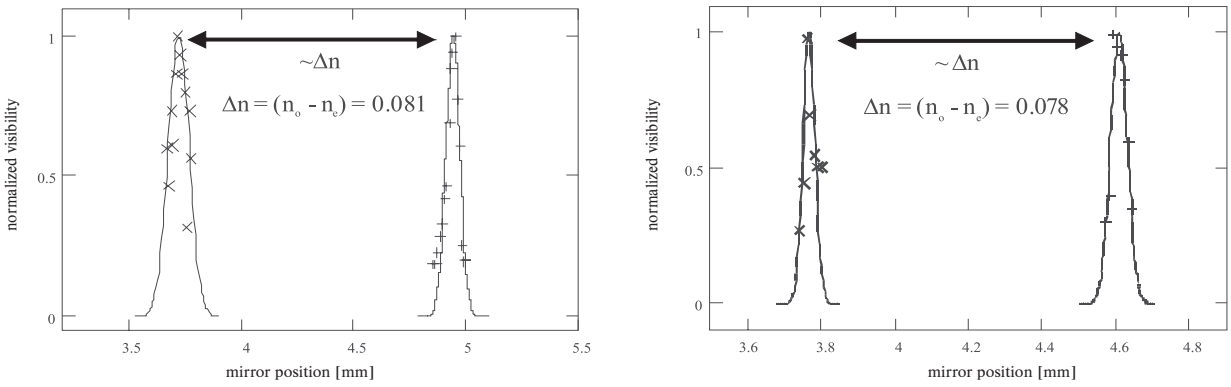

Fig. 4 Birefringence of $LiNbO_3$ with different content of Fe ions imaged by visibility of interference measured at 1550 nm. The thickness of the samples was a) 15.055 mm and b) 10.765 mm.

a polyvinyl-alcohol/acrylamide (PVA/AA) dry material was deposited on the glass plate. The material properties and its response to light are studied because of its intended utilization in holography [11]. The thicknesses of the sample layers were measured by means of a micrometer screw gauge and were about $l = 135\mu m$ on average. The recent methods of investigation of the material properties require to know the values of the refractive indices of PVA/AA at some wavelengths laying in the visible part of light spectrum. However, for some applications one may need to know the refractive index value for a wavelength in a near infrared region. To estimate the refractive index of PVA/AA at 1310 nm we used a Safibra SLED OFSL-B-13-10-C-FA as a light source. First, a clean glass substrate without photopolymer layer was put into the test arm of the interferometer, the optical lengths of the interferometer's arms were balanced and the maximum visibility of interference fringes was measured. Then the glass substrate with a layer of the sample was put into the test arm and the optical lengths of the both arms were balanced again. The particular visibilities of interference are shown in Fig. 5. The distance between peaks of the curves shown in Fig. 5 is the change of the optical path due to a photopolymer layer. After readout of the displayed data we get a value of 0.015 mm for the optical path change and 1.11 for the refractive index of PVA/AA at 1310 nm. Knowing the refractive index of PVA/AA at some wavelengths [e.g. 12] as well as the character of the spectral dependence of the refractive index according to Sellmeier equation for most of optical materials we can treat the resulting value as reasonable.

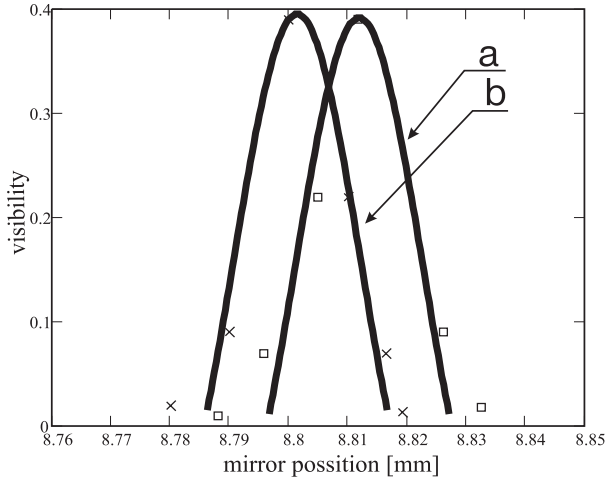

Fig. 5 Visibility function of interference for a) clean glass substrate, b) glass substrate with the photopolymer layer in the test arm of interferometer. Measured at 1310 nm

4. Conclusion

A method of refractive index measurement of optical devices using easily built optical-interferometer-based setup was presented. In contrast to other interferometric methods, it does not require special care for maintaining the interferometer in perfectly stable conditions and at the same time, it offers high accuracy of the group delay determination when investigating the fiber samples. The accuracy of the group delay measurement is 10 fs. The applicability of the presented method was demonstrated on measurement of chromatic dispersion of a sample of photonic crystal fiber. Using the setup we demonstrated the birefringence of the optical device based on $LiNbO_3$ and from the measurement of refractive indices obtained the values of the birefringence for two different samples of iron doped $LiNbO_3$. We also estimated the value of the refractive index of a sample of photopolymer material with the known thickness at the wavelength of 1310 nm. The presented method can be a practical tool for laboratories where exists the need of inexpensive and easily built setup for measurement of refractive index or the thickness of optical devices even in a broad spectral range.

Acknowledgements

The authors wish to thank for the support to the R&D operational program Centre of excellence of power electronics systems and materials for their components. The project is funded by the European Community, ERDF – European regional development fund.

References

[1] HLUBINA, P.: *Measurement of Optical Fibers by Interferometric Methods.* Proc. of SPIE (Optical Fibers: Applications, Warsaw 2005), 5952, p. 192–203, 2005.

[2] TUREK, I., TARJANYI, N.: *Investigation of Symmetry of Photorefractive Effect in $LiNbO_3$*, Opt. Express (15)17, p. 10782–10788, 2007.

[3] PETERKA, P., KANKA, J., HONZATKO, P., KACIK, D.: *Measurement of Chromatic Dispersion of Microstructure Optical Fibers Using Interferometric Method,* Optica Applicata, 38(2): p. 295–303, 2008.

[4] HLUBINA, P.: *White-light Spectral Interferometry to Measure the Effective Thickness of Optical Elements of Known Dispersion.* Acta Physica Slovaca, 55 no. 4, p. 387–393, 2005.

[5] THEVENAZ, L. et al.: *All-fiber Interferometer for Chromatic Dispersion Measurements,* J. of Lightwave Technology, vol. 6, p. 1–7, 1988.

[6] KACIK, D., PETERKA, P., CANNING, J., TUREK, I., KOLIMAR, M., BEREZINA, S.: *The Modified Interferometer for Measurement of the Chromatic Dispersion in PCFs, in Photonic Crystal Fibers,* Proc. SPIE, Vol. 6588, 65880N, 2007.

[7] BJARKLEV, A., BROENG, J., BJARKLEV, A. S.: *Photonic Crystal Fibres,* Kluwer Academic Publishers, Boston, MA, 2003.

[8] KACIK, D., TUREK, I., TARJANYI, N.: *Measurement of Modal Dispersion by Low Coherence Interferometer,* Proc. SPIE, Vol. 7141, 71411K, 2008.

[9] BEREZINA, S., TUREK, I., KACIK, D.: *Practical Arrangement of Interferometer for Optical Fiber Chromatic Dispersion Measurements,* APCOM 2006, p. 312–317, 2006.

[10] DYMAK, P., PETERKA, P.: *Chromatic Dispersion Measurement of Er doped Optical Fibers (in Czech),* In sborník konference Opticke komunikace 2002, Praha, p. 136–140, 2002.

]11] LAWRENCE, J. R., O'NEILL, F. T., SHERIDAN, J. T.: *Photopolymer Holographic Recording Material,* Optik 112(10), p. 449–463, 2001.

[12] GLEESON, M.R. et al.: *Improvement of the Spatial Frequency Response of Photopolymer Materials by Modifying Polymer Chain Length,* J. Opt. Soc. Am. B, 25(3), p. 396–406, 2008.

Zs. J. Horvath – P. Basa – T. Jaszi – A. E. Pap – Gy. Molnar – A. I. Kovalev
D. L. Wainstein – T. Gerlai – P Turmezei *

SILICON NITRIDE BASED NON-VOLATILE MEMORY STRUCTURES WITH EMBEDDED Si OR Ge NANOCRYSTALS

Memory structures with an embedded sheet of separated Si or Ge nanocrystals were prepared by low pressure chemical vapour deposition using a Si_3N_4 control and SiO_2 tunnel layers. It was obtained that a properly located layer of semiconductor nanocrystals can improve both the charging and retention behaviour of the MNOS structures simultaneously. Memory window width of above 6 V and retention time of 272 years was achieved for charging pulses of ±15 V, 10 ms.

1. Introduction

Information storage in non-volatile memories is based on changing the threshold voltage of memory field effect transistors (FETs) by appropriate voltage pulses. The actual mechanism is injection of charge by tunneling and its storage in a floating gate, or in traps in metal-nitride-oxide-semiconductor (MNOS) or silicon-oxide-nitride-oxide-silicon (SONOS) devices located in the nitride layer close to the SiO_2/Si_3N_4 interface [1–8].

Nowadays memory arrays are based mainly on floating gate FETs. The reduction of dimensions is limited in these devices mainly due to reliability problems connected with defects in the thin oxide layer below the floating gate (tunnel oxide). The main problem is that through defects or weak points in tunnel oxide with reduced thickness the whole amount of stored charge carrying the information can be lost [1,6–8].

One of the possible solutions is to replace floating gate with separated semiconductor nanocrystals (NCs), which are electrically isolated. In this case the loss of information via local defects can be avoided [3–8].

Another possible way to avoid the above difficulties is the application of SONOS or MNOS devices. In these structures the charge holding the information is stored in the traps of nitride layer, which are electrically isolated by their nature. So, the effect of local defects in the tunnel oxide is reduced significantly [4,7–9].

Our group realized that formation of semiconductor NCs in nitride based memory structures can enhance both the charging and retention behaviour due to making direct tunneling possible to NCs and creating deep energy states, respectively. So, our idea was to realize MNOS structures with Si or Ge NCs at the Si_3N_4/SiO_2 interface [8–10]. Although two earlier works were devoted to the study the effect of semiconductor NCs in SONOS structures [9, 11], to the best of our knowledge we are the only group studying this effect in MNOS structures.

2. Experiment

For tunnel layer a SiO_2 layer was prepared after cleaning the wafers in 1 wt% HF. The SiO_2 layer was prepared using a HNO_3 treatment [12]; n-type Si wafers were immersed in 68 wt% HNO_3 at the boiling temperature (121 °C) for 60 minutes. This method yielded a SiO_2 layer with a thickness of 2.5 nm, as obtained by cross-sectional transmission electron microscopy [13].

The Si NC layer and the Si_3N_4 control layer were deposited by LPCVD on n-type Si substrates at 830 °C at a pressure of 30 Pa using SiH_2Cl_2 and NH_3. The Si_3N_4 layers were grown at gas flow rates of SiH_2Cl_2 and NH_3 of 21 and 90 sccm, respectively, while the Si NC layer with a gas flow rate of SiH_2Cl_2 of 100 sccm. The duration of deposition for the Si NC layer was 30 s and 60 s. Reference structures without Si NC layer were also prepared. Si_3N_4 control layer for structures with Si NCs was grown during 15 min, which yielded a layer thickness of 37–40 nm, obtained by ellipsometry.

In the MNOS structures with embedded Ge NCs the effects of duration of Ge NC deposition were studied as well (25 s and 50 s). Ge nanocrystals were deposited by electron beam evaporation at 350 °C [14]. The thickness of the control Si_3N_4 layer was about 35 nm. Reference devices without any Ge nanocrystal layers were also prepared.

* **Zs. J. Horvath[1,2], P. Basa[1], T. Jaszi[1], A. E. Pap[1], Gy. Molnar[1], A. I. Kovalev[3], D. L. Wainstein[3], T. Gerlai[1], P Turmezei[2]**
[1] Hungarian Academy of Sciences, Research Institute for Technical Physics and Materials Science, Budapest, Hungary
[2] Obuda University, Kando Kalman Faculty of Electrical Engineering, Institute of Microelectronics and Technology, Budapest, Hungary
[3] Surface Phenomena Researches Group (SPRG), CNIICHERMET, Moscow, Russia
E-mail: horvzsj@mfa.kfki.hu, Horvath.Zsolt@kvk.obuda-uni.hu

For electrical and memory measurements Al capacitors were formed with dimensions of 0.8 mm by 0.8 mm by evaporation. For backside ohmic contact also Al was evaporated after an appropriate chemical surface treatment [15].

The crystal structure of the layers was studied by X-ray photoelectron spectroscopy (XPS). Memory window and retention measurements were carried out on the capacitors. In this case the appropriate parameter for the characterisation of the memory effect and retention behaviour is the shift of flat-band voltage of capacitor. Memory window measurements were performed using voltage pulses with amplitude in range ±3 to ±25 V and width in range 10 ms to 400 ms. To enhance the development of the inversion layer, and so to avoid high voltage drop on the deep depletion layer during negative voltage pulses, the structures were illuminated with white light during memory window measurements. Retention measurements were performed in dark.

3. Results and Discussion

XPS results obtained on the MNOS structures after removing the upper part of the control silicon nitride layer clearly indicate the presence of NCs at the oxide/nitride interface, as it is presented in Fig. 1 for the structures with Si NC deposition duration of 30 s and 60 s. The Si NC peak is much more pronounced for a deposition duration of 60 s, than for 30 s, as it was expected.

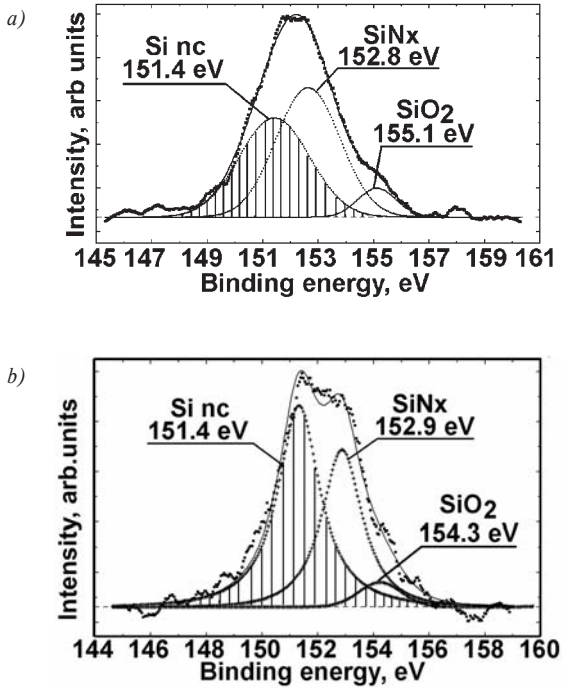

Fig. 1. Si 2s photoelectron spectrum of MNOS structures with Si nanocrystal deposition duration of 30 s (a) and 60 s (b) after Ar ion etching at depth of 38 nm.

The results of memory window measurements as a function of charging pulse amplitude with pulse width of 10 and 150 ms are presented in Fig. 2 for structures with Si nanocrystal deposition duration of 60 s. For longer charging pulses a wider memory window was obtained. The effect of Si NC deposition on the memory window is demonstrated in Fig. 3, which presents the memory window width for structures with Si nanocrystal deposition duration of 30 s and 60 s, and without middle NC layer deposition (indicated as 0 s duration), as a function of charging pulse amplitude. The structures with Si NCs exhibited a wider memory window for the whole studied voltage range than the reference structure.

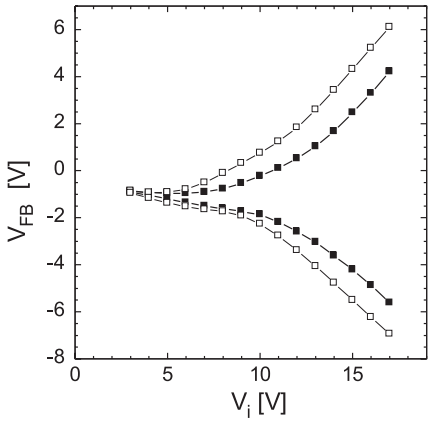

Fig. 2. The position of a memory window as a function of writing/erasing pulse amplitude with the pulse width of 10 ms (filled dots) and 150 ms (open dots) for the studied MNOS structures with Si nanocrystal deposition duration of 60 s. The upper curves are obtained for positive, the lower curves for negative voltage pulses.

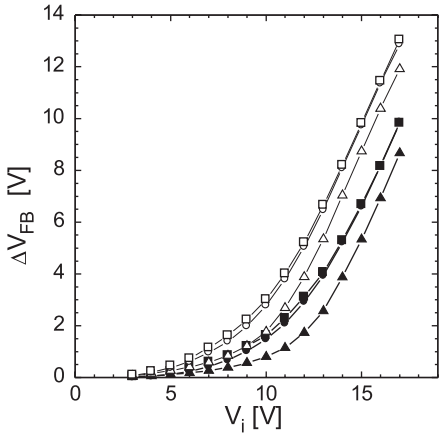

Fig. 3. The memory window width as a function of writing/erasing pulse amplitude with the pulse width of 10 ms (filled dots) and 150 ms (open dots) for the studied MNOS structures with Si nanocrystal deposition duration of 0 s (triangles), 30 s (circles), and 60 s (squares).

Retention behaviour is determined on the basis of flat-band voltage shift as a function of time after the application of a charg-

ing pulse. This shift of flat-band voltage is due to the loss of charge holding the information, through the tunnel and/or control layer. The shift exhibits logarithmic dependence on the time. So, plotting flat-band voltage as a function of the logarithm of time, a linear relation is obtained. The retention time (the time necessary to the lost of information) or the width of memory window after a certain time can be extrapolated from this linear relation fitted to the experimental data points [10]. Results concerning the retention behaviour of the studied structures with Si NCs are presented in Table 1. It is seen that the presence of Si NCs decreased the retention time, but for the samples with NC deposition of 30 s the memory window width after 10 years is still detectable. The extrapolation of flat-band voltage shift yielded a retention time of 41 years for these samples. It is even much higher than the standard requirement of 10 years.

The initial and extrapolated from the retention measurements for 1 and 10 years memory window widths for the studied structures. The charging pulse amplitude was ±15 V, the pulse width 10 ms — Tab. 1.

Nano-crystal	Nano-crystal deposition duration (s)	Initial memory window width (V)	Extrapolated memory window after 1 year (V)	Extrapolated memory window after 10 years (V)	Retention time (years)
Si	0	5.34	0.87	0.46	128
Si	30	6.61	0.85	0.32	41.2
Si	60	6.68	0.47	0	7.37
Ge	0	5.81	0.72	0.22	27.0
Ge	25	6.31	1.14	0.67	272
Ge	50	6.12	0.25	0	2.64

The results of memory window measurements of MNOS structures with Ge nanocrystals as a function of writing/erasing pulse amplitude with pulse width of 100 ms are presented in Fig. 4. The memory window is somewhat wider for memory structures with NCs than in the reference sample. However, while in the structures with Si NCs a longer deposition duration of NCs yielded a wider memory window, in the structures with Ge NCs the memory window is wider for a shorter deposition time.

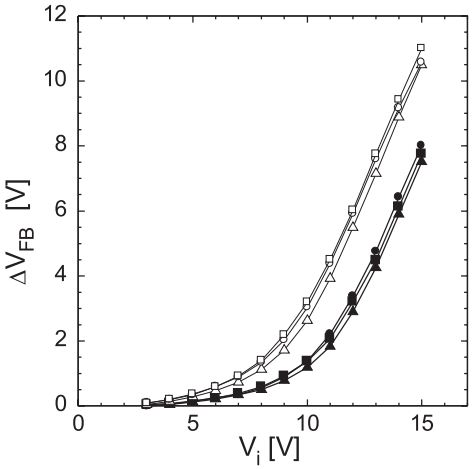

Fig. 4. The memory window width as a function of writing/erasing pulse amplitude with the pulse width of 10 ms (filled dots) and 150 ms (open dots) for the studied MNOS structures with Ge nanocrystal deposition duration of 0 s (triangles), 25 s (circles), and 50 s (squares).

The retention behaviour of the structures with Ge NCs is also summarized in Table 1. The best retention time of 272 years was obtained for Ge NC deposition duration of 50 s. It is very important that both injection and retention performances of samples with deposition duration of 50 s are better than those for reference samples without NCs. This demonstrates that a sheet of semiconductor NCs can improve both the injection and retention behaviour of silicon nitride based memory devices simultaneously [7,8].

4. Summary

MNOS structures with embedded Si or Ge nanocrystals were prepared by LPCVD and studied by memory window and retention measurements. Both the memory window and retention depended on the presence and deposition duration of nanocrystals. The presence of nanocrystals increased the memory window width, and enhanced in some cases the retention behaviour as well. The results demonstrate that a sheet of semiconductor nanocrystals can improve both the injection and retention behaviour of silicon nitride based memory devices.

References

[1] PARAT, K. K.: *Flash Memory Technology - Recent Advances and Future Outlook, in Physics of Semiconductor Devices, (Eds. K. N. Bath and A. DasGupta),* Narosha Publishing House, New Delhi, 2004, pp.433–438.

[2] NORMAND, P., KAPETANAKIS, E., DIMITRAKIS, P., SKARLATOS, D., BELTSIOS, K., TSOUKALAS, D., BONAFOS, C., BEN ASSAYAG, G., CHERKASHIN, N., CLAVERIE, A., BERG, J. A. VAN DEN, SONCINI, V., AGARWAL, A., AMEEN, M., PEREGO, M., FANCIULLI, M.: *Nanocrystals manufacturing by ultra-low-energy ion-beam synthesis for non-volatile memory applications, Nucl. Instr. and Meth. B,* Vol. 216, 2004, pp. 228–238, and references therein.

[3] DIMITRAKIS, P., KAPETANAKIS, E., TSOUKALAS, D., SKARLATOS, D., BONAFOS, C., ASSAYAG, G. BEN, CLAVERIE, A., PEREGO, M., FANCIULLI, M., SONCINI, V., SOTGIU, R., AGARWAL, A., AMEEN, M., SOHL, CH., NORMAND, P.:

Silicon nanocrystal memory devices obtained by ultra-low-energy ion-beam synthesis, Solid-State Electron., Vol.48, 9/2004, pp. 1511–1517.

[4] DE SALVO, B., GERARDI, C., SCHAIJK, R. VAN, LOMBARDO, S. A., CORSO, D., PLANTAMURA, C., SERAFINO, S., AMMENDOLA, G., DUUREN, M. VAN, GOARIN, P., MEI, W. Y., JEUGD, K. VAN DER, BARON, T., GÉLY, M., MUR, P., DELEONIBUS, S.: *Performance and Reliability Features of Advanced Nonvolatile Memories Based on Discrete Traps (Silicon Nanocrystals, SONOS), IEEE Trans. Dev. Mater. Reliability, Vol.4, 3/2004, 377–389, and references therein.*

[5] PODOR, B, HORVATH, ZS. J., BASA, P.(Eds.): *Semiconductor Nanocrystals; Proc. First Int. Workshop on Semiconductor Nanocrystals SEMINANO2005, Sept. 10–12, 2005, Budapest, Hungary* Vols. 1 and 2; http://www.mfa.kfki.hu/conferences/seminano2005/

[6] HORVATH, ZS. J.: *Semiconductor Nanocrystals in Dielectrics: Optoelectronic and Memory Applications of Related Silicon Based MIS Devices, Current Appl. Phys.,* Vol. 6, 2/2006, pp.145–148, and references therein.

[7] HORVATH, ZS. J., BASA, P.: *Nanocrystal Non-volatile Memory Devices, Mater. Sci. Forum,* Vol. 609, 2009, pp. 1–9, and references therein.

[8] HORVATH, ZS. J., BASA, P.: *Chapter 5: Nanocrystal memory structures, in: Nanocrystals and Quantum Dots of Group IV Semiconductors, (Eds. T. V. Torchinskaya, Yu. V. Vorobiev)*, American Scientific Publishers, in press, and references therein.

[9] RAO, R. A., STEIMLE, R. F., SADD, M., SWIFT, C. T., HRADSKY, B., STRAUB, S., MERCHANT, T., STOKER, M., ANDERSON, S. G. H., ROSSOW, M., YATER, J., ACRED, B., HARBER, K., PRINZ, E. J., WHITE JR., B. E., MURALIDHAR, R.: *Silicon nanocrystal based memory devices for NVM and DRAM applications, Solid-State Electron.,* Vol. 48, 2004, pp.1463–1473.

[10] HORVATH, ZS. J., BASA, P., JASZI, T., PAP, A. E., DOBOS, L., PACZ, B., TOTH, L., SZOLLOSI, P., NAGY, K.: *Electrical and Memory Properties of Si_3N_4 MIS Structures with Embedded Si Nanocrystals, J. Nanosci. Nanotechnol.,* Vol. 8, 2/2008, pp.812–817.

[11] AMMENDOLA, G., ANCARANI, V., TRIOLO, V., BILECI, M., CORSO, D., CRUPI, I., PERNIOLA, L., GERARDI, C., LOMBARDO, S., DESALVO, B.: *Nanocrystal memories for FLASH device applications", Solid-State Electron.,* Vol. 48, 2004, pp. 1483–1488

[12] KOBAYASHI, H., ASHUA, MAIDA, O., TAKAHASHI, M., IWASA, H.: *Nitric Acid Oxidation of Si to Form Ultrathin Silicon Dioxide Layers with a Low Leakage Current Density, J. Appl. Phys.,* Vol. 94, 6/2003, pp. 7328–7236.

[13] DOBOS, L., PECZ, B., TOTH, L.: unpublished.

[14] BASA, P., MOLNAR, GY., DOBOS, L., PECZ, B., TOTH, L., TOTH, A. L., KOOS, A. A., DOZSA, L., NEMCSICS, A., HORVATH, ZS. J.: *Formation of Ge Nanocrystals in SiO_2 by Electron Beam Evaporation, J. Nanosci. Nanotechnol.,* Vol. 8, 2/2008, pp. 818–822.

[15] HORVATH, ZS. J., ADAM, M., SZABO, I., SERENYI, M., TUYEN, VO VAN.: *Modification of Al/Si Interface and Schottky Barrier Height with Chemical Treatment, Appl. Surf. Sci.*, Vol. 190, 5/2002, pp. 441–444.

M. Timko – P. Kopcansky – M. Koneracka – V. Zavisova – N. Tomasovicova – A. Dzarova *

MAGNETIC NANOPARTICLES FOR APPLICATION IN NANOMEDICINE

This contribution will summarize the information about the ways of synthesizing biocompatible magnetic nanoparticles and complexes containing them and the possibility of their application in nanomedicine at magnetic drug targeting and thermal treatment of diseases by hyperthermia effect. Some procedures of the preparation of biocompatible magnetizable complexes as magnetic nanoparticles, magnetic fluids, some proteins and enzymes covalently bound to the freshly prepared magnetic nanoparticles in the presence of carbodiimide (bovine serum albumin, streptokinase, chymotrypsin, dispase, glucose oxidase), entrapment of magnetic particles into magnetoliposomes and encapsulation of clinically important drug as indomethacin and taxol together with magnetite nanoparticles in biodegradable polymer. We will summarize the results from the study of structural, magnetic and hyperthermic properties of bacterial magnetite nanoparticles i.e. magnetosomes prepared by biomineralization process of magnetotactic bacteria as a promising material for application in nanomedicine.

1. Introduction

Since the mid 1970s, magnetic particles and fluids or ferrofluids as they are often called, have increasably been used in the area of bioscience and nanomedicine. Magnetic nanoparticles offer some attractive possibilities in biomedicine as they have controllable sizes ranging from a few nanometers up to tens of nanometers, which places them at dimensions that are smaller than or comparable to those of the cell (10–100 μm), a virus (20–450 nm), a protein (5–50 nm) or a gene (2 nm wide and 10–100 nm long). This means that they can get close to a biological entity of interest. On the other hand, although often referred to as magnetic, many of the particles currently used are superparamagnetic, meaning that these particles can be easily magnetized with external magnetic field and redispersed immediately once the source of the magnetic field is removed. The reaction of magnetic particles to a remote magnetic force is their unique feature, which can be used in many applications involving the transport and retaining of magnetic nanoparticles with immobilized anticancer drug in targeted region of the body such as a tumor and bioseparation including cell sorting. Magnetic particles also can have resonant response to a time-varying magnetic field with advantageous results related to the transfer of energy from the exciting field to the nanoparticles. This enables effective thermotherapy (hyperthermia) as one of the promising approaches in cancer therapy. Of course, magnetic particles themselves generate a magnetic field and influence the local area around them. This feature is exploited in magnetic resonance imaging (MRI). These and many other potential applications are made available in biomedicine as a result of the special physical properties of magnetic nanoparticles. From the physiological point of view the critical parameters of magnetizable complex systems and magnetic field are particle size, surface characteristics of the particle, concentration and volume of the fluid, reversibility and strength of the drug-ferrofluid binding (desorption characteristics), access of organism (infusion route), duration and rate injection, geometry and strength of the external magnetic field. On the other hand, physiological parameters of the organism comprise size, weight, body surface, blood volume, vascular resistance, circulation time, tumor volume and location, vascular content of tumor and blood flow in tumor [1].

The principal problems currently associated with systematic drug administration are a) even biodistribution of pharmaceuticals throughout the body, b) the lack of drug specific affinity toward a pathological site, c) the necessity of a large total dose of a drug to achieve high local concentration, e) non-specific toxicity and other adverse side-effects due to high drug doses [2]. Magnetic drug targeting can bring solution to all these problems. Magnetic drug targeting allows the concentration of drugs at a defined target site generally and, importantly, away from the reticular endothelial system (RES) with the aid of a magnetic field. The intended drug and a suitable magnetically active component (magnetic fluid) are formulated into a pharmacologically stable formulation. This compound is injected intravenously in the presence of an external magnetic field with sufficient field strength and gradient to retain the carrier at the target site.

After particles are injected into the bloodstream they are rapidly coated by components of the circulation, such as plasma proteins. This process is known as opsonization and is critical in dictating the circumstance of the injected particles [3]. So, the application of nanoparticles *in vivo or ex vivo* would require surface

* **M. Timko, P. Kopcansky, M. Koneracka, V. Zavisova, N. Tomasovicova, A. Dzarova**
Institute of Experimental Physics, Slovak Academy of Sciences, Kosice, Slovakia, E-mail: timko@saske.sk

modification that would ensure particles were non-toxic, biocompatible and stable to the reticulo-endothelial system. Generally the magnetic particles are coated by a biocompatible polymer such as polylactic acid (PLGA), derivates of dextran, polyethylene glycol (PEG), polyethylen oxide or polyoxamines. The coating acts to shield the magnetic particle from the surrounding environment and can be functionalized by attaching carboxyl group, biotin, avidin, carbodi-imide and other molecules [4–6].

2. Biocompatible magnetic materials

A variety of magnetic nanoparticle and microparticle carriers have been developed to deliver drugs to specific target sites *in vivo*. The biocompatible nanoparticles or magnetic fluids during the therapy are injected intravenously and then blood circulation would be used to transport the particles to the region of interest for treatment. Alternatively, the particle suspension would be injected directly into the treatment area. Either of these routes has the requirement that the particles do not aggregate and block their own spread. This leads to the question about the best way to produce magnetic nanoparticles and consequent magnetic fluids. It was shown that nanoparticles of about 5 – 10 nm should form the ideal particles for the most forms of therapy but that there will also be problems of formulating the particle concentrations and suspending media to obtain best distribution [7]. We will focus on some procedures to prepare a biocompatible magnetizable complex system.

2.1. Covalent binding procedure

The targeting of drug-bearing magnetic particles to a specific part of the body has been studied using magnetic fluids (stable suspensions of highly dispersed particles of magnetic materials), unstable suspensions (well dispersed systems containing multi-domain magnetic particles) and magnetic microspheres (complex systems comprising special matrix materials like albumin, polysaccharide or containers like liposomes or erythrocytes) [8, 9]. These systems are ideal for carrying small molecular weight pharmacologically active substances to a target area. However, these systems are not ideal for transporting enzymes to a target area for treatments of clot lysis in peripheral and coronary vascular occlusive diseases. In the present study, an attempt was made to link protein molecules as bovine serum albumin (BSA), glucose oxidase (GOD), chymotrypsin, streptokinase and dispase directly to magnetic particles using CDI as the coupling agent. Different values of pH and ratios of magnetic particles to protein were studied in order to establish the optimum conditions for immobilization. The direct coupling of enzymes or bioactive molecules to the magnetic particles has a number of potential advantages.

Several advantages could be envisaged of such preparations where molecules are directly linked to a magnetic material, like ferrite, the lack of a polymer coat results in smaller particles, thus increasing the ratio of surface area to volume, allowing a greater response to any magnetic field; studies on the use of magnetic particles for cell-separation have revealed that the larger the particle size used for separation, the higher the extent of non-specific entrapment in the larger aggregates of magnetic particles, thus smaller magnetic particles hold the promise of greater specificity; small magnetic particles can exist as stable colloidal suspensions (ferrofluids) that will not aggregate, thus allowing for uniform distribution in a reaction mixture; the direct coupling method described in our papers [6,10] is both simple (one-step) and inexpensive. In our experiment BSA, GOD, chymotrypsin, streptokinase and dispase were immobilized onto magnetic particles using CDI. The coupling reactions were carried out under different conditions to determine the optimum conditions for immobilization of proteins, i.e. change of the pH of the reaction mixture and proportion of magnetic particles to proteins. The present findings clearly show that it is possible to bind proteins onto magnetic particles in the presence of CDI without the aid of a primary coating. The binding is due to the presence of hydroxyl groups on the surface of fine magnetic particles freshly prepared from Fe_3O_4. The optimal conditions for the immobilization of the various proteins and enzymes to fine magnetic particles depend on the kind of immobilized proteins and enzymes, the pH of the reaction mixture and the ratio of each reagent in the reaction mixture, respectively. The present findings have several applications in medicine and biotechnology. One of the important applications worth exploring is the treatment of coronary thrombosis and peripheral arterial occlusions. The present procedure could also be used to remove carcinogenic cells from the circulation to prevent metastases by using magnetic antibodies specific for tumor cell surface antigens.

2.2. Liposome entrapment procedure

In order to improve the accumulation of magnetite particles in a target site the magnetoliposomes were developed [11]. This new type of vesicle consisted of nanosized magnetic particles or magnetic fluid wrapped in a phospholipids bilayer with or without drugs offers new challenges in the field of modern biotechnology and biomedicine. To overcome problem with the releasing of drug from the magnetoliposomes a variety of approaches have been employed including complexation of DNA with cationic lipids [12], the design of thermosensitive liposomes capable of releasing their contents in response to small changes in temperature [13], and the development of pH-sensitive liposomes [14]. As the magnetoliposomes offer new challenges in the field of modern biotechnology and biomedicine it is very important to know the transport properties of the membrane-impermeant substances into cells. In our previous work [15] we have used the magnetoliposomes consisted of lipid mixture dipalmitoylphosphatidylcholine (DPPC) with nanosized magnetic particles and liposomes wrapped dye Crystal Violet for the study of transmembrane transport. The prepared magnetoliposomes were observed using Transmission Electron Microscopy. It was shown that there exists temperature dependent non-zero transport of dye from liposom to magnetoliposome. The lipid bilayer of the used DPPC provides a simplified model of cellular membrane because any “impurities” in the form of proteins are missing in the lipid bilayer.

2.3. Polymer nanospheres

Magnetic particles encapsulated with drug into biocompatible polymer have potential applications in the field of magnetic drug targeting. Non-specific intravenously administered drugs are systemically distributed and attack normal, healthy cells in addition to the target cells. Magnetically controlled drug targeting could reduce side effects. This technique is based on the binding of a selected drug with magnetic fluids into a pharmacologically stable formulation. The drug can be dissolved, entrapped, encapsulated or attached to nanoparticles and depending on the method of preparation, nanoparticles, nanospheres (NPs) or nanocapsules can be obtained. Biodegradable NPs formulated using biodegradable polymer poly(lactide-co-glycolide) (PLGA), can be used as carriers for drug. In addition to being biodegradable, other advantages include reduced frequency of administration, sustained drug release, reduced dosage, and less systemic side effects [16]. Polylactic acid (PLA) and PLGA have been approved for human use by the United States Food and Drug Administration (USFDA) as surgical sutures, implantable devices, and drug delivery systems [17]. Magnetic-polymeric NPs (MNPs) must fulfill several requirements such as biocompatibility, biodegradability, mechanical strength, and ease of producing. The constituents of the magnetically active polymeric NPs play different roles: the polymeric matrix acts as a shell, reservoir, and vehicle for the active component, whereas magnetite is the component which makes targeting possible by external magnetic field manipulation. Well known classes of biodegradable materials for controlled release are the PLGAs. The main advantage of these degradable polymers is that they are broken down into biologically acceptable molecules that are metabolized and removed from the body via normal metabolic pathways.

Indomethacin (IND) is a nonsteroidal anti-inflammatory drug (NSAID) that reduces fever, pain, and inflammation. As IND may cause or worsen stomach or intestinal bleeding or ulcers and can increase blood pressure and decrease kidney function, it is important to decrease used dosages and side effects during the treatment. One of the possibilities to do it is direct delivery of the drug to the target area of the body by external magnetic field. Magnetically controlled drug targeting is one of the various possibilities of drug targeting. This technology is based on the encapsulation of drug (in our case IND) with magnetic particles that concentrate the drug in the area of interest by means of magnetic fields.

In our previous study [18, 19] IND, which is a poorly water-soluble antiinflammatory drug, was encapsulated in magnetic biodegradable PLA. The magnetite nanoparticles were prepared by the coprecipitation method of ferric and ferrous salts in an alkali aqueous medium was used to prepare magnetite particles [15]. Sodium oleate ($C_{17}H_{33}COONa$) as surfactant was used for the modification of prepared magnetic particles to prevent their agglomeration. Sodium oleate (10wt% with respect to Fe_3O_4) was added to the suspension of Fe_3O_4 and mixed under heating until the boiling point was reached. The saturation magnetization of the prepared magnetic fluid (with a 2% volume concentration of Fe_3O_4) and average diameter of magnetite particles were estimated by VSM magnetometer to be 6.5 emu/g and 10 nm, respectively. Infrared spectroscopy confirmed the incorporation of magnetic particles and drug in the polymer. The next objectives were focused on the enhancement of incorporation efficiency of drug including the influence of the pH aqueous phase in magnetic PLA nanospheres. Finally, the release behavior of IND was examined by an external sink method. Two simple models, diffusion and dissolution, were applied for the description of the experimental data of IND release and for the identification of the release mechanism. It can be said that the encapsulation of IND into magnetite-labeled biodegradable polymer was successfully realized. The biodegradable polymer nanoparticles made by nanoprecipitation method were spherical in shape, and their particle size was about 250 nm in diameter. The successful encapsulation of the IND and magnetic particles into PLA was confirmed by infrared spectroscopy. Release experiments showed that 70 % of the drug was released within 5 h and a plateau was reached within 10 h at 80 %. Such IND-loaded magnetic nanoparticles could be useful for magnetic drug targeting of inflammatory diseases.

Taxols (paclitaxel, TAX) an important anticancer drug, has been chosen for encapsulation into the polymer for its significant role against a wide range of tumors (breast cancer, ovarian carcinoma, lung cancer, and head and neck carcinomas) [20]. TAX is a natural diterpenoid alkaloid, firstly isolated from the bark of the yew Taxus brevifolia [21]. It is not affordable from the nature. The other limitation of TAX applications is its high insolubility in water and most pharmaceutical solvents. Adjuvants such as Cremophor EL have to be used in its current clinical administration, which, by itself, causes serious side effect hypersensitivity reaction. To eliminate the side effects of the adjuvant and to improve the therapeutic efficacy of the drug, alternative dosage forms have been suggested, including liposomes, microspheres, and polymeric nanoparticles (NPs). Other important advantages associated with the use of NPs include the simplicity of their preparation with well-defined biodegradable polymers and their high stability in biological fluids and during storage. The modified nanoprecipitation method was used to entrap magnetic fluid (MFPEG) and anticancer drug TAX into polymer NPs. To prepare a stable colloid of magnetic particles, sodium oleate ($C_{17}H_{33}COONa$) as a first surfactant was used to prevent their agglomeration. The key parameters of the behavior of magnetic particles are related to the nature of their surface. The chemical composition of the surface is especially important to avoid the action of the reticuloendothelial system (RES), which is a part of the immune system, to increase the half-life in the blood stream. Coating the magnetic particles with a neutral and hydrophilic compound-poly(ethylene glycol), the circulatory half-life increases from minutes to hours or days. Thus, PEG as a second surfactant was added to the system magnetite-sodium oleate. The more detail description of preparation, procedure, magnetic and morphological properties is given in our papers [22, 23]. Scanning Electron Microscopy (SEM) was used to determine the morphology and size of various TAX-loaded nanoparticles (TAXMNPs shown in Fig. 1). The surface was primarily smooth, although some roughness could be identified in certain areas of some spheres. The mean diameter of all NP samples was approximately 200–250 nm and the results were in good agreement with the results obtained with the PCCS technique.

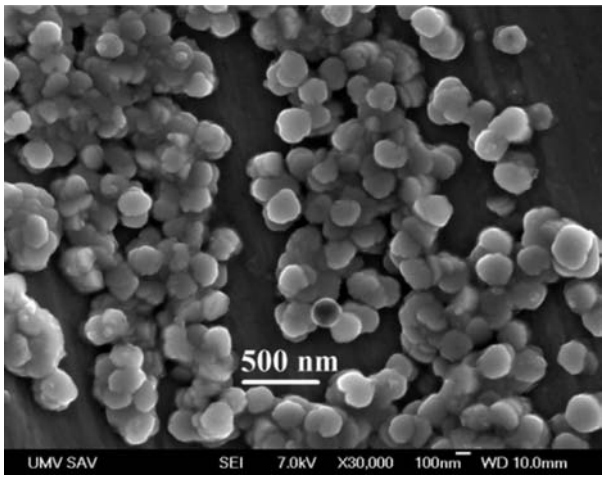

Fig. 1 SEM image of taxol-magnetite-PLGA nanospheres

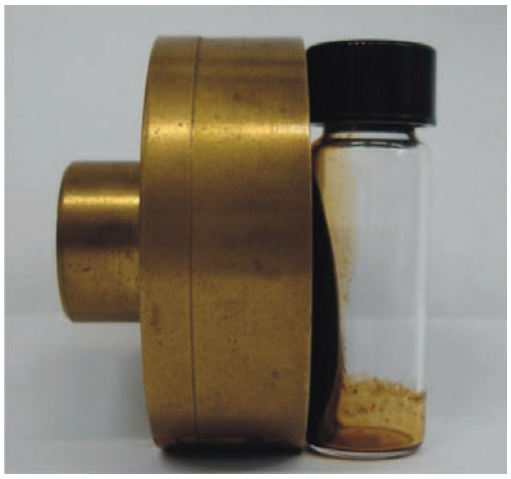

Fig. 2 Encapsulated taxol and MF-PEG in PLGA attached to a magnet

We can state that we have prepared and characterized TAXMNPs with a spherical shape of the mean diameter lower than 250 nm, which is a relevant size for intravenous administration. Using IR spectroscopy, TAX was successfully identified in the TAXMNPs before the release process and also in the TAXMNPs that had been releasing TAX into a phosphate buffer. The prepared NPs have been found to have good stability in the presence of high NaCl concentration at ambient temperature, the toxicity (preliminary 'up and down' method) of prepared samples declared a three times higher value of lethal dose LD50 (see Table 1) in comparison with pure TAX (LD50 = 33 mg/kg) and showed a significant response to the external magnetic field which is useful for drug delivery systems for tumor treatment (see Fig. 2).

The lethal dose in vivo experiments Table 1

Sample	LD50
MFPEG	400 mg Fe3O4/kg
PLGA NPs	221 mg PLGA/kg
PLGA/TAX	226 mg PLGA kg (at 11.3 mg TAX /kg)
PLGA/MFPEG	174 - 198 mg PLGA/kg
PLGA/MFPEG/TAX	154 mg PLGA/kg (at 7.7 mg TAX /kg)

A good sink condition was achieved using sodium salicylate solution, a hydrotropic agent, as a good alternative to increase the aqueous TAX solubility for in vitro TAX release studies from TAXMNPs. The effect of pH (pH = 6.0, 6.6, and 7.4) as well as the molar concentration of sodium salicylate in the release medium (1, 2, and 3M) on the release profiles of drug were studied and it can be concluded that TAX release from TAXMNPs was not significantly influenced by the pH value of the phosphate buffer (Fig. 3). The slope of the initial release process increased with increasing sodium salicylate concentration of the release medium. The presence of sodium salicylate in the release medium significantly influenced the release profile of TAX and the cumulative released amount of TAX in 9 days was around 50% (for 2 and 3M sodium salicylate).

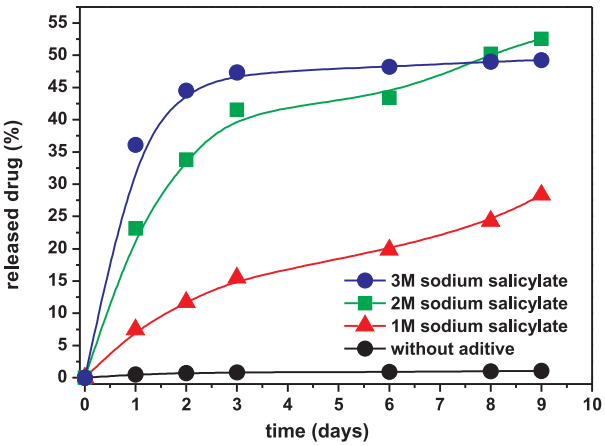

Fig. 3 Time dependence of the released drug at pH = 7.4 from TAXMNPs to (a) phosphate buffer, (b) phosphate buffer with 1M sodium salicylate, (c) phosphate buffer with 2M sodium salicylate and (d) phosphate buffer with 3M sodium salicylate

The surface modification of magnetite with PEG was a useful approach to prepare biocompatible magnetic fluid suitable for entrapment into a hydrophobic polymer PLGA together with the anticancer drug taxol by the nanoprecipitation method. The nanospheres were nearly spherical with the mean diameter of 250 nm and with entrapment efficiency of magnetite 21.5 wt% and taxol 0.5 wt%. They were superparamagnetic, with saturation magnetization of 1.4 mT. Nevertheless, the prepared taxol loaded magnetic polymeric nanospheres still show sufficient magnetization for their magnetic properties to be useful from the point of view of magnetic carrier technology. The prepared TAXMNPs were used in in-vivo

experiments at treatment of melanoma cancer B16 in mouse . We found that after intravenous application of prepared TAXMNPs with application of the external magnetic field statistical important reduction of melanoma was observed.

2.4. Biological magnetite nanoparticles – magnetosomes

Application of magnetic materials for hyperthermia treatment of biological tissues with the goal of tumor therapy has been known in principle for more than four decades [24]. The heating effect depends strongly on the magnetic properties of the particles, which may vary appreciably depending on their size and microstructure. The magnetite particles can be either ferromagnetic or superparamagnetic, and the magnetic moment of single-domain particle relaxes through either Brownian or Neel relaxation depending on the anisotropy and size of the particle [25, 26]. It was shown by previous investigations that specific loss power (SLP) depends strongly on the mean particle size as well as the width of the size distribution [27–29]. The strong monotonous rise of SLP, nearly two orders of the magnitude, from15 kW/kg up to 900 kW/kg with an increasing particle core size from 7 nm up to 18.4 nm in magnetite, was described. This rise was clarified in the frame of the classical Debye theory of dispersions [28]. For the biocompatible magnetic iron oxides magnetite and maghemite, a maximum SLP was found above typical sizes of superparamagnetic particles but below the size of typical multidomainparticles. On the other hand, the SLP determined from hysteresis loops, susceptibility spectra and calorimetry with a maximum value of 960 kW/kg at 410 kHz and field amplitude of 10 kA/m was found for biological particles-magnetosomes with a mean size of about 35nm [30]. However, the magnetic and structural properties of magnetosomes have been insufficiently characterized up to now, mainly because of the unavailability of significant amounts of material. Magnetosomes, which can be obtained by a biomineralization process in magnetotactic bacteria (MTB), consist of magnetic mineral crystals magnetite or greigite [31] enveloped by a biological membrane that contains phospholipids and specific proteins [32]. The magnetosome membrane is not only critical for the control of crystal size and morphology, but it also prevents the aggregation of extracted magnetosomes and thus stabilizes magnetosome suspensions. Magnetosome crystals of MTB are typically from 30 to about 140 nm in diameter, i.e. within the single-magnetic-domain size range, which maximizes the efficiency of the particle as a permanent magnetic carrier [33]. In many magnetotactic bacterial types, the magnetosome are characterized by narrow particle size distributions. Whether the mineral particles are magnetite or greigite, the chain of magnetosome particles constitutes a permanent magnetic dipole fixed within the bacteria [34]. The remanent moment is generally close to its saturation value. Normally it is sufficiently larger than background thermal energy so that it, and consequently the bacteria, is oriented along geomagnetic field lines as it swims, causing the bacterium to migrate along the field lines. Because of their unique characteristics, magnetosomes have a high potential for nano- and biotechnological applications, which require a specially designed particle surface. Especially, in biotechnological applications, functionalized bacterial magnetosomes represent an attractive alternative to chemically synthesized iron oxide particles. Magnetosome particles have been applied in numerous applications that range from the extraction of magnetic resonance imaging (MRI), magnetic drug targeting, DNA and RNA to the highly sensitive detection and concentration of toxic substances and development of immunoassays [35]. One of the potential application areas of magnetosomes is magnetic particle hyperthermia (MPH) [36]. As pointed out recently an enhancement of specific heating power is of importance for reducing useful dosage applied to the tumor. Previous investigations on the suitability of magnetic nanoparticles for MPH have shown that for the biocompatible magnetic iron oxides a core size range above about 20 nm is advantageous with respect to large specific heating power. Therefore, magnetosomes are of particular interest for testing their suitability for application in MPH tumor therapy.

3. Magnetic hyperthermia effect

In our previous papers [37, 38], the structural, magnetic properties and heating effect of magnetosomes obtained by a biomineralization process in magnetotactic bacteria Magnetospirillum sp. Strain AMB-1 were reported. The heating effect of the magnetosome solution as the result of absorbing energy from the alternating magnetic field has shown that magnetosome suspensions are capable of delivering sufficient heating power which may be of interest for magnetic particle hyperthermia.

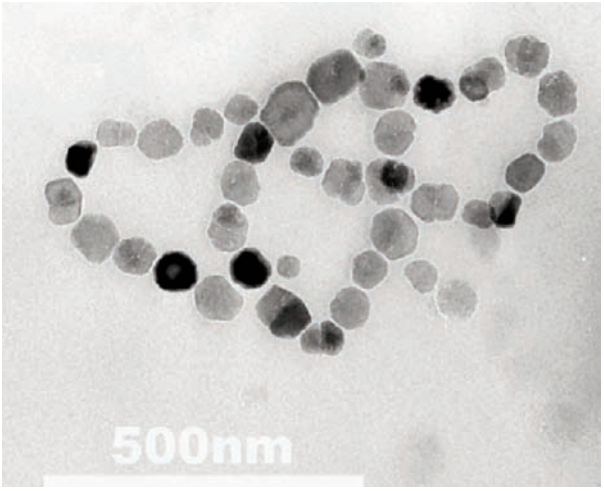

Fig. 4 Transmission electron micrograph of magnetosomes

Bacterial magnetosomes investigated in this contribution were synthesized by magnetotactic bacteria Magnetospirillum sp. strain AMB-1 in laboratory conditions. These bacteria are Gram-negative a-proteobacterium that are more oxygen-tolerant and easier to grow on a large scale. The detailed description of cultivation of magnetotactic bacteria and isolation of magnetosomes is given in our previous contribution [39]. Techniques for the isolation and purification of magnetosome particles from Magnetospirillum sp. are based on combination of centrifugation and the magnetic sep-

aration. Typically, 2.6 mg bacterial magnetite could be acquired from a 1000-mL culture of Magnetospirillum sp. AMB-1. These isolation and purification procedures leave the surrounding membrane intact and magnetosome preparations are apparently free of contaminating materials. Owing to the presence of the enveloping membrane, isolated magnetosomes particles form stable, well dispersed suspensions in water solution of HEPES (4-(2-hydroxyethyl)-1-piperazineethanesulfonicacid). For the study of heating characteristics of samples with magnetosomes we used the heating system described in [18] at the frequency of 750 kHz and AC-field amplitude in the range of (0–2.5) kAm^{-1}. The slope of the curve $T(t)$ is a measure of the power release in a unit volume. From the fitting of the function $(\Delta T/\Delta t) = (H/a)^n$ to the experimental data the parameters a and n were determined which depend on several factors such as particle permeability, conductivity, size, shape and distribution. The observed H^n -law-type dependence of the temperature increase rate $(\Delta T/\Delta t)_{t=0}$, on the amplitude of the magnetic field indicates the presence of superparamagnetic and partially ferromagnetic particles in the magnetic fluids studied since $n > 2$. The small amount of ferromagnetic particles causes energy losses associated with hysteresis and superparamagnetic particles cause energy losses associated with relaxation. On the basis of the obtained relation $(\Delta T/\Delta t)_{t=0} = (H/14063)^{2.31}$ the specific absorption rate (*SAR*) values were calculated. The *SAR* is defined as the amount of heat released by a unit weight of the material per unit time. It can be calculated from the expression $SAR_{sample} = C_s\,(\Delta T/\Delta t)$ [mW/g_{sample}] where C_s is the specific heat of the sample. The *SAR* data normalized with respect to the magnetite mass contents in the samples, m_{Fe} can be calculated from the expression:

$$SAR = \frac{\rho C_P}{m_{Fe}} \cdot \left(\frac{\Delta T}{\Delta t}\right)_{t=0} \quad \left[\frac{W}{kg_{Fe}}\right] \qquad (1)$$

where ρ is the density of the sample, $C_P \cong C_{water} = 4.18$ [$kJ \cdot K^{-1} \cdot kg^{-1}$] is the sample specific heat capacity, $m_{Fe} = \phi V \cdot \rho_{Fe} = 21$ [$kgFe \cdot m^{-3}{}_{sample}$] is the mass of magnetic material in the 1 m^3 sample and $\rho_{Fe} = 5180$ [$kg \cdot m^{-3}$] is the density of magnetite.

Densities ρ_0 and ρ of the carrier liquid and the magnetosome-based magnetic fluid, respectively, mass contents of magnetite in the samples, m_{Fe}, and the values of the parameters a and n determined from thermal measurements. Table2

ρ_0	ρ	Φ_V	m_{Fe}	a	N
$kg \cdot m^{-3}$	$kg \cdot m^{-3}$	%	$kg \cdot m^{-3}$	-	-
998	1002	1.1	21	12162	2.31

On the basis of the relation, $(\Delta T/\Delta t)_{t=0} = (H/12162)^{2.31}$, and the following expression for the power dissipated as heat in 1 g of magnetic material (magnetosome) was obtained:

$$SAR = 201 \cdot \left(\frac{H}{12162}\right)^{2.31} \quad \left[\frac{kW}{kg_{Fe}}\right] \qquad (2)$$

The dependence of *SAR* on the magnetic field with respect to the magnetite mass content in the sample calculated according Eq. (1) (at $f = 750$ kHz) is shown in Fig. 5. The found value for a specific absorption rate (SAR) 26 kW/kg at 5 kA/m and 750 kHz, which is comparable to those values of the MF-oleate system means that magnetosomes may be considered as good material for the biomedical applications in hyperthermia in the view of a phospholipidic biological membrane.

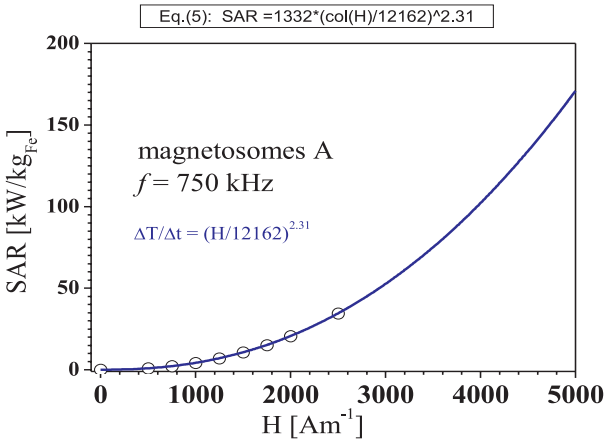

Fig. 5 SAR values for the sample at f = 750 kHz calculated with the aid of Eq (2)

The obtained results in the area of biomedical applications are very promising but there are several problems associated with magnetic drug targeting. These limitations include (i) the possibility of embolization of the blood vessel in the target region due to the accumulation of magnetic carriers, (ii) difficulties with scaling up from animal models due to larger distances between the target sites and the magnet, (iii) once drug is released, it is no longer attracted to the magnetic field and (iv) toxic responses to the magnetic carriers [31]. Recent pre-clinical and experimental results indicate, however, that it is still possible to overcome these limitations and use magnetic targeting to improve drug retention and also address safety issue.

4. Conclusion

In this contribution we have showed some aspects of preparation biocompatible magnetizable complex systems (nanoparticles, magnetic fluids, covalently binding of proteins and enzymes to magnetite nanoparticles, magnetoliposomes, encapsulation clinically important drugs (Indomethacin and Taxol) in biodegradable polymer nanospheres together with magnetite and their in vivo application, preparation and properties of biological magnetite nanoparticles – magnetosomes and their application in hyperthermia experiment. Greater understanding of the properties of magnetic particles and overcoming of some problems connected with biomedical application will enable the earlier implementation of laboratory results into clinical praxis.

Acknowledgement

The Slovak Academy of Sciences, in the framework of CEX Nanofluid, Projects VEGA 077 and 051, Project SAV-FM-EHP-2008-01-01 and the Slovak Research and Development Agency, in the framework of Projects APVV No. 0173-06, No. 0509-07 and Ministry of Education Agency for structural funds of EU in framework of projects No. 26220120021 and 26220220005.

References

[1] LUBE, A. S., BERGEMANN C. et al.: Cancer Res. 194 (1999) 149
[2] TORCHILIN, V. P.: Eur. J. Pharm. Sci. 11 Suppl. 2 (2000) S81
[3] DAVIS, S. S.: Trends Biotechnol., 15 (1977) 217
[4] MECHTA, R. V., UPHADAY, R. V., CHARLES, S.W., RAMCHAND, C. N.: Biotechnol. Techn. 11, (1997) 493
[5] KONERACKA, M., KOPCANSKY, P., TIMKO, M., ANTALIK, M., RAMCHAND, C. N., LOBO, D., MECHTA, R., UPHADAY, R. V.: J. Magn. Magn. Mat. 201 (1999) 427
[6] KONERACKA, M., KOPCANSKY, P., TIMKO, M., RAMCHAND, C. N., DE SEQUEIRA, A., TREVAN, M.: J. Mol. Catalysis B Enzymatic 18 (2002) 13
[7] BERRY, C. C., CURTIS, A. S. G.: J. Phys. D: Appl. Phys. 36 (2003) R198
[8] BACRI, J. C., SALIN, D., MASSART, R.: J. Magn. Magn. Mater. 85 (1990) 27.
[9] PACKER, L., TRISTRAM, S., HERZ, J. M., RUSSEL, C., BORDERS, L. C.: FEBS Lett. 108 (1979) 243
[10] ZAVISOVA, V., KONERACKA, M., TOMASOVICOVA, N., KOPCANSKY, P., TIMKO, M.: Z. Phys.Chem. 220 (2006) 241
[11] DE CUYPER, M., JONIAU, M.: Langmuir 7 (1991) 647
[12] XU, Y., SZOKA, F. C.: Biochemistry 35 (1996) 5616.
[13] GABER, M. H., HONG, K., HUANG, S. K., PAPAHADJOPOULOS, D.: Pharm Res 12 (1995)1407
[14] MEYER, O., PAPAHADJOPOULOS, D., LEROUX, J-C.: FEBS Lett 421 (1998) 61
[15] KONERACKA, M., KOPCANSKY, P., SOSA, P., BAGELOVA, J., TIMKO, M.: J. Magn. Magn. Mater. 293 (2005) 271
[16] HICKEY, T., KREUTZER, D., BURGESS, D. J., MOUSSY, F.: Biomaterials 23 (2002) 1649.
[17] MIDDLETON, J. C., TIPTON, A. J.: Biomaterials 21 (2000) 2335.
[18] TIMKO, M., KONERACKA, M., KOPCANSKY, P., TOMASOVICOVA, N., ZAVISOVA V.: J. Magn. Magn. Mat. 300 (2006) e191–e194
[19] ZAVISOVA, V., KONERACKA, M., STRBAK, O., TOMASOVICOVA, N., KOPCANSKY, P., TIMKO, M., VAVRA, I.: J. Magn. Magn. Mat. 311 (2007) 379–382
[20] FONSECA, C., SIMES, S., GASPAR, R.: J. Control. Rel. 83 (2002) 273.
[21] WANI, M. C., TAYLOR, H. L., WALL, M. E. et al.: J. Am. Chem. Soc. 93 (1971) 2325
[22] KONERACKA, M., MUCKOVA, M., ZAVISOVA, V., TOMASOVICOVA, N., KOPCANSKY, P., TIMKO, M., JURIKOVA, A., CSACH, K., KAVECANSKY, V., LANCZ, G.: J. Phys.: Condens. Matter 20 (2008) 204151
[23] KONERACKA, M., MUCKOVA, M., ZAVISOVA, V., TOMASOVICOVA, N., KOPCANSKY, P., TIMKO, M., LANCZ, G., PATOPRSTA, B., BARTOS, P., FABIAN, M.: J. Mag. Mag. Mat. 321 (2009) 1613
[24] CHAN, D. C. F., KIRPOTIN, D. B., BUNN, P.A. Jr.: J. Magn. Magn. Mater. 122 (1993) 374.
[25] JORDAN, A., SCHOLZ, R., WUST, P., SCHIRRA, H. et al.: J. Magn. Magn. Mater. 194 (1999) 185.
[26] ROSENSWIEG, R. E.: J. Magn. Magn. Mater. 252 (2002) 370.
[27] ATSUMI, T., JEYADEVAN, B., SATO, Y., TOHJI, K.: J. Magn. Magn. Mater. 310 (2007) 2841.
[28] HERGT, R., HIERGEIST, R., ZEISBERGER, M., GLOCKL, G., WEITSCHIES, W., RAMIREZ, L. P., HILGERD, I., KAISER, W.A.: J. Magn. Magn. Mater. 280 (2004) 358.
[29] HERGT, R., HIERGEIST, R., HILGER, I., KAISER, W.A., LAPATNIKOV, Y., MARGEL, S., RICHTER, U.: J. Magn. Magn. Mater. 270 (2004) 345.
[30] HERGT, R., HIERGEIST, R., ZEISBERGER, M., SCHULER, D., HEYEN, U., HILGER, I., KAISER, W.A.: J. Magn. Magn. Mater. 293 (2005) 80.
[31] FRENKEL, R. B., BLAKEMORE, R.: Science 203 (1979) 1355.
[32] SCHULER , D.: Arch. Microbiol. 181 (2004) 1.
[33] BUTLER, R. F., BANERJEE, S.: J. Geophys. Res. 80 (1975) 4049
[34] FRENKEL, R. B.: Ann. Rev. Biophys. Bioeng. 13 (1984) 85
[35] SCHULER, D.: J. Molec. Microbiol. Biotechnol. 1 (1999) 79.
[36] MOROZ, P., JONES, S. K., GRAY, B. N.: Int. J. Hyperthermia 18 (2002) 267.
[37] TIMKO, M., DZAROVA, A., KOVAC, J., KOPCANSKY, P., GOJZEWSKI, H., SZLAFEREK, A.: Acta Physica Polonica 115 (2009) 381
[38] TIMKO, M., DZAROVA, A., KOVAC, J. et.al.: J. Mag. Mag. Mat. 321 (2009) 1521
[39] TIMKO, M., DZAROVA, A., ZAVISOVA et. al.: Magnetohydrodynamics Journal 44 (2008) 3.

Julius Stelina – Ctibor Musil *

SOME EFFECTS OBSERVED IN THE MAGNETIC FLUID UNDER THE INFLUENCE OF QUASI-HOMOGENEOUS MAGNETIC FIELD

The effect of homogenous external magnetic fields on the created space structure of a nanoparticle distribution in a sample of magnetic fluid was studied. A grating was formed by the interference field of two crossed Ar-laser beams. The magnetic field was formed by using two electromagnets. The magnetic field oriented parallel to strips of grating does not significantly change the shape of nanoparticle grating. Perpendicular direction of magnetic field causes redistribution of the nanoparticles and in consequence of that the perpendicular nanoparticle "quasi-grating" arised.

1. Introduction

Magnetic fluids are colloidal suspensions of ferromagnetics nanoparticles dispersed in a nonmagnetic carrier liquid and the investigation of it is very interesting from several points of view. As the suspensions of magnetic nanoparticles, they exhibit liquid behaviour combined with the superparamagnetic properties. Consequently, they are useful in various applications, as the magnetic control of their flow can be realized by attainable values of the magnetic field strengths. Another application is spanning from sealants in rotary shaft to head dissipaters in loud speaker coils to carrier liquids for medical substances e.g. Nanoparticles of magnetic materials with the typical diameter of 10 nm are large enough to have extremely small particle mobility. This leads to a situation where the typical redistribution time constants are extremely large. On the other hand, the typical manifestation of these conditions is the behaviour of the nanoparticles in conditions of the created inhomogenities.

On top of it, fluids can be influenced by magnetic field. When additional energy is imported by a light beam and a spatial structure is thus created (grating for instance), it results in appearance of diffusion- and termodiffusion fluxes. The total nanoparticle flux will be given not only by its diffusion part but also by the properties of the termodiffusion mechanisms, mainly by the temperature behaviour of the Soret constant [1, 2] and their dependence on the magnetic field in the equation

$$i = -D_0(1 + D^m)\cdot\frac{\partial n}{\partial x} - D_0(1 + D^m)\cdot \cdot S_T\left(S_T^0 + S_T^m\right)\cdot n\cdot\frac{\partial T}{\partial x}$$

where the first term on the right hand side is the diffusion flux, the second is the thermo-diffusion flux of the particles. D_0 is the diffusion constant of particles, S is the thermo-diffusion coefficient (the Soret constant), n is the particle concentration, T is the temperature and D^m and S_T^m take into consideration the influence of the magnetic field [3], [4].

Experimentally it can be verified that particles can accumulate (under specific conditions) at places of the lower temperature (for $S > 0$), or at places where the temperature is higher (for $S < 0$). The spatial redistribution of the nanoparticle concentration depends on sighn of parameter S. As far as the nanoparticle concentration explicitly affects the local optical properties of the ferrofluid, this can be used for the investigation of the processes mentioned above by means of optical methods.

2. Experimental results

In this article the study of nanoparticle kinetics in the magnetic liquid under the influence of the external magnetic field is presented. The study was carried out using a diagnostic laser beam (λ = 633 nm) and its diffraction on the nanoparticle diffraction grating which was generated by two crossing Ar laser beams (λ = = 488 nm) through the interference field.

The relative position of the diffraction grating and magnetic induction vector $\vec{B}$ can be oriented according to Fig. 1. The direction of the strings of the grating was always in the direction of $\boldsymbol{x}$ axis, and the diagnostic (λ = 633 nm) beam was always in the direction of $\boldsymbol{z}$ axis. In this article the magnetic field influence in the axes $\boldsymbol{x}$ and $\boldsymbol{y}$ is presented only.

The experiments were carried out on a magnetic liquid sample based on kerosene with dispersed nanoparticles Fe_2O_3 of about 10 nm diameter. The thickness of the cell was about 65 μm.

* **Julius Stelina, Ctibor Musil**
Department of Physics, Faculty of Electrical Engineering, University of Zilina, Slovakia, E-mail: stelin@fel.uniza.sk

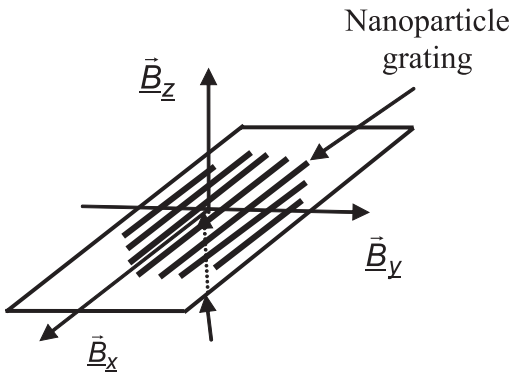

Fig. 1 Relative position of diagnostic laser beam, magnetic induction vector and nanoparticles grating

The basic scheme of the apparatus used for the study of nanoparticle kinetics in the dispersion fluids is in Fig. 2.

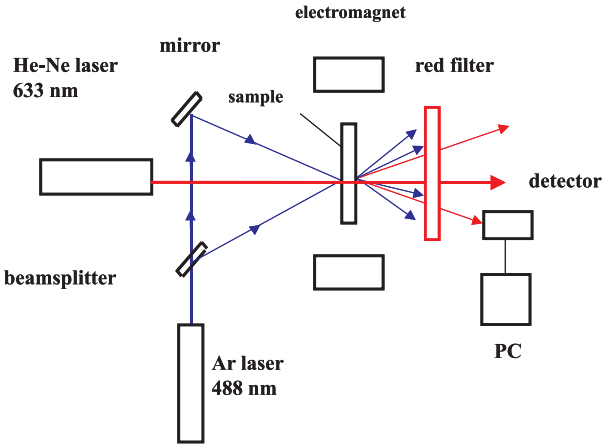

Fig. 2 The basic scheme of the apparatus

2.1. The experimental results of the study for magnetic field B_x

In this case the magnetic field is oriented in direction of the grating fringes (*x* direction) and lies in the plane of the created diffraction grating (see Fig. 1).

Fig. 3 shows a creation of the nanoparticle grating by the interference field of two crossed coherent laser beams with λ = 488 nm and its spontaneous decay. Fig. 4 presents the same case as Fig. 3 but the decay is under the influence of additional lighting beam λ = 488 nm and 6 mW/mm^2 power. We can see that the additional lighting beam stops or reduces the decay of the nanoparticle grating. Probably the thermo-diffusion (Soret) coefficient is negative in this phase of process.

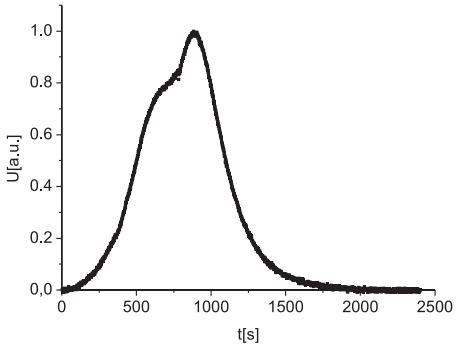

Fig. 3 The time dependence of the rise and decay of the nanoparticle grating without additional lighting

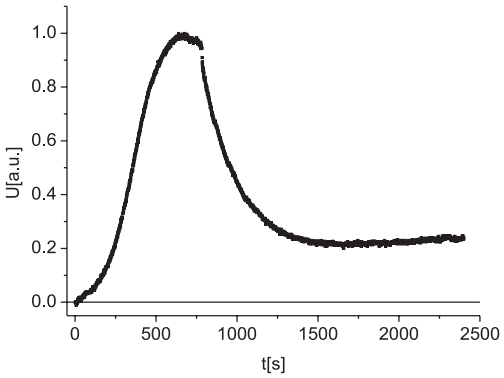

Fig. 4 The time dependence of the rise and decay of the nanoparticle grating with additional lighting of 6 mW/mm^2

The influence of the intensity of the magnetic field on the stability of the diffraction grating is presented by diffraction efficiency on the diffraction nanoparticle grating and is shown in Figs. 5.

Figs. 5a to 5d show a decay of the nanoparticle grating under the influence of quasi-homogenous direct external magnetic field with values 8 mT, 16 mT, 24 mT, 30 mT and the additional lighting beam λ = 488 nm and 6 mW/mm^2 power was present as well. In the figures we can see that the presence of external magnetic

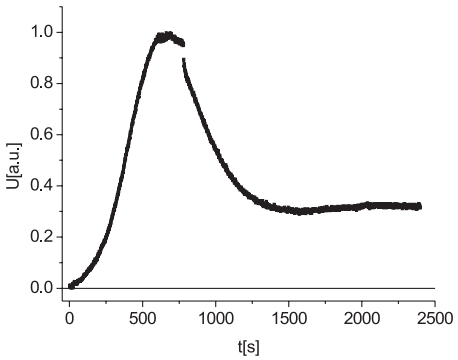

Fig. 5a The decay of the grating at B = 8 mT

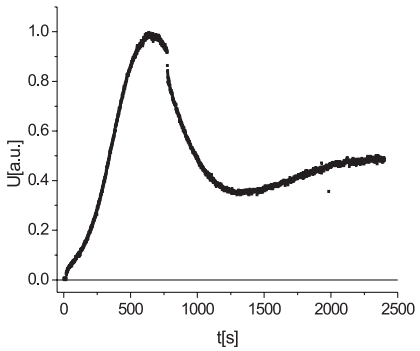

Fig. 5b The decay of the grating at B = 16 mT

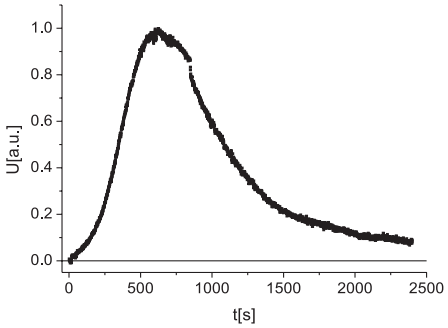

Fig. 5c The decay of the grating at B = 24 mT

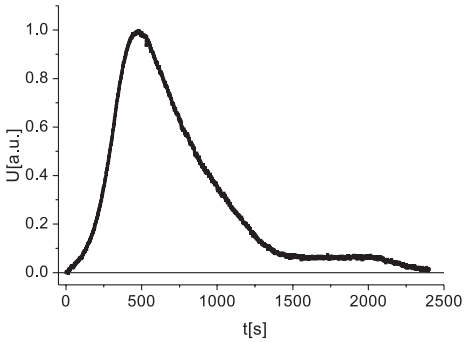

Fig. 5d The decay of the grating at B = 30 mT

field at the magnetic induction higher than 16 mT causes a quick decay of the nanoparticle grating and does not stabilise it.

The presence of the external magnetic field without additional lighting beam does not stabilise the nanoparticle grating at all.

Conclusions

1. As was discovered in the past [6], the additional lighting with a suitable wavelength, i.e. such wavelength that is absorbed in the sample and that induces the rise of a suitable temperature gradient between the strips of the grating, can stabilize the grating or eventually make it of a better quality.
2. But if at the same time a magnetic field is applied in the direction of the strips of the grating and in their plane, a better quality of the grating is observed at first. When the value of the magnetic field is above 16 mT, the stabilizing effect of the additional lighting is removed (Fig. 5d).

2.2. The experimental results of the study for magnetic field B_y

In this case the nanoparticle grating is oriented again in the ***x*** direction and external magnetic field is oriented perpendicularly to the grating strips, i.e. in the y direction and lies in the plane of the created diffraction grating (see Fig. 1).

In Figs. 6 and 7 the created nanoparticle grating and diffraction on it are shown.

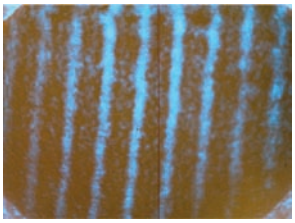

Fig. 6 Original nanoparticle grating

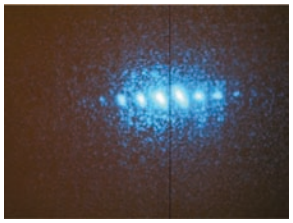

Fig. 7 Diffraction on the original grating

Fig. 8 shows the state of the nano-particle grating cca 5 s after switching on the perpendicular external magnetic field with B = = 10 mT intensity and Fig. 9 shows the diffraction on it. These figures illustrate a decay of the original grating. The decay of original grating is accompanied with the formation new one in perpendicular direction. This new grating is not exactly regular (therefore we call it "quasy-grating"). The diffraction on it is shown in Fig. 10.

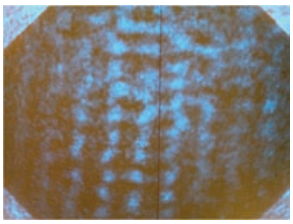

Fig. 8 The grating after switch on magnetic field.

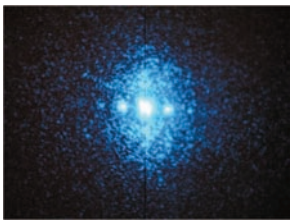

Fig. 9 The diffraction on the knew quasi-grating at the moment switch on of the magnetic field.

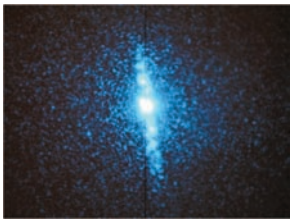

Fig. 10 Diffraction on the perpendicular new quasi-grating after some time.

The visage of the new "quasy-grating" 20 s and 1200 s after the external magnetic field was switched on can be seen in Figs. 11 and 12.

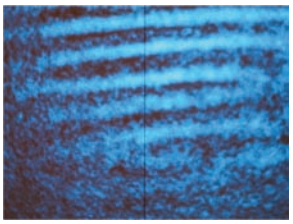

Fig. 11 The perpendicular nanoparticle quasi- grating after 20 s

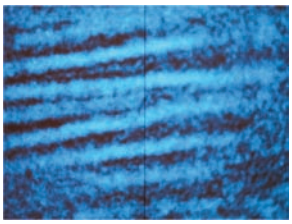

Fig. 12 The perpendicular nanoparticle quasi-grating after1200 s

The creation of the new "quasy-grating" in the time record of the diffraction efficiency can be seen in Fig. 13.

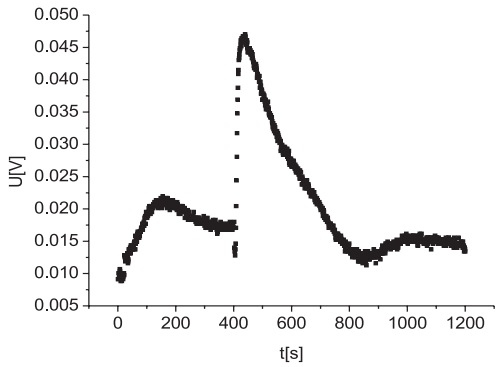

Fig. 13 The time dependence of the generation and decay of the first diffraction maximum which represent the arise of the perpendicular quasi-grating

The regular nanoparticle grating was generated through the interference field for the duration of 400 s. The detector was placed into an expected position of the first diffraction maximum of the arising "quasi-grating". In the moment of 400 s (see Fig.13) one of the two interfering beams was switched off and the external magnetic field 10 mT was switched on in the same time and

Fig. 14 The structural shape of the nanoparticle grating strings after 1080 s from the beginning of the additional lighting

the new "quasi-grating" arises very quickly (cca in 15 s). In consequence of the used external magnetic field, which compensate influence of the additional lighting beam, the "quasi- grating" quick decay.

One argument for forming the perpendicular (in y direction oriented) "quasi-grating" is due to the cluster structure of strings of the original nanoparticle grating (illustrate Fig. 14). The influence of the external magnetic field probably causes transversal connection of the clusters in the strings. Because the cluster structure is not correctly periodical neither the forming transversal "quasi-grating" is not correctly periodical.

3. Conclusions

1. The nanoparticle grating was created in the sample of magnetic fluid.
2. To the created grating the transversal magnetic field $B = 10$ mT and additional lighting $P_L = 5$ mW/mm^2 was applied.
3. Relatively quickly (15 s) the quasi-grating transversal to the original nanoparticle grating was generated and it was observed directly on the ground glass or through the diffraction on it.
4. Probably the quasi-grating is created due to the cluster structure of the nanoparticle grating (Fig. 14) [5] and the influence of the transversal magnetic field.

Acknowledgements

This work has been supported by Slovak Grant Agency VEGA under project No. 2/0077/09

References

[1] MEZULIS, A., BLUMS, E., BOURDON, A., DEMOUCHY, G.: *Thermodiffusion- Induced Optical Index Grating in Ferrocolloids: Determination of Transport Coefficients,* Proc. of Fourth International PAMIR conf. on MHDDTM, Presquile de Giens, France, 2000, 781

[2] KITA, R., KIRCHER, G., WIEGAND, S.: *Thermally Induced Sign Change of Soret Coefficient for Dilute and Semidilute Solution of Poly(N-isopropylacrylamide) in Ethanol*, J. Che. Phys. 121(18), 2004, p. 9140

[3] VOLKER, T., ODENBACH, S.: *Physics of Fluids,* Vol. 15, 8/2003

[4] BLUMS, E., ODENBACH, S., MEZULIS, A., MAIOROV, M.: *Physics of Fluids,* Vol. 10, 2155, 1998

[5] STELINA, J., MUSIL, C., BRACINIK, J., KOPCANSKY, P., TIMKO, M., TOMCO, L.: *Proc. of 7th International Conference on Applied Physics of Condensed Matter*, 2006, p. 256.

[6] MUSIL, C., STELINA, J., KOPCANSKY, P., TIMKO, M.: *The Influence of an External Paralel Magnetic Field on a Nanoparicle Grating Created in a Magnetic Fluid,* 17th Conference of Slovak Physicists, 2009, Bratislava, p. 109

Jozef Kudelcik – Peter Bury – Vlasta Zavisova – Milan Timko – Peter Kopcansky *

THE DIELECTRIC BREAKDOWN OF MAGNETIC FLUIDS

The development of dielectric breakdown and the DC dielectric breakdown voltage of magnetic fluids based on inhibited transformer oil ITO 100 were investigated in parallel orientations of external magnetic field. It was shown that the breakdown voltage is strongly influenced by the magnetic nanoparticles. The magnetic fluids with the volume concentration of 1% had better dielectric properties than pure transformer oil. The increase of breakdown voltage was interpreted on the base of the bubble theory of breakdown.

Keywords: transformer oil, magnetic fluid, relative permittivity, breakdown voltage

1. Introduction

Magnetic fluids based on inhibited transformer oil ITO 100 have been shown to provide thermal and dielectric benefits to the power transformers. They can improve transfer of heat by enhancing the fluid circulation within transformer windings [1], while also minimizing the effect of moisture on typical insulating fluids. Better dielectric properties of magnetic fluids than pure transformer oil and the use as high-voltage insulation was found for low volume concentration of 0.1% [2, 3]. Such transformer oil shows the strong dependence of dielectric breakdown strength on aggregation effects of magnetic nanoparticles [3].

A magnetic fluid is a colloidal suspension of nano-sized magnetic particles covered with a surfactant layer in a carried liquid. Particles of this size are monodomain and interaction between them may lead to their agglomeration and subsequent sedimentation. To avoid these undesired side effects magnetic particles can be coated with a surfactant that produces entropic repulsion. The macroscopic magnetic properties of the magnetic fluid are determined by the orientation of magnetic moments of nanoparticles in the external magnetic field. An externally applied magnetic field induces ordering of magnetic moments of the particles giving rise to magnetization of the sample as a whole and can cause certain amount of colloidal particles to join into clusters as long as hundreds of nanometers or more [4, 5].

The aim of the research reported in this article was to study the dielectric properties and DC dielectric breakdown voltage of magnetic fluids based on ITO 100 transformer oil. The effect of external magnetic field induced structuralization of magnetic particles in magnetic fluid on the dielectric properties were studied too.

2. Experimental setup and results

Fig. 1 shows the schematic diagram of the experimental setup, which includes HVdc power supply TESLA BS 221 (max voltage 10 kV and current 3 mA), electrode system, electric diagnostics and electromagnet. Sphere-to-sphere Cu electrodes with radius of 1 cm and plane-to-plane Cu electrodes with radius of 2.7 cm were used as the electrode system. The distance of electrodes was measured by metric gauge blocks with accuracy of 0.01 mm. New and unfiltered transformer oil – ITO 100 was filled into a discharge chamber (0.2 dm^3) and electrodes were again cleaned after series of 7 breakdowns. The capacitor value of 1 nF and resistance of 1 MΩ were chosen. The applied voltage and current were measured using a high voltage probe (E253/01, 10 MHz) and a Rogowski coil (Pearson Current monitor 110A, 10 kA, 20 MHz, 20 ns). The signals were recorded on Agilent technologies DSO3202A, 200 MHz digital oscilloscope. The time developments of resistance of magnetic fluids were measured using C.A 6549 Megaohmeter.

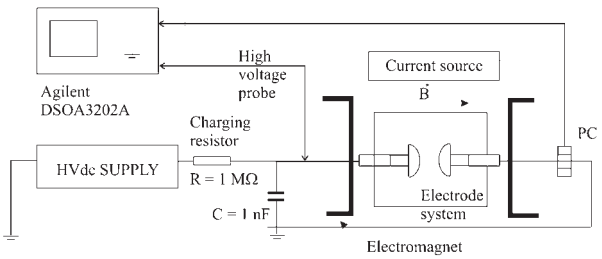

Fig. 1 The experimental setup

The magnetic fluids used in experiments consisted of magnetite particles ($FeO.Fe_2O_3$), the mean diameter D = 10.6 nm, coated

* **Jozef Kudelcik[1], Peter Bury[1], Vlasta Zavisova[2], Milan Timko[2], Peter Kopcansky[2]**
[1] Department of Physics, Faculty of Electrical Engineering, University of Zilina, Slovakia, E-mail: kudelcik@fyzika.uniza.sk
[2] Department of Magnetism, Institute of Experimental Physics SAS, Kosice, Slovakia

with oleic acid as a surfactant, dispersed in inhibited ITO 100 transformer oil. The original magnetic fluid used in our experiment had density equal to 1.071 g/cm^3 and its saturation magnetization was 8.81 mT. From this magnetic fluid and pure ITO 100 transformer oil the magnetic fluids with volume fractions 0.2 %, 1 % and 2 % were prepared. The acoustic velocity in these magnetic fluids without magnetic field is c = 1652 m/s (25 °C).

Each value of the breakdown voltage was measured seven times and the maximum and minimum values were omitted in the calculation of its mean value according to the rules of high voltage techniques [6]. Time intervals between breakdowns were 5 minutes. The experimental error of the breakdown voltage determination was ±10%.

One of parameters that determine the quality of transformer oil is the isolation resistance. This parameter gives information on isolation stage which can be decreased by water content, solid impurities and gases dissolved in oil [7]. Transformer oil or magnetic fluids were in the electrode system with plane-to-plane Cu electrodes and the measurements were made at 500 V DC by Megaohmeter. The isolation resistances were measured at following times: 15, 30, 40 and 60 seconds. From measured values the polarization index p calculated as: $p = R_{60}/R_{15}$, which is also important in transformers diagnostics, can be determined. Values of insulation resistance and polarization index observed for various times are in Table 1.

The resistance of transformer oil and magnetic fluids summarized for various times. Table 1

Liquid	R_{15} [GΩ]	R_{30} [GΩ]	R_{40} [GΩ]	R_{60} [GΩ]	p
ITO 100	335	372	394	430	1.28
0.2% MF	5.25	5.43	5.52	5.6	1.06
2% MF	0.83	0.76	0.77	0.77	0.92

When the insulation resistance of transformer oil is higher than 100 GΩ and increases with time (Table 1, ITO 100) it can be used in transformer [8]. Otherwise, there can be some problems in the insulation stage. In our case the magnetic fluid was prepared from nanoparticles and new inhibited ITO 100 transformer oil. ITO 100 was without impurities. In this case, the decrease (Table 1) of the insulation resistance of magnetic fluid was caused by the presence of magnetic nanoparticles. From these results follows that this type of diagnostic method for determination of quality of insulation stage cannot be used for magnetic fluid based on transformer oil.

Development of arc currents in oil and magnetic fluids are presented in Fig 2. The arc current is characterized by under-damped oscillation with angular frequency [9, 10]. The angular frequency is the function of electrode distance, type of liquid and outer parameters. As it can be seen from Fig. 2 the angular frequency is smaller for magnetic fluids. The angular frequency decreased with volume concentration of magnetic fluid. Amplitude and duration of arc current were changed with applied voltage at identical electrode distance and the magnetic fluid. The angular frequency did not changed with applied voltage. The measurements were also made at various electrode distances (0.1 – 0.6 mm) and similar developments and characteristics of arc currents were observed (Fig. 2)

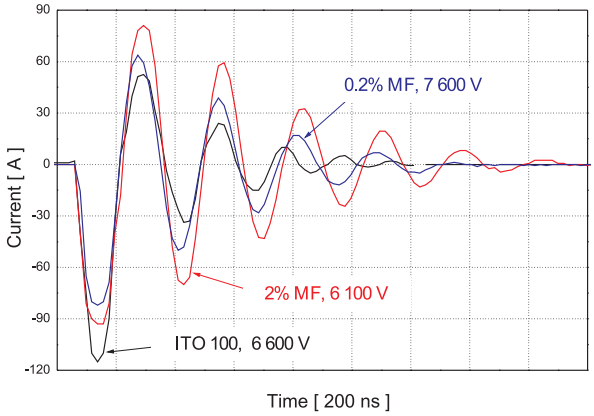

Fig. 2 The time dependence of arc current in transformer oil, 0.2 % and 2 % magnetic fluid with applied voltage (distance between the electrodes d = 0.4 mm).

The breakdown voltage or dielectric strength is the main measured parameter for determination of quality of insulating fluids. Fig. 3 illustrates the dependencies of the DC breakdown voltage on the distance between the electrodes for transformer oil and two volume concentrations of magnetic field. The measurements in the case of magnetic liquid were performed also in the external magnetic field (20 mT) in parallel orientation with the electric field (Fig. 1). Magnetic fluid was placed in the external magnetic fields during the whole measurement of the breakdown voltage.

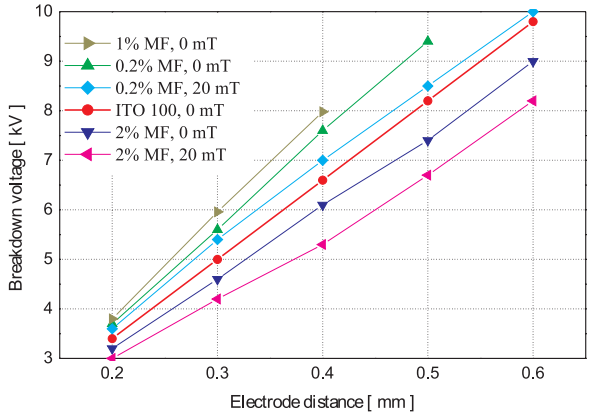

Fig. 3 The breakdown voltage versus distance between the electrodes for ITO 100 transformer oil and magnetic fluids (0.2 %, 1 % and 2 %) without the external magnetic field (B = 0 mT) and in the external magnetic field (B = 20 mT).

The breakdown voltage of 0.2% and 1% magnetic fluid is higher than those of the transformer oil, even also in the magnetic field. These properties are worse in 2% magnetic fluid. This is in agreement with the observation for the DC impulse voltage of Segal [1] and Marton [2, 3] for both DC and AC voltage.

3. Discussion

The change of the breakdown voltage of magnetic fluid with different volume concentration can be interpreted using theory of breakdown transformer oil. This theory is based on the bubble mechanism of breakdown, which is supported by various experimental works [11–16]. The main aspect is formation of bubbles (small channels [9]), regions with smaller density than surrounding liquid. These bubbles are formed by local heating and field-emitted electron injected in electrode space. By increasing voltage these regions grow and expand until their local density is reduced under a critical density [11] enough to take place in electron impact ionization. In the next phase, electron avalanches expand and create an ionizing front – primary streamer or streamers. When one of the streamers bridges the inter-electrode gap, plasma channel is generated and the breakdown can be observed. In the final stage of breakdown the energy stored in a capacitor is transformed to arc discharge and under damper oscillation of arc current can be observed [9, 10].

From previous we know that the value of breakdown voltage depends on creation of bubbles and processes running inside. When magnetic nanoparticles (e.g. magnetite Fe_3O_4) are added to transformer oil, there is negative effect on the formation of bubbles. The magnetite nanoparticles in transformer oil have extremely short charging time [16], so they are excellent electron traps. Trapped fast electrons are lost for ionization process and slow negative nanoparticles are produced. These negative ions also caused the decrease of electric field which had negative effect on ionization process. Nanoparticles are polarizable and have higher permittivity than the surrounding liquid, so they move by electrical force to the place of maximum of electrical intensity. This place is also the place of the creation and existence of bubbles. Therefore, when the formation and existence of bubbles are affected by magnetic nanoparticles, it results in the increase of breakdown voltage. This is observable only for small concentration of magnetic fluid, as in our case 0.2 % and 1% (Fig. 3) [2, 3].

When magnetic fluid has higher volume concentration of magnetic particles (2 %, Fig. 3) we must take into account another effect. The magnetic nanoparticles are again moved to the place of maximum stress but their high concentration is presumed to be initiated by the surface irregularities on the electrodes and formations of the chains, which give rise to local field gradients. The accumulation of particles continues and tends to form a bridge across the gap, which leads to the breakdown initiation. In external magnetic field is the decrease of the breakdown voltage due to the magnetic dipol-dipol interaction between the particles and formations of the chains and chain-like elongated clusters [4, 5].

Water content is one of the main parameters, which can cause the decrease of the insulation resistance. Also small solid impurities and gases dissolved in oil have the same influence. In these experiments the decrease of insulation resistance was not caused by these impurities, because new ITO 100 transformer oil was used. The decrease of insulation resistance is uniquely determined by the presence of magnetic nanoparticles in these measurements. From these results it follows that when transformed oil contained magnetic nanoparticles the diagnostic method of the isolation resistances test cannot be used.

4. Conclusion

The insulating properties of magnetic fluid based on transformer oil with a small volume concentration (0.2 % and 1 %) of magnetite nanoparticles were better in comparison with pure transformer oil. The presence of small concentration of magnetic nanoparticles has a profound effect on the breakdown voltage of liquid insulators. For 2 % magnetic fluid the situation was opposite, the insulation properties were worse and breakdown voltage was also smaller. The change of breakdown voltage was interpreted on the base of the bubble theory of breakdown.

Acknowledgements

The authors wish to thank for the support to the R&D operational program Centre of excellence of power electronics systems and materials for their components. The project is funded by the European Community, ERDF – European regional development fund.

References

[1] SEGAL, V., RAJ, K.: *An Investigation of Power Transformer Cooling with Magnetic Fluids,* Indian J. Eng. Mater. Sci. 5 (6), pp. 416–422, 1998,

[2] KOPCANSKY, P., TOMCO, L., MARTON, K., KONERACKA, M., TIMKO, M., POTOCOVA, I.: The DC Dielectric Breakdown Strength of Magnetic Fluids Based on Transformer Oil, Journal of Magnetism and Magnetic Materials, vol. 289, pp. 415–418, 2005.

[3] TOMCO, L., MARTON, K., HERCHL, F., KOPCANSKY, P., POTOCOVA, I., KONERACKA, M.: *The DC and DC Insulating Properties of Magnetic Fluids Based on Transformer Oil*, Phys. sta. sol (c) , 1/2006, pp. 195–198.

[4] JOZEFCZAK, A.: *Study of Low Concentrated Ionic Ferrofluid Stability in Magnetic Field by Ultrasound Spectroscopy,* Journal of Magnetism and Magnetic Materials, vol. 294, 2009 Article in Press,

[5] BRAMANTYA, M. A., MOTOZAWA, M., TAKUMA, H., FAIZ, M., SAWADA, T.: *Experimental Analysis of Clustering Structures in Magnetic and MR Fluids Using Ultrasound,* Journal of Physics: Conference Series, vol. 149, 012040, 2009,
[6] KUFFEL, E., ZAEUNGL, W.S.: *High Voltage Engineering Fundamentals,* Pergamon Press, Oxford, 1984,
[7] GUTTEN, M., KORENCIAK, D.: *Frequency Diagnostics Options of Transformers,* In Diagnostika '09, Plzen 2009, pp. 78–81,
[8] http://www.megger.com/eu/index.php
[9] KUDELCIK, J.: *Development of Breakdown in Transformer Oil,* ADVANCES in Electrical and Electronic Engineering 6, pp. 35–39, 2007,
[10] KUDELCIK, J., GUTTEN, M.: *Measurement of Electrical Parameters of Breakdown in Transformer Oil,* In 7th International Conference on Measurement, Smolenice 2009, pp. 393–396,
[11] JONES, H. M., KUNHARDT, E. E.: *Development of Pulsed Dielectric Breakdown in Liquids,* Journal of Physics D: Applied physics, vol. 28, pp. 178–188, 1995,
[12] DEVINS, J. C., RZAD J., SCHWABE, R. J.: *Breakdown and Prebreakdown Phenomena in Liquids,* Journal of Applied Physics, vol. 52, pp. 4531–4545, 1981,
[13] BEROUAL, A.: *Electronic and Gaseous Processes in the Prebreakdown Phenomena of Dielectric Liquids,* Journal of Applied Physics, vol. 73, pp. 4526–4533, 1993,
[14] TIMOSHKIN, V. et all: *Hydrodynamic Modeling of Transient Cavities in Fluids Generated by High Voltage Spark Discharges,* J. Phys. D.: Appl. Phys., vol. 39, pp. 4808–4817, 2006,
[15] KUDELCIKOVA, M.: *Positive Solutions of Delayed Differential Equation,* In Modelling & Stability: international conference Dynamical system modelling and stability investigation, Kyjev, 2009, pp. 29–30.
[16] HWANG, J. G., O'SULLIVAN, F., ZAHN, M., HJORTSTAM, O., PETTERSON, L., LIU, R.: *Modeling of Streamer Propagation in Transformer Oil-based Nanofluids,* Annual Report – Conference on Electrical Insulation and Dielectric Phenomena, Article number 4772777, pp. 361–366 , 2008.

Peter Hockicko – Francisco Munoz – Peter Bury – Peter Sidor *

ANALYSIS OF ACOUSTIC ATTENUATION SPECTRA OF LIPON GLASSES

The acoustic attenuation spectra which reflect the basic features of the relaxation and transport processes of the mobile ions of investigated phosphate and oxynitride phosphate glasses are analyzed. Suitable theoretical models and mathematical fit of acoustic spectra are used for characterization of the ionic hopping motion, relaxation processes and transport mechanisms connected with the mobility of conductive ions. Results from acoustic measurements are compared with results obtained from electrical conductivity measurements.

1. Introduction

One of the most important requirements of the electrolyte materials in battery application is high ionic conductivity. Using solid electrolytes in rechargeable batteries can provide numerous advantages such as thermal and mechanical stability, high reliability, longer active life, the possibility of miniaturization through thin-film production.

Lithium-ion conductive glasses have been widely studied due to their potential application as solid-state amorphous electrolytes in secondary batteries [1]. Lithium metal can be used as the anode material in lithium batteries and it allows higher energy and power densities than when graphitized anodes are used as anode materials. It was found that the amorphous character of the material and the presence of nitrogen increase the conductivity with respect to that of the crystalline compound. The increase in conductivity is supposed to be related to the formation of P–N bonds, which replace P–O ones leading to a more reticulated anionic network [2].

The optical and electrochemical properties of lithium phosphorous oxynitride (LiPON) thin films have been studied and successfully applied in lithium microbatteries [3]. LiPON exhibits a single, Li^+-ion conducting phase with an average conductivity of $(2.3 \pm 0.7) \times 10^{-6}$ S/cm at 25 °C and an average activation energy of $E_a = (0.55 \pm 0.02)$ eV [3].

The acoustic attenuation measurement seems to be a useful technique for nondestructive investigation of transport mechanisms in conductive glasses and compared to the electrical ones it has even some advantages as high sensitivity, the absence of contact phenomena and so on [4, 5]. Acoustical measurements made over a wide range of frequencies and temperatures can characterize different relaxation processes according to corresponding transport mechanisms due to the strong acousto-ionic interaction. In glassy electrolytes, the mobile ions encounter different kinds of site and ionic hopping motion and relaxation processes connected with charge mobility so that modified jump relaxation model [6, 7] can be used for transport mechanisms description.

In this contribution we present first results from acoustic investigation of lithium phosphate and oxynitride phosphate glasses with different Li/P ratios, first with compositions $57.5Li_2O{\cdot}42.5P_2O_5$ and second prepared through a thermal treatment under ammonia atmosphere of the sample with initial composition $55Li_2O{\cdot}45P_2O_5$. A theoretical model is suggested for the description of experimental results obtained from acoustic spectra of the glasses prepared in the system $Li_{1.35}PO_{3.18}$ and $Li_{1.22}PO_{2.80}N_{0.21}$ with the purpose to study ion relaxation processes and transport mechanisms.

2. Experiment

2.1. Characterisation of the glasses

Lithium phosphate glasses with composition $xLi_2O{\cdot}(1-x)\ P_2O_5$ (x = 55, 57.5 mol%), were obtained by conventional melt-quenching technique. Stoichiometric amounts of reagent grade raw materials Li_2CO_3 (Aldrich, 99 %) and $(NH_4)_2HPO_4$ (Merck, 99 %) were weighed and mixed. The batches were calcined in porcelain crucibles held in an electric furnace up to 450 °C, and then melted in a gas furnace (propane/air) during 1 h at temperatures ranging from 800 °C to 1000 °C depending on composition. The compositions of the glasses are given by their molecular formula as $Li_{1.22}PO_{3.11}$ and $Li_{1.35}PO_{3.18}$ for Li_2O contents of 55 and 57.5 mol%, respectively [2].

Oxynitride lithium phosphate glasses were obtained through ammonolysis of the base glasses in an Al_2O_3 gas-tight tube furnace

* **Peter Hockicko[1], Francisco Munoz[2], Peter Bury[1], Peter Sidor[1]**
[1] Department of Physics, Faculty of Electrical Engineering, University of Zilina, Slovakia
[2] Insituto do Ceramica y Vidrio (CSIC), Madrid, Spain

at temperatures from 600 °C to 750 °C and treatment times of 3 h. Base glasses were placed in graphite moulds acting as individual "crucibles" of 2 cm in diameter and 5 mm deep. The furnace was heated up to the treatment temperature at a constant heating rate of 10 K min^{-1} under N_2 flow. In the present work only two glass compositions of prepared set of samples [2] are studied by acoustic spectroscopy: $Li_{1.35}PO_{3.18}$ (C) and $Li_{1.22}PO_{2.80}N_{0.21}$ (BN).

Electrical conductivity measurements were performed by Electrochemical Impedance Spectroscopy (EIS) in a Solartron SI1260 impedance analyzer, in the frequency range from 10 Hz to 10 MHz at temperatures between 40 and 200 °C [2]. The samples were cut into discs of 1–2 mm in thickness and 10 mm in diameter and gold electrodes were sputtered on both faces as contacts for electrical measurements.

2.2. Acoustic measurements

The longitudinal acoustic waves of frequency 13, 17 and 29 MHz were generated by Pulse Modulator and Receiver – MATEC 7700 and $LiNbO_3$ transducer acoustically bonded to the quartz rod buffer. Acoustic measurements were realized at the temperature range of 290 – 530 K at a heating rate of 0.5 K/min on the same samples that were used previously for electrical measurements. The quartz buffer was used to separate the acoustic signal from thin sample (Fig. 1). The samples for acoustical attenuation measurements were cylindrical in shape (thickness ≈ 1.8 mm and 8.7 mm in diameter) and end faces were polished to be flat and parallel.

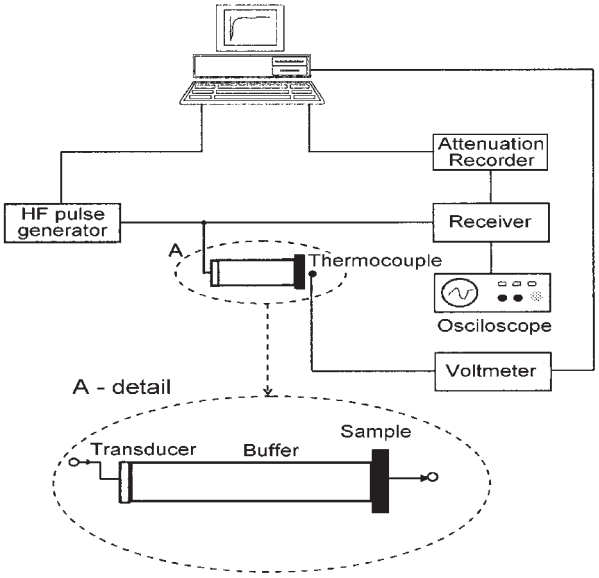

Fig. 1 Experimental arrangement for acoustic attenuation measurement

3. Theoretical principles

In a dilute system containing a low concentration of mobile ions the acoustic attenuation spectrum may be described as a Debye-like, single relaxation time process in which the individual ion hops occur independently of each other. In such cases, the attenuation α for a wave of angular frequency ω takes the form

$$\alpha = \Delta\left(\frac{\omega^2\tau}{1+\omega^2\tau^2}\right), \tag{1}$$

where the parameter Δ is the relaxation strength and it determines the magnitude of the attenuation peak [8].

The term in the equation (1) in the round brackets describes a Debye peak. The acoustic attenuation will exhibit a maximum when the condition ωτ is equal to 1 and

$$\tau = \tau_0 \exp\left(E_a/k_B T_{peak}\right) \tag{2}$$

is the most probable relaxation time, T thermodynamic temperature and k_B the Boltzmann constant [9]. The relaxation processes, described by the Arrhenius equation (2), are characterized by the activation energy E_a for jumps over the barrier between two potential minima and typical relaxation frequency of ion hopping $1/\tau_0 \approx 10^{13} - 10^{14}\ s^{-1}$.

All the glasses we studied using acoustic spectroscopy exhibit the Arrhenius – type relaxation between the temperature of the peak maximum T_{peak} and the applied frequency f of acoustic waves

$$f = f_0 \exp\left(-\frac{E_a}{k_B T_{peak}}\right), \tag{3}$$

where f_0 is the preexponential factor.

In fact all the investigated relaxation peaks are much broader than Debye peak. It can be interpreted as arising from the existence of a distribution of relaxation times due to random deviations in the local arrangement of the system.

In solid electrolytes the mobile ion concentrations are large and conduction mechanisms are thought to be cooperative. The relaxation phenomena observed in a wide variety of materials exhibit then a power-law type of frequency dependence. The relationship corresponding to the Debye behaviour is expressed in the form [8]

$$\alpha \approx \frac{1}{T}\left(\frac{(\omega\tau)^m}{1+(\omega\tau)^{1+m+n}}\right), \tag{4}$$

where m and n are power-law exponents, which take values between 0 and 1. When $m = 1$ and $n = 0$, equation (4) reduces to the equation for a single Debye-like process. One of the functions which were mainly used to fit mechanical loss data is the double power law (DPL) [10]

$$\alpha(\omega, T) \propto \frac{1}{(\omega\tau)^{-n} + (\omega\tau)^m}. \tag{5}$$

Using this function, we can fit also the acoustic attenuation spectrum of the lithium phosphate glasses. Applying the method of genetic algorithm [11] with binary representation of the theoretical attenuation DPL function of variables in connection with the visual construction of the acoustic attenuation model we analyzed then the acoustic spectra obtained on copper phosphate glasses.

4. Experimental results and discussion

The acoustic spectra are illustrated for investigated sample BN and measured at various frequencies in Fig. 2. All acoustic measurements indicate one broad attenuation peak at higher temperature, however, for some dependences we can distinguish two separated peaks.

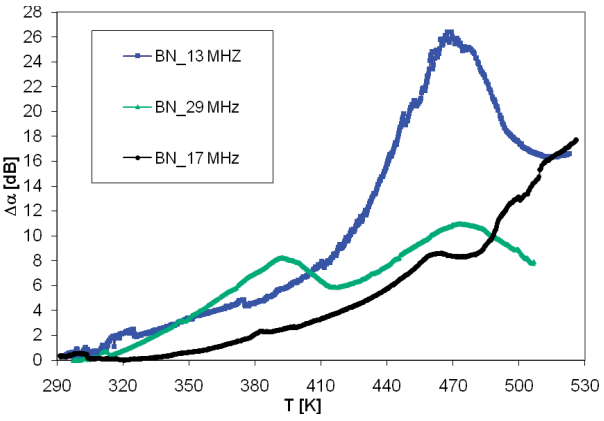

Fig. 2 Comparison of the acoustic attenuation spectra of investigated lithium phosphate glass sample $Li_{1.22}PO_{2.80}N_{0.21}$ (BN) measured at frequency f = 13, 17 and 29 MHz

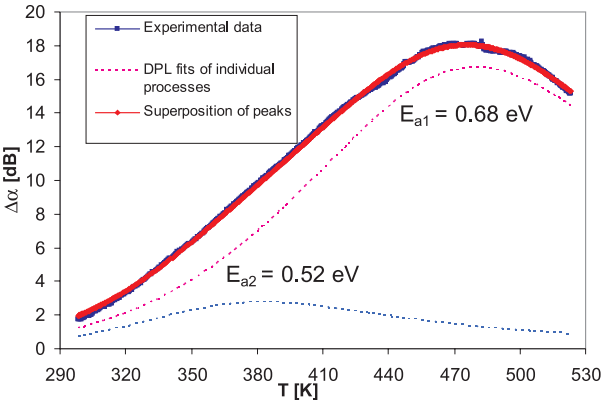

Fig. 3 The acoustic spectrum of the glass sample $Li_{1.35}PO_{3.18}$ (C) (full blue line) measured at frequency f = 13 MHz and the DPL fits of the two supposed relaxation processes (dashed line) including their superposition (full red line)

Applying DPL function (5) we simulated acoustic attenuation spectra at constant frequency as a superposition of individual peaks (Figs. 3–5) and determined the values of activation energies (Tab. 1) of the individual relaxation processes connected with ion hopping.

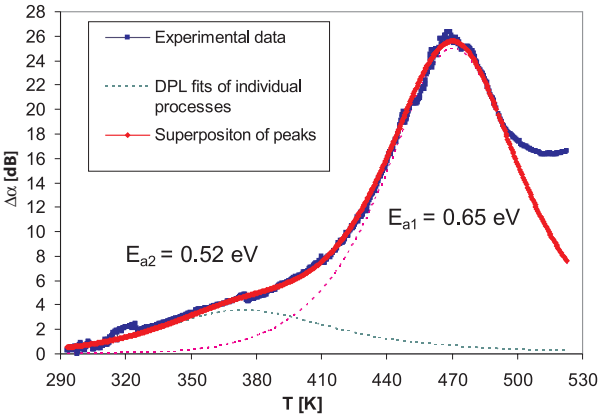

Fig. 4 The acoustic spectrum of the glass sample $Li_{1.22}PO_{2.80}N_{0.21}$ (BN) (full blue line) measured at frequency f = 13 MHz and the DPL fits of the two supposed relaxation processes (dashed line) including their superposition (full red line)

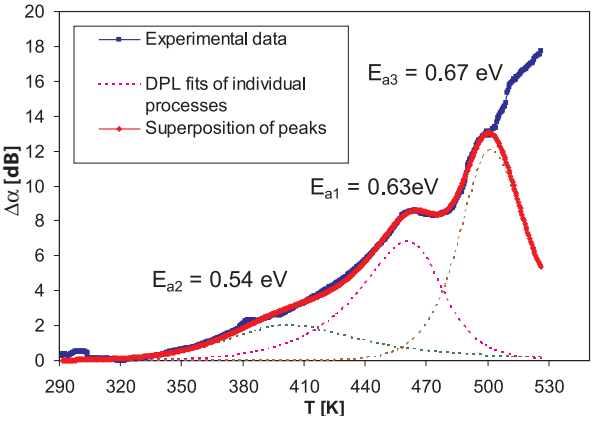

Fig. 5 The acoustic spectrum of glass sample $Li_{1.22}PO_{2.80}N_{0.21}$ (BN) (full blue line) measured at frequency f = 17 MHz and the DPL fits of the three supposed relaxation processes (dashed line) including their superposition (full red line)

Using the theoretical double power law (DPL) model we tried to fit the whole acoustic attenuation spectra of investigated samples measured at various frequencies as a superposition of two relaxation processes, respectively. The whole temperature dependence of acoustic attenuation cannot be fitted applying only one DPL function in any case. The whole temperature dependence of acoustic attenuation was analyzed then assuming the existence of at least two thermally activated relaxation processes of Li^+ ions in connection with different kinds of sites.

There are several categories of relaxation processes connected with temperature peaks of individual processes. Comparing the activation energies obtained from acoustic and electrical measurements (Tab. 1), it seems that essentially the same microscopic processes can be responsible for the electrical and one of the acoustic relaxation processes (the same or very close values of E_{a1} and E_{ae}). However, the acoustic spectra are able to detect also other processes compared with electrical spectroscopy.

Activation energies calculated from acoustic and electrical measurements — Table 1

Glass sample	Acoustic Measurements				Electrical measurements
	f [MHz]	E_{a1} [eV]	E_{a2} [eV]	E_{a3} [eV]	E_{ae} [eV]*
C ($Li_{1.35}PO_{3.18}$)	13	0.68	0.52	-	0.68
BN ($Li_{1.22}PO_{2.80}N_{0.21}$)	13	0.65	0.52	-	0.64
	17	0.63	0.54	0.67	
	29	0.63	0.52	-	

*Data were used from [2]

The results from FTIR spectra of the $LiPO_3$ glasses [1] show characteristic peaks corresponding to the different vibration modes of the PO_4 tetrahedra ($\nu(PO_4)^{3-}_{sym,asym}$) as well as those of the P–O–P bonds ($\nu(P\text{–}O\text{–}P)_{sym,asym}$ and $\delta(P\text{–}O\text{–}P)$) and the PO_2^- groups ($\nu(PO_2)^-_{sym,asym}$). Using Nuclear Magnetic Resonance it was found [12] that the oxide glass marked C (nitrogen-free) is composed of PO_4 groups of Q^2 – type (metaphosphate composition with two bridging oxygen atoms bonded to neighbouring phosphorous atoms, cyclic anions of exact $(PO_3^-)_n$) and Q^1 structural units (pyrophosphate composition with one bridging oxygen atom bonded to neighbouring phosphorous atom, $P_2O_7^{4-}$ groups). Furthermore, oxynitride glass marked BN presents other groups: PO_3N and PO_2N_2, which are results of the nitrogen/oxygen substitution [13]. The two activated processes found from modelling of acoustic spectra might be related to different structural motifs: Lithium ions bonded to non-bridging oxygen atoms present in Q^2 phosphate units or Q^1 pyrophosphate ones. Apart from that, it would be necessary to take into account that non-bridging oxygen atoms belonging to PO_3N and PO_2N_2 oxynitride tetrahedral units formed during nitridation might also contribute with additional effects, e.g. a third process.

From acoustic measurements we found lower activation energies for the sample BN in comparison with the sample C. It was found that nitrogen affected the electrical conductivity according to the structural modifications of the glass network induced by nitrogen [2]. Some authors [14] supposed that the decrease in the electrostatic energy when P–O bonds are replaced by more covalent P–N bonds may cause the decrease in the electrostatic activation energy and increase in ionic conductivity. The effect of nitrogen on conductivity can be explained by higher cross-linking density introduced by nitrogen atoms, which should facilitate the lithium transfer between phosphate chains. The higher amount of non-bridging oxygen atoms generated by nitridation could increase the number of hopping positions for Li^+ ions creating conduction paths with lower activation energy and the rising of the electrical conductivity as a consequence of this [2].

5. Conclusion

The experimental investigation of the lithium phosphate and oxynitride phosphate glasses proved that acoustical spectroscopy can be a very useful technique for the study of relaxation and transport mechanisms in ion conductive glasses. Using the theoretical model of Double Power Law function for the simulation of acoustic spectra we can better determine and describe the relaxation processes and transport mechanism of mobile ions. Several different kinds of sites responsible for ionic hopping motion were discovered and described. The comparison of activation energies obtained from acoustic and electrical measurements showed that the same microscopic processes can be responsible for the acoustic and electrical relaxation processes, however the acoustic spectroscopy can detect also some minor processes. It was found that the activation energy connected with main attenuation peak decreases with increasing content of nitrogen. Nitridation increases the amount of non-bridging oxygen atoms and cross-linking density which increases the electrical conductivity of the oxynitride phosphate glasses connected with decrease of the activation energy.

Acknowledgments

The authors would like to thank to Mr. F. Cernobila for technical assistance. The authors wish to thank for the support to the R&D operational program "Centre of excellence of power electronics systems and materials" for their components. The project is funded by the European Community, ERDF – European regional development fund.

References

[1] MOREAU, F., DURAN, A., MUNOZ, F.: *Journal of the European Ceramic Society* 29 (2009) 1895
[2] MUNOZ, F., DURAN, A., PASCUAL, L., MONTAGNE, L., REVEL B., RODRIGUES, A. C. M.: *Solid State Ionics* 179 (2008) 574
[3] YU, X., BATES, J. B., JELLISON JR., G. E., HART, F. X.: J. *Electrochem. Soc.* 144 (2) (1997) 524
[4] ROLING, B., HAPPE, A., INGRAM, M. D., FUNKE, K.: *J. Phys. Chem.* B 103 (1999) 4122

[5] CHARNAZA, E. V., BORISOV, B. F., KULESHOV, A. A.: *Proc. World Congress on Ultrasonics,* Berlin (1995) 483
[6] FUNKE, K.: *Sol. State Ionics* 94 (1997) 27
[7] BURY, P., HOCKICKO, P., JURECKA, S., JAMNICKY, M.: *Physica Status Solidi* (c) 11 (2004) 2888
[8] ALMOND, D. P., WEST, A. R.: *Solid State Ionics* 26 (1988) 265
[9] CARINI, G., CUTRONI, M., FEDERICO, M., GALLI, G., TTIPODO, G.: *Physical Review* B 30 (1984) 7219
[10] BURY, P., HOCKICKO, P., JAMNICKY, M.: *Advanced Materials Research* 39-40 (2008) 111
[11] JURECKA, S., JURECKOVA, M., MULLEROVA, J.: *Acta Physica Slovaca* 53 (2003) 215
[12] BROW, R. K.: *J. Non-Cryst. Solids* 263&264 (2000) 1
[13] MUNOZ, F., PASCUAL, L., DURAN, A., MONTAGNE, L., PALAVIT, G., BERJOAN, R., MARCHAND, R.: *J. Non-Cryst. Solids* 324 (2003) 142
[14] WANG, B., KWAK, B. S., SALES, B. C., BATES, J. B.: *J. Non-Cryst. Solids* 183 (1995), 297.

Mikulas Gintner – Josef Juran – Ivan Melo – Beata Trpisova *

THE EFFECTIVE DESCRIPTION OF STRONG ELECTROWEAK SYMMETRY BREAKING

The actual mechanism of electroweak symmetry breaking remains the last unsolved part of the Standard model of electroweak interactions. We review the general requirements that all possible solutions must fulfill. Based on them the effective description of the mechanism can be formulated. We offer such a description which is a modified version of the so-called BESS model and discuss its properties.

Keywords: electroweak symmetry breaking, effective Lagrangian, BESS model.

1. Introduction

The gauge invariance as a fundamental principle for building the electroweak Lagrangian enables describing the electromagnetic and weak interactions under the same formalism [1]. The theory is commonly known as *the Standard model of electroweak interactions* (SM) [2]. The SM leads to the long list of predictions that have been successfully verified by experiments.

However, the local symmetry does not tolerate explicit mass terms for gauge fields. This seems to be in contradiction with reality in all cases but the photon. Fortunately, there is a way to reconcile the massive gauge bosons, namely Z, W^+, W^-, and gauge invariance: spontaneous breaking of electroweak symmetry accompanied by *the Higgs mechanism*. The Higgs mechanism was first suggested to explain some collective density fluctuations in plasma which were produced by a finite range electromagnetic field (a massive photon) [3]. Later it was generalized as a relativistic field theory [4] and its renormalizability was proved [5].

Despite the great success of the SM one essential component of the theory remains a puzzle: it is the actual mechanism behind the electroweak symmetry breaking (ESB). The introduction of the Higgs complex doublet scalar field of a non-zero vacuum expectation value to the electroweak Lagrangian serves as a benchmark hypothesis. A direct consequence of this hypothesis is the presence of the Higgs boson in the particle spectrum of the SM, not observed to these days. It is not the only plausible hypothesis though.

There is a host of candidates for the suitable extensions of the SM. They range from supersymmetric theories with multiple elementary Higgs bosons in their spectra to the theories of new strong interactions, like Technicolor, which might form bound states of new elementary particles in analogy with QCD. These bound states might appear in the particle spectrum as new resonances.

In more recent theories like the Little Higgs models and the Gauge-Higgs unification models, their dual-description relation to the Heavy Composite Higgs and the No Higgs strongly-interacting models has been demonstrated (see [6] and references therein). Most of these models introduce new particles at about 1 TeV.

Facing this plethora of alternative theories it is highly desirable to describe their low-energy phenomenology in a unified way. Thus, it is very useful to exploit the formalism of effective Lagrangians. Therein the so-called *hidden local symmetry* (HLS) approach [7] can be used to introduce new vector resonances which might originate in some new physics beyond the SM. The new particles are not only a byproduct of a particular ESB mechanism but they would be needed to tame the unitarity if the Higgs boson were not found. The HLS formalism along with the AdS/CFT correspondence plus deconstruction is also behind the dual-description relation of the recent models mentioned above [6].

In this paper we present the modified version of the existing effective model of strong ESB. The original model is called the *BESS* (Breaking Electroweak Symmetry Strongly) model [8]. There – beside the known SM particles – a new $SU(2)_V$ vector boson triplet is introduced exploiting HLS. The new triplet is supposed to represent the spin-1 bound states of hypothetical new strong interactions. We take this model and modify its interactions of the vector triplet with fermions. In the BESS model there is a universal direct coupling of the triplet to all fermions of a given chirality. In our model, on the other hand, we admit direct couplings of the new triplet to top and bottom quarks only. The modification reflects speculations about a special role of the top quark

* **Mikulas Gintner[1], Josef Juran[2], Ivan Melo[1], Beata Trpisova[1]**
[1] Physics Department, University of Zilina, Slovakia, E-mail: gintner@fyzika.uniza.sk
[2] Institute of Experimental and Applied Physics, Czech Technical University in Prague, Czech Republic

(or the third quark generation) in the mechanism of ESB. We named the modified BESS model as the *top-BESS* model.

In Section 2 of the paper we discuss the general requirements for the ESB mechanism which must be reflected by any ESB hypothesis. In Subsection 2.2 we briefly introduce the BESS and the top-BESS models. Besides we show the direct interaction vertices of the new vector triplet to top and bottom quarks and the differences in the couplings of the electroweak gauge bosons with these quarks. Section 3 is devoted to the phenomenology of the top-BESS model. Herein we discuss the masses and the decay widths of the new vector triplet. We also point to the forward-backward asymmetry as a promising observable for measuring parameters of the V–to–t/b couplings. Conclusions can be found in Section 4.

2 The effective description of ESB

2.1. General requirements

The central idea to the generating masses of the electroweak gauge bosons $W^{\pm}$ and Z is the *spontaneous symmetry breaking* (SSB): $G \to H$ where G is a global continuous symmetry of the Lagrangian and H is a continuous symmetry of its vacuum (ground state), $H \subseteq G$. The *Goldstone theorem* [9] implies that the SSB results in appearance of massless scalar fields, the so-called *Nambu-Goldstone bosons* (NGB). The number of NGB is equal to dim G – dim H, i.e. the number of "broken" generators of the group G. However, once $F \subset G$ is made local by introducing gauge fields interacting with the NGB's the corresponding NGB's disappear from the spectrum while the G – H gauge fields become massive and acquire longitudinal degrees of freedom. This is depicted in the following figure:

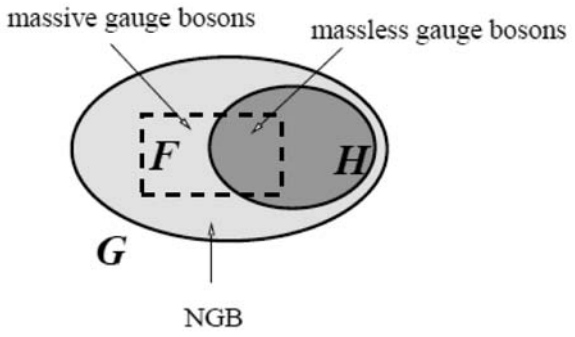

Now we formulate the conditions that must be fulfilled in order to build the most general effective Lagrangian describing the Higgs mechanism that provides masses for the Z^0 and $W^{\pm}$ gauge bosons [10]:

- A part of the SM must exhibit the SSB pattern $G \to H$, where G is a global symmetry and H is its subgroup. Since we need masses for three gauge bosons we require that there would be at least 3 broken generators: dim $K \geq 3$ where $K = G/H$ (dim K = dim G − dim H).
- Three of broken generators must generate a local symmetry. The massive gauge bosons must be coupled to the corresponding three NGB's.
- The gauge group $SU(2)_L \times U(1)_Y$ has to be contained in G. The photon is a massless gauge boson thus $U(1)_{em} \subset H$. Therefore dim $G \geq 4$, dim $H \geq 1$.
- If the SSB bears the responsibility for the masses of gauge bosons then the masses should be given by the scale υ of the SSB, $M_{W,Z} = \mathcal{O}(\upsilon)$. The value of υ can be obtained from the Fermi constant G_F which is measured in the muon decay:

$$\upsilon^2 = \frac{1}{\sqrt{2}\,G_F}, \quad G_F \approx 1.17 \times 10^{-5}\,\mathrm{GeV}^{-2}$$
$$\Longrightarrow \upsilon \approx 246\,\mathrm{GeV}$$

- The electrowek gauge symmetry predicts that the relative strength of the charged weak currents to the neutral weak currents

$$\rho = \frac{\text{charged current}}{\text{neutral current}} = \frac{M_W^2}{M_Z^2 \cos\theta_W}$$

is equal to 1 at tree level. Generally, at loop levels the gauge symmetry $SU(2)_L \times U(1)_Y$ admits large corrections to ρ. Nevertheless, when the H group contains the so-called *custodial symmetry* $SU(2)_V$ the radiative corrections to the ρ parameter must be small. When measured in experiments the ρ parameter comes up with the value

$$\rho_{\mathrm{exp}} = 1 + \mathcal{O}(10^{-2})$$

which supports the presence of the custodial symmetry. The condition $SU(2)_V \subset H$ implies dim $H \geq 3$.

If we consider $K = 3$ (otherwise we would have to explain where the uneaten NGB's are) the constraints listed above lead to a unique choice of the groups G and H:

$$G = SU(2)_L \times SU(2)_R,$$
$$H = SU(2)_V,\ K = SU(2)_A,$$

where $SU(2)_V$ is a diagonal subgroup of $SU(2)_L \times SU(2)_R$ and $SU(2)_A$ is its axial[1)] "subgroup". This also implies that NGB's are pseudoscalar particles.

Let us mention that the gauge invariance under a chiral symmetry group excludes explicit mass terms for fermions. However, gauge invariant mass terms for fermions can be generated through the ESB mechanism.

[1)] $SU(2)_A$ is not a group even though it is often called that way in the physical literature.

2.2 From BESS to top-BESS

The BESS model [8] effectively describes a Higgsless ESB mechanism accompanied by a hypothetical strong triplet of vector resonances $\tilde{V}^{\alpha}_{\mu}$. In the HLS formulation the symmetry of the model is $[SU(2)_L \times SU(2)_R \times U(1)_{B-L}]^{glob} \times SU(2)^{loc}_V$ where B, L are the baryon and lepton numbers, respectively. The hypothetical vector triplet is introduced as the $SU(2)_V$ gauge bosons. Beside the indirect interactions of the new vector resonances to the SM fermions induced by the mixing of $\tilde{V}^{\alpha}_{\mu}$ with the SM gauge bosons, the BESS model couples the vector resonances directly and universally to all SM fermion generations of a given chirality. The direct interactions are parameterized by two free parameters, b for the left fermions, and b' for the right fermions. The low energy measurements imply the following limits: $b \lesssim 0.01$, $b' \approx 0$.

In the top-BESS model we modify the fermion sector by considering no direct interactions of V to fermions other than t and b. The $SU(2)_L$ symmetry does not allow us to disentangle the V-to-t_L coupling from the V-to-b_L one. However, it can be done in the case of right fermions. We do it and to simplify the numerical analysis of the model we turn off the direct interaction of V to b_R completely. The full form of the top-BESS Lagrangian can be found in [11]. Here, we show only the part responsible for the direct interactions of t and b quarks to the new vector resonances parameterized by the $b_{1,2}$ coupling constants as well as the non-SM interactions of t and b with the SM gauge bosons

$$
\begin{aligned}
L_{\rho}^{(t,b)_L} &= \frac{b_1}{1+b_1} g \bar{\psi}_L \tilde{W}^a \tau_a \psi_L + \frac{b_1}{1+b_1} \frac{g''}{2} \bar{\psi}_L \tilde{V}^a \tau_a \psi_L \\
&= \frac{1}{2} \frac{b_1 g}{1+b_1} \left(\bar{t}_L \tilde{W}^3 t_L - \bar{b}_L \tilde{W}^3 b_L \right) + \frac{1}{\sqrt{2}} \frac{b_1 g}{1+b_1} \left(\bar{t}_L \tilde{W}^+ b_L - \bar{b}_L \tilde{W}^- t_L \right) \\
&= \frac{1}{2} \frac{b_1}{1+b_1} \frac{g''}{2} \left(\bar{t}_L \tilde{V}^3 t_L - \bar{b}_L \tilde{V}^3 b_L \right) + \frac{1}{2} \frac{b_1}{1+b_1} \frac{g''}{2} \left(\bar{t}_L \tilde{V}^+ b_L - \bar{b}_L \tilde{V}^- t_L \right)
\end{aligned} \tag{1}
$$

$$
\begin{aligned}
L_{\rho}^{(t,b)_R} &= \frac{b_2}{1+b_2} g' \left(\bar{\psi}_R P_0 \right) \not{B} \tau_3 \left(P_0 \psi_R \right) + \frac{b_2}{1+b_2} \frac{g''}{\sqrt{2}} \left(\bar{\psi}_R P_0 \right) \tilde{V}^3 \tau_3 \left(P_0 \psi_R \right) \\
&= \frac{1}{2} \frac{b_2 g}{1+b_2} \left(\bar{t}_R \not{B} t_R \right) + \frac{1}{2} \frac{b_2}{1+b_2} \frac{g''}{\sqrt{2}} \left(\bar{t}_R \tilde{V}^3 t_R \right)
\end{aligned} \tag{2}
$$

where $\psi = (t, b)^T$, and $P_0 = \mathrm{diag}(1, 0)$. The gauge couplings g, g' and g'' correspond to the $SU(2)_L$, $U(1)_Y$, and $SU(2)_V$ gauge symmetry groups of the model, respectively. As a consequence of turning off the V-to-b_R coupling in (2) neither t_R couples directly to the charged V-resonance.

The Lagrangians (1) and (2) are expressed in terms of gauge field flavor eigenstates. However, in experiments we measure the mass eigenstates. The relations between the two sets of the gauge field eigenstates are given by

$$
\begin{pmatrix} \tilde{W}^{\pm} \\ \tilde{V}^{\pm} \end{pmatrix} = \left[\begin{pmatrix} 1 & -\sqrt{\alpha}\, x \\ \sqrt{\alpha}\, x & 1 \end{pmatrix} + \mathbb{O}(x^2) \right] \begin{pmatrix} W^{\pm} \\ V^{\pm} \end{pmatrix},
$$

$$
x = \frac{\overline{M}_W}{\overline{M}_V} = \frac{1}{\sqrt{\alpha}} \frac{g}{g''}
$$

where $G = \sqrt{g^2 + g'^2}$, $c_W = \overline{M}_V / \overline{M}_Z$, $s_W = \sqrt{1 - c_W^2}$, $c_{2W} = c_W^2 - s_W^2$, $s_{2W} = 2 s_W c_W$, $\overline{M}_V = gv/2$, $\overline{M}_Z = Gv/2$. The free parameter α is related to the mass of the vector triplet, degenerated in the leading order approximation: $\overline{M}_V = \sqrt{\alpha}\, g'' v/2$. $\overline{M}_W$ and $\overline{M}_Z$ are the W and Z boson masses in the leading order approximation, respectively.

The measurement of $Zb\bar{b}$ vertex constrains the V-to-t_L coupling to relatively small values. Due to the disentangling of the t_R interactions with V from the b_R interactions with V the measurement does not limit the V-to-t_R interaction. For the low-energy limits on the model's parameters, see [11, 12].

3. Phenomenology of the top-BESS model

3.1. Masses and widths of the new vector resonance triplet

The masses of the $SU(2)_V$ neutral and charged resonances depend on the parameters α and g'' as shown in Fig. 1. In all calculations depicted here and below we consider the fixed values of the Z and W masses as taken from experiment. To compensate for the non-SM corrections to M_Z and M_W the SM parameters v, g, and g' vary slightly with g''.

The vector resonances decay dominantly to the SM gauge bosons and/or to the third generation of quarks. In Fig. 2 we show the total decay widths of the vector resonances [13]. The plots of the partial decay widths are shown in Fig. 3. Finally, we compare the BESS and the top-BESS models in terms of the total decay

$$
\begin{pmatrix} \tilde{W}^3 \\ \not{B} \\ \tilde{V}^3 \end{pmatrix} = \left[\begin{pmatrix} s_W & c_W & -c_W \sqrt{\alpha}\, y \\ c_W & -s_W & -s_W \sqrt{\alpha}\, y \\ s_{2W} \sqrt{\alpha}\, y & c_{2W} \sqrt{\alpha}\, y & 1 \end{pmatrix} \right] + \mathbb{O}(y^2) \begin{pmatrix} A \\ Z \\ V^0 \end{pmatrix}, \quad y = \frac{\overline{M}_Z}{\overline{M}_V} = \frac{1}{\sqrt{\alpha}} \frac{G}{g''}
$$

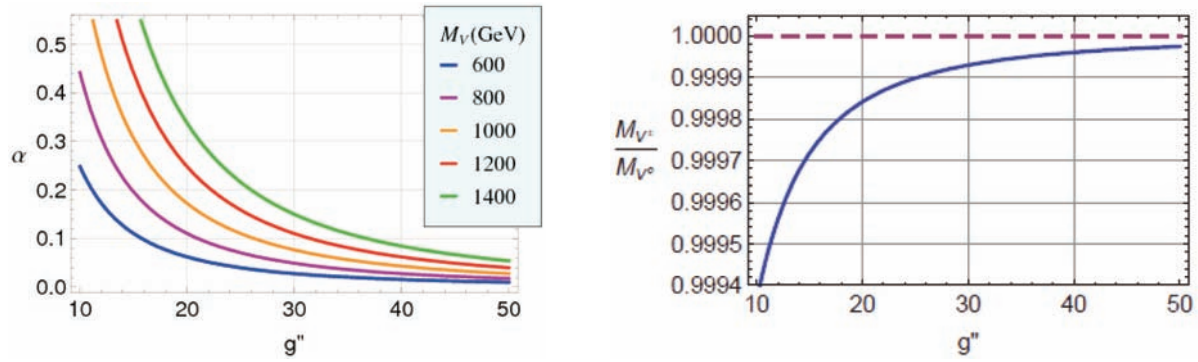

Fig. 1 At the left: The relations between α and the $SU(2)_V$ gauge coupling g″ at various fixed masses of V. At the right: The splitting of the $M_{V^\pm}$-to-M_{V^0} degeneracy as a function of g″.

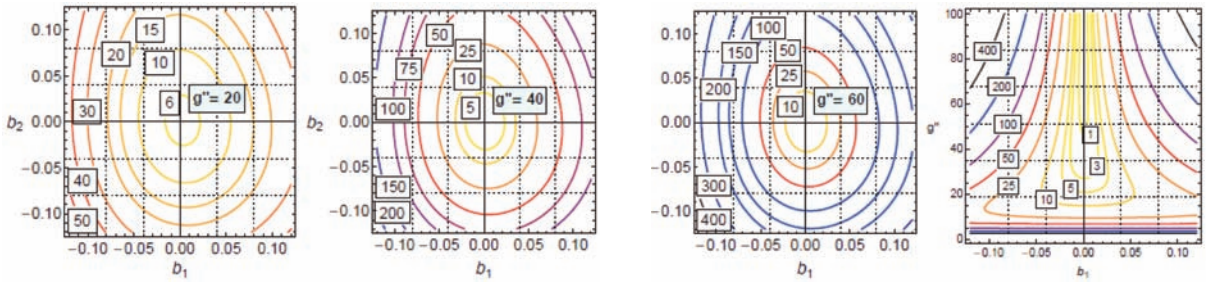

Fig. 2 The top-BESS total decay width contours of V^0 in the (b_1, b_2) parametric space at various values of g″, and of $V^\pm$ in the (b_1, g″) parametric space. The contour labels are in GeV.

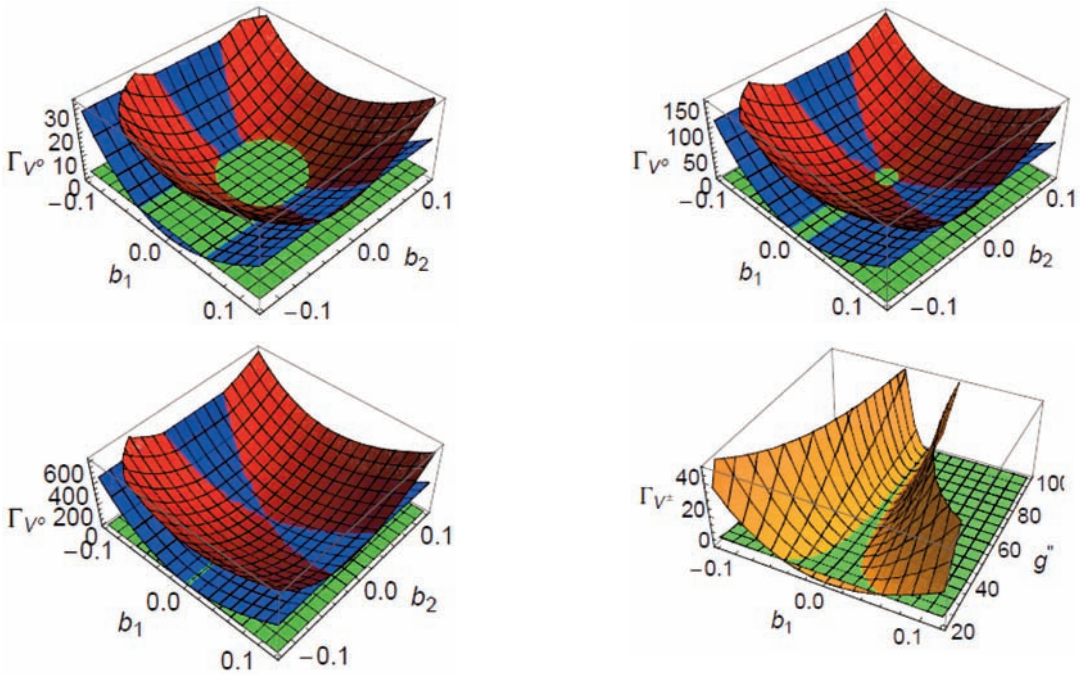

Fig. 3 The top-BESS partial decay widths of V^0 as functions of b_1 and b_2 at g″ = 25, 50, 100, from the left to the right, respectively, and of V^+ as functions of b_1 and g″. For the neutral resonance, the green, blue, red surface corresponds to the W^+W^-, $b\bar{b}$, and $t\bar{t}$ channel, respectively. For charged resonance the green, orange surface corresponds to the W^+Z and $t\bar{b}$ channel, respectively.

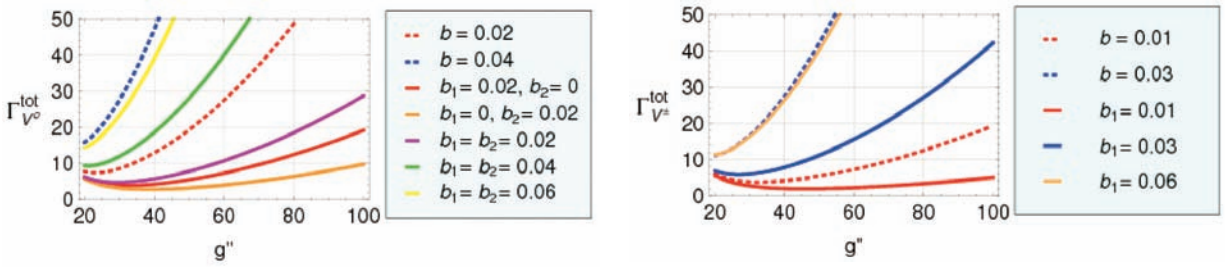

Fig. 4 Differences between the BESS model (dotted lines) and the top-BESS model (solid lines) demonstrated through the total decay widths of V^0 and $V^\pm$ (in GeV).

widths of V^0 and $V^\pm$ in Fig. 4 [13]. In all cases we assume $M_{V^0} = 1$ TeV.

3.2. Experimental signatures

It would seem natural to search for the signs of the new resonances in the processes where the electroweak gauge bosons and/or the *t* and *b* quarks are involved. At the Large Hadron Collider (LHC) this is often a difficult case due to the large backgrounds to the processes with *b* and *t* in the final state and/or due to the negligible *b* and *t* luminosities in *pp* collisions.

In the BESS model the new $SU(2)_V$ vector bosons mix with the electroweak gauge bosons. While the mixing complicates theoretical analysis of the model it might provide some advantages in experimental searches. The mixing generates interactions of the new resonances with the fermions of lighter generations. Although these interactions are suppressed by the mixing factors, the LHC processes enabled by them have the advantage of higher parton luminosities and more favorable final state topologies. In [12] we have calculated sensitivities of the $pp \to t\bar{t}X$, $b\bar{b}X$, $t\bar{b}X$, W^+W^-X, $W^\pm ZX$ processes with subsequent decays to leptons and hadronic jets at the LHC without considering backgrounds. At this level of analysis the investigated processes have displayed promising potential to serve as probes of new physics under consideration. Nevertheless, further and more detailed investigation of the issues is necessary.

New ESB-responsible physics can also be studied at a future e^+e^- collider under preparation which is known under its generic name of ILC (International Linear Collider). While the LHC will serve as a discovery machine the ILC will provide much cleaner signal to measure parameters of new physics. In [14] we have analyzed three ILC processes – $e^+e^- \to t\bar{t}$, $e^+e^- \to b\bar{b}$, and $e^+e^- \to W^+W^-$ – at the collision energies 800–1200 GeV as probes of the top-BESS model with $M_{V^0} = 1$ TeV.

The above mentioned investigations focused on discovering and distinguishing mass peaks of the *V*-resonances in the invariant mass distributions of the *V* decay products. The observation of a mass peak would result in determining the mass and, perhaps, the width of the observed resonance. However, here we would like to point to yet another ILC observables which might be suitable for determining the values of b_1 and b_2 parameters. Namely, they are the forward-backward assymmetries of top and bottom quarks. This is illustrated in Figs. 5 and 6 for processes $e^+e^- \to t\bar{t}$ and $e^+e^- \to b\bar{b}$, respectively, with $M_{V^0} = 1$ TeV. The curves for the forward-backward asymmetries depend significantly on the values

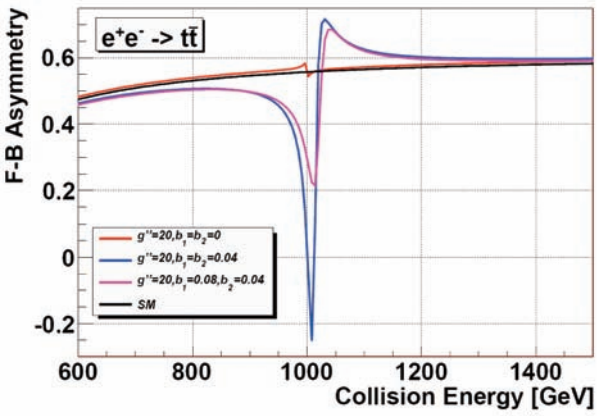

Fig. 5 The forward-backward asymmetry for the process $e^+e^- \to t\bar{t}$ as a function of the collision energy when $M_{V^0} = 1$ TeV. The sensitivity of the SM curve to the Higgs mass is negligible.

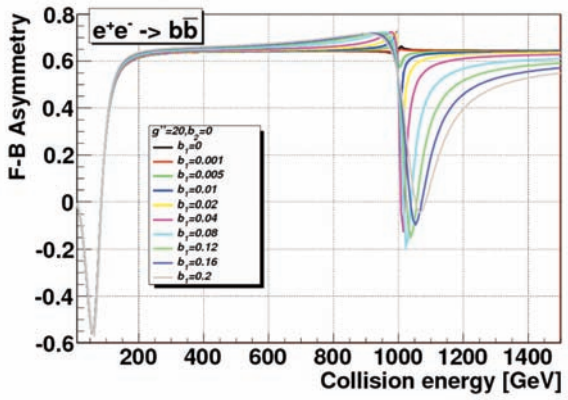

Fig. 6 The forward-backward asymmetry for the process $e^+e^- \to b\bar{b}$ as a function of the collision energy when $M_{V^0} = 1$ TeV. While $b_2 = 0$ the b_1 parameter runs through 0 to 0.2.

of the $b_{1,2}$ parameters. They also differ significanly from the SM curve in the region around the mass of the V resonance.

Regarding hadron colliders the forward-backward asymmetry is not applicable at the LHC because the symmetry of the colliding proton beams wipes up the forward-backward asymmetry. On the other hand, the Tevatron collider is free of this problem because it collides protons with antiprotons. However, its collision energy is probably too low to probe 1 TeV resonances.

4. Conclusions

In this paper we have presented the status of our ongoing study of the top-BESS model which is a well-motivated modification of the original BESS model. We had introduced the modifications to obtain the effective description of a certain class of theories which aim at explaining the mechanism of ESB. These are the theories with the top quark playing a special role in the ESB mechanism.

It appears that the properties of the theories representable by the top-BESS model can be studied at both the LHC as well as ILC colliders. While the $SU(2)_V$ resonance triplet can be discovered at the LHC by observing the invariant mass distributions of its decay products the detailed properties of the resonances can be studied at the ILC. For example, the observation of the forward-backward asymmetry at the ILC is well suited for the measurement of the $b_{1,2}$ parameters. Nevertheless, further investigation of the related issues is needed. This work is in progress.

References

[1] YANG, C. N., MILLS, R. L.: *Phys. Rev.* 96, 1954, 191.

[2] GLASHOW, S. L.: *Nucl. Phys.* 22, 1961, 579; SALAM, A., WARD, J. C.: *Phys. Lett*. 13, 1964, 168; WEINBERG, S.: *Phys. Rev. Lett.* 19, 1967, 1264.

[3] ANDERSON, P. W.: *Phys. Rev.* 130, 1963, 439.

[4] ENGLERT, F., BROUT, R.: *Phys. Rev. Lett.* 13, 1964, 321; HIGGS, P. W.: *Phys. Rev. Lett.* 12, 1964, 132; *Phys. Rev. Lett.* 13, 1964, 508; *Phys. Rev.* 145, 1966, 145.

[5] HOOFT, G.: *Nucl. Phys.* B35, 1971, 167.

[6] CHENG, H-C.: *Proceedings of 15th International Conference on Supersymmetry and the Unification of Fundamental Interactions (SUSY07), Karlsruhe, 2007*, hep-ph/0710.3407.

[7] BANDO, M., KUGO, T., YAMAWAKI, K.: *Phys. Rep.* 164, 1988, 217.

[8] CASALBUONI, R., de CURTIS, S., DOMINICI, D., GATO, R.: *Phys. Lett.* B155, 1985, 95; CASALBUONI, R., de CURTIS, S., DOMINICI, D., GATO, R.: *Nucl. Phys*. B282, 1987, 235; CASALBUONI, R., CHIAPPETTA, P., de CURTIS, S., FERUGLIO, F., GATTO, R., MELE, B., TERRON, J.: *Phys. Lett.* B249, 1990, 130.

[9] GOLDSTONE, J.: *Nuovo Cimento* 19, 1961, 154; GOLDSTONE, J., SALAM, A., WEINBERG, S.: *Phys. Rev.* 127, 1962, 965.

[10] DOBADO, A., GOMEZ-NICOLA, A., MAROTO, A. L., PELAEZ, J. R.: *Effective Lagrangians for the Standard Model,* Springer 1997, ISBN 3-540-62570-4.

[11] GINTNER, M., MELO, I., TRPISOVA., B.: *Acta Phys. Slov.* 56, 2006, 473-483.

[12] GINTNER, M., MELO, I., TRPISOVA., B.: *Proceedings of 16th Conference of Czech and Slovak Physicists, Hradec Kralove, 2007;* Proceedings of *10th Small Triangle Meeting on Theoretical Physics, Medzilaborce, 2008,* arXiv:0903.1981.

[13] GINTNER, M., JURAN, J., MELO, I.: *The proceedings of The 2009 Europhysics Conference on High Energy Physics, July 16-22, 2009*, Krakow, Poland.

[14] GINTNER, M., JURAN, J., MELO, I., TRPISOVA., B.: *Proceedings of 17th Conference of Slovak Physicists,* Bratislava, 2009.

Miroslav Gutten – Jozef Kudelcik *

METHODS OF HUMIDITYANALYSIS IN TRANSFORMER OIL

To prevent failure states of transformer, we performed different types of measurements. We made measurements of a frequency dependence of capacity of test transformer immersed in tank with transformer oil. The capacity illustrates a momentary state of the measured equipment and its variations to indicate the changes in the transformer oil. Water content in the transformer oil causes deterioration of its insulation and, finally, thermal defect of solid insulation.

Keywords: humidity, transformer, insulation resistance, dissipation factor

1. Introduction

The state of new insulation in operation mostly deteriorates due to surface contamination of insulators and insulation, their moistening and ageing. If no measures are taken in time so as to avoid this degradation, the situation usually results in damage of insulator and consequently in stop of an electrical device. Insulation state of important electrical devices, such as transmission transformer which bring huge economic cost due to each stop in operation, needs to be checked regularly [1,2].

Water content in the transformer oil causes deterioration of its insulation and thermal defect of solid insulation. Dielectric warming can be so high that the temperature increase is out of control and transformer becomes dangerous for its surrounding.

2. Analysis of humidity by measuring insulation resistance

The oldest and the easiest method of inspecting the state of insulators is by means of an insulation resistance measurement. The main disadvantage of this method is that the insulation resistance does not only depend on the state of insulation but also on its type and dimensions. Therefore, the insulation resistance method can be used to evaluate the state of insulation of an electric device only on the basis of previous experience with the same insulation on a similar device. Moreover, this method enables to identify even small insulation degradation, if it passes through an insulation layer e.g. oil – paper, but it cannot identify whether the degradation is on the side of oil or paper, which is its next drawback.

The time development of resistance can be measured (Fig.1) by the MEGGER MIT510 insulation tester, which provides direct reading of the insulation resistance in ohms regardless of the test DC voltage selected. Resistance of insulation is calculated applying Ohm's Law by measuring the resultant current at the given DC voltage. Unfortunately, more than one current flows, which tends to complicate matters. The main components of resultant current are the capacitance charging current, the absorption (or polarization) current and the conduction or leakage current. The capacitive current is initially large, but goes to zero as the test piece is charged. The absorption current is caused by charges in the insulation material moving under the effect of the electric field absorption (polarization). Conduction current is stabilized after few seconds of application of test voltage while absorption current is decreased with time. The conduction current is greatly affected by humidity or contamination in the insulation.

Utilizing this knowledge for evaluation of insulation state does not require determining full time dependence of the resistance

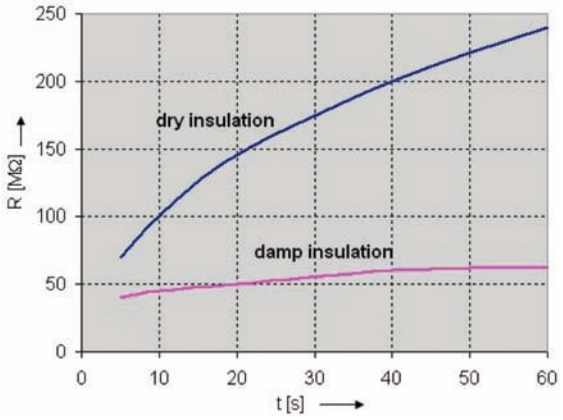

Fig. 1 Typical time dependence of the insulation resistance

* **Miroslav Gutten[1], Jozef Kudelcik[2]**
[1] Department of Measurements and Applied Electrical Engineering, University of Zilina, Slovakia, E-mail: gutten@fel.uniza.sk
[2] Department of Physics, University of Zilina, Slovakia

(current). It is enough to determine a value of the resistance (current) in two different moments from the time of connection to test DC voltage. The ratio of these two values defines the state of insulation and is called the polarization index. The polarization index is positive number (a non-dimensional parameter) and it does not depend on dimension of insulation. In the USA it is defined as the one-minute reading divided into ten-minute reading to provide a ratio, in the EU the times are 15 and 60 seconds.

To better illustrate the change in values of polarization index, it needs to be expressed by both types of currents – absorption i_a and conduction i_c.

$$p_i = \frac{R_{60}}{R_{15}} = \frac{i_{a15} + i_c}{i_{a60} + i_c} \quad (1)$$

Contaminated and humidity insulation is mainly determined by i_c, therefore numerator and denominator in eq. (1) are very close values and their ration tends to 1. On the other hand, dry and clean insulation, which is in good condition, has a very low conduction current and the time dependence on the absorption current i_a is dominant. Thus, the fraction value is noticeably higher than 1. Values above 2 indicate that the insulation conditions are all right.

The next advancement of the measurement of polarization index against isolation resistance is the great advantage of its being independent on temperature. So we don't need temperature stabilization during the whole measurement. Of course, the temperature cannot be changed during a single measurement.

3. Humidity analysis by the measurement of dissipation factor and capacity

The measurements of a dissipation factor tg(δ) and capacities of transformer windings are used for additional determination of the insulation quality as a whole or only of some parts of the transformer. The value of the dissipation factor indicates the presence of polar and ion compounds in oil and it also determines the ageing of oil. The degree of oil humidity (water content in oil) can be measured by temperature dependence of the dissipation factor [3].

The next method for determination of the degree of oil humidity (to 10 kHz – Fig. 2) is a frequency dependence on the capacity of a transformer. In damp isolation, the absorption current is negligible to leakage current, which is independent on frequency. The stage of insulation can be determined as the ratio of capacities at two different frequencies. Frequencies of 2 and 50 Hz are used in the case of a class A transformer. The values of the ratio: C_2/C_{50} before dehydration are in the range between 1.3 and 2.3 and after dehydration are around 1.2.

The next method of the determination of oil humidity was the measurement of the value of capacity at various temperatures. The capacity is the function of the absorption processes, which are characterized by their time constants and distribution of absorption charges. This method is a basis for the determination of the ratio: $(C_{75}-C_{20})/C_{80}$, where C_{20} and C_{75} (or C_{80}) are capacities at 20 and 75 °C (or 80 °C). This method was in practice substituted by the previous method (C_2/C_{50}) due to problems with defined temperature of transformers.

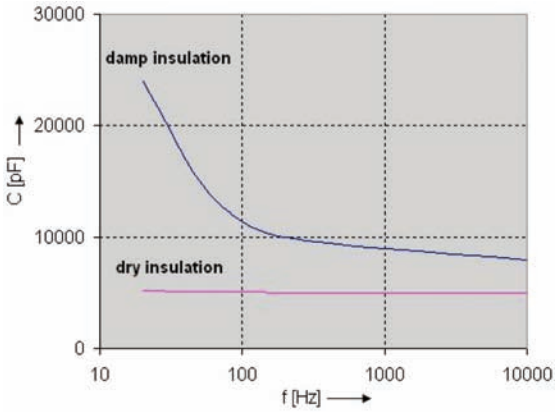

Fig. 2 The frequency change in capacities of dry and damp insulation

4. Description of experimental measurements

The test transformer (60 VA, 220/52 V) immersed in a tank with transformer oil ITO 100 is provided as an example of safety and reliability inspection of the transformer based on insulation humidity (Fig. 3). We changed water content in the transformer oil and temperature of this transformer oil. We measured capacities as functions of the oil temperature, the applied frequency (to 10 kHz) and the oil humidity. The automatic measurements of capacities were made using RLC meter and computer program. All the measured values were plotted using Excel. The results were compared with the value of the insulation resistance.

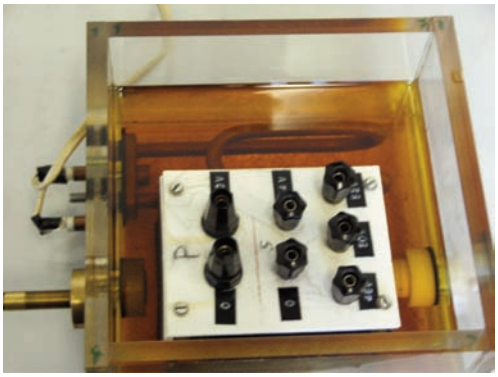

Fig. 3 Test transformer (60 VA, 220/52 V) immersed in tank with transformer oil with heating apparatus

The automatic RLC meter was used to measure the dependence of capacity on frequency. The component measurement is based on the current and voltage technique [4, 5]. Duration of

each measurement cycle was approximately 0.5 seconds. AC measurements for one frequency consist of seven single measurements, during which the following values were measured: V_p, V_q, I_p and I_q. The measured values are displayed on a phase diagram (Fig. 4) and the phase relation between I and V happens to be a load inductance. The microprocessor uses the measured values to calculate the equivalent series resistance R_s, the equivalent series reactance X_s (2) and the quality factor $Q = X_s/R_s$ of the measured component. From previous values it determined – using equations [4] – the dominant parameters (resistance, capacitance, or inductance) of the measured transformer and displays it together with the equivalent circuit symbol.

The series resistance and reactance are calculated from these components

$$R_s = \frac{V_p I_p + V_q I_q}{I_p^2 + I_q^2} \qquad X_s = \frac{V_q I_p + V_p I_q}{I_p^2 + I_q^2} \tag{2}$$

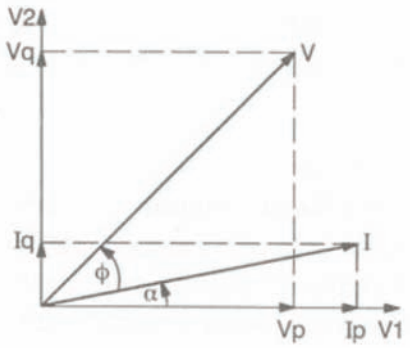

Fig. 4 Phase diagram of measured values

5. Results of the measurements

The state of insulation was measured for moisture content of 0 %, 0.05 %, 0.15 % and 0.25 % in transformer oil (Fig. 5, [6]). At moisture content 0.05 %, we already experienced a significant change in waveform upwards (increase in humidity – Fig. 5). The aim of this experiment was to verify the relation between the increase of oil humidity and capacity-frequency characteristics (see Fig. 2). Based on the measurements, we proved correctness, reliability and high sensitivity of the method for determining humidity in the transformer.

In the second step of measurements, we measured frequency dependence of capacity for various oil temperature (see Fig. 6). The measurements were made at these temperatures of the transformer oil: 25, 35, 45, 55, 65 and 75 °C. The experimental measured values verified the connection between the increase of temperature and the change of frequency development of capacity (see Fig. 6). From the measurements also follows that the capacity is the function of the absorption processes and charges, which are characterized by their time constants dependent on temperature of the system.

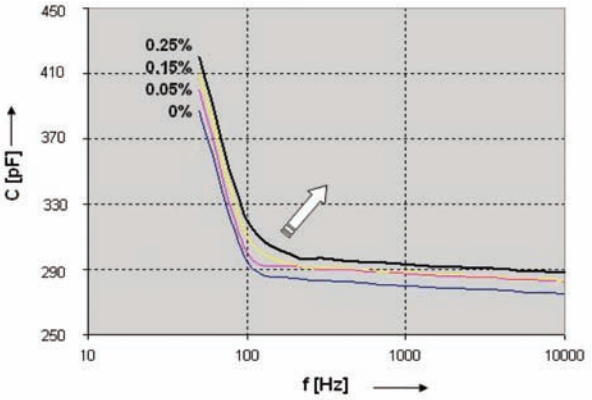

Fig. 5 The frequency dependence of capacity as function for moisture content of 0 %, 0.05 %, 0.15 % and 0.25 % in transformer oil (waveforms increase with moisture content)

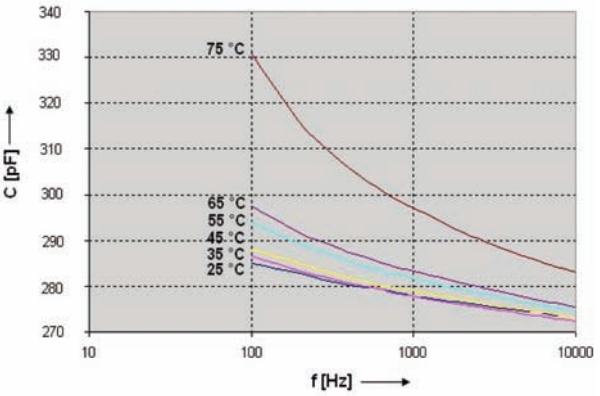

Fig. 6 The frequency dependence of capacity as function of oil temperature

In the last step we measured temperature dependence of the dissipation factor tg(δ) at 100 Hz (Fig. 7). The ranges of temperatures were determined by normal stages of the transformer (20 °C to 75 °C) and the temperature 85 °C (transformer thermal overload, the polarization index is close to 1). The dissipation factor increases with temperature and at the temperature around 50 °C there is a visible step. These results were compared with the values of insulating resistances at 15 s and 60 s (R15 a R60 – Fig. 7). The insulating resistances R15 and R60 decrease with temperature and at temperature over 75 °C resistance values are very similar. In the range of temperatures 40 – 60 °C there can be seen steps on the waveforms – represented by a dash circle. Resultant similarities between insulation resistances and dissipation factor show that we verified the connection between both these methods.

6. Conclusion

Based on the measurements we proved correctness and high sensitivity of both methods for determination of transformer oil

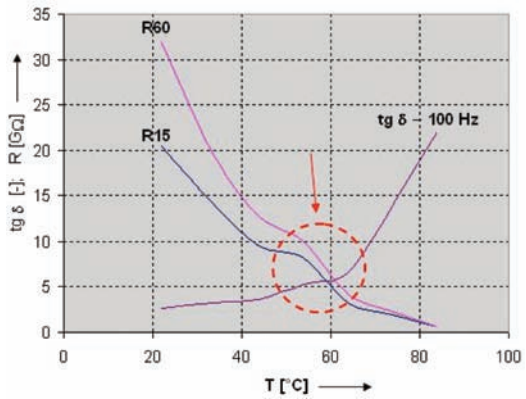

Fig. 7 The temperature dependence of dissipation factor tg(δ), R15 and R60.

humidity in the transformer, i.e. the frequency monitoring of capacity or tg(δ) to 10 kHz. These methods can be utilized to determine an insulation state during a short term layoff of the transformer and thus increase its reliability and safety.

Acknowledgments

This work was supported by the Grant Agency VEGA from the Ministry of Education of the Slovak Republic under contract 1/0515/09 and 1/0548/09.

References

[1] GUTTEN, M.: *Diagnostic and Monitoring of Power Transformers,* Proc. of 5th International Conference Elektro 2004, Zilina 2004, pp. 300–301,

[2] MARTON, K., KURIMSKY, J., BALOGH, J.: *Partial Discharges in the Diagnostics of Transformers (in Slovak),* In: Monitorovacie a diagnostické systémy transformátorov, EDIS ZU, Zilina, 2007, pp. 23–45,

[3] ARTBAUER, J., SEDOVIC, J., ADAMEC, V.: *Insulators and insulations (in Slovak),* ALFA, Bratislava, 1969, ,

[4] Manual Fluke 6306 - RLC meter,

[5] http://assets.fluke.com/images/products/fpm/bench_in-struments/ds_rcl_6304_6.pdf

[6] GUTTEN, M., KUDELCIK, J.: *Effect of humidity in the transformer on its safety and reliability (in Slovak),* In: ELDICOM 09, Zilina, 2009, pp. 45–47.

D. Pudis – I. Kubicova – L. Suslik – J. Skriniarova – I. Martincek – I. Novotny *

PATTERNING TECHNIQUES FOR FABRICATION OF SUBMICROMETER STRUCTURES IN PHOTORESIST, III-V SEMICONDUCTORS AND PMMA

This paper presents experimental results in the field of planar periodic structures, their fabrication and analysis. We demonstrate techniques and experimental results of fabrication of two-dimensional periodic structures and their preparation in a thin photoresist layer, III-V semiconductors and PMMA - interference lithography using two coherent laser beams, nanoimprint lithography and lithography using near-field scanning optical microscope.

1. Introduction

New applications in photonics and optoelectronics are focused on exploitation of periodic structures known as photonic structures. The photonic structures with submicrometer period enable to change the optical and electrical properties of optic and optoelectronic devices.

Periodic structures can be fabricated by different lithography techniques as holographic lithography [1, 2], electron beam lithography [3], nanoimprint lithography [2, 4, 5] and near-field scanning optical microscope lithography [6–9]. Techniques presented in this paper allow maskless definition of surface microstructures.

One of the simplest ways how to obtain microstructures with two-dimensional geometry (2D) is holographic lithography based on a double-exposure process using two-beam interference optical field [1, 5, 6]. In this way, the holographic lithography produces high-resolution periodic structures in a large area with low costs. These periodic structures patterned in a thin photoresist layer can be employed as a mask for the patterning of III–V semiconductor surfaces, which may be attractive for optoelectronic and photonic applications [10]. However, due to the diffraction limit, it is very difficult for the holographic lithography to reach the subwavelength resolution. The subwavelength resolution can be achieved by submicron-diameter optical fiber, where the metal coated fiber tip is used as a subwavelength fiber probe for a local exposure [6]. A combination of such a fiber probe with nanopositioning system can be used as the near field scanning optical microscope lithography with high exposure resolution.

Unlike the above optical forms of patterning that employ radiation to delineate a pattern in a resist, non-radiation based patterning uses a mechanical mold that shapes a material into features. One of these techniques is nanoimprint lithofraphy (NIL). As the NIL's working principle is fundamentally different from radiation-based lithography, it has many advantages over conventional lithography, as high pattern transfer fidelity, larger area and high throughput [4, 5]. NIL does not use any energetic beams; therefore its resolution is not limited by the effects of wave diffraction, scattering and interference in a resist and backscattering from a substrate. Moreover, they can directly pattern functional materials to reduce fabrication steps.

In this work we present experimental results from holographic lithography of two beam interference method and near field scanning optical microscope lithography as effective optical techniques for the preparation of 2D periodic structures in a thin photoresist layer as well as on GaAs surfaces. Non-optical possibility of structure patterning was examined in PMMA material using nanoimprint lithography.

2. Two-Dimensional Structures Patterned by Interference Lithography

Holographic lithography using two beam geometry allows to design one and two dimensional periodic structures by a simple theoretical approach of interference of two optical plane waves. The intensity distribution of the interference pattern of two optical plane waves with the same intensity in the *xy* plane can be expressed as [1]

$$I_{\alpha} = 4I_0 \cos^2\left[k \sin\theta\left(x\cos\alpha + y\sin\alpha\right)\right], \qquad (1)$$

where I_0 is the intensity of the interfering beams, k is the wavenumber, θ is the semiangle between two interfering beams and the

* D. Pudis[1], I. Kubicova[1], L. Suslik[1], J. Skriniarova[2], I. Martincek[1], I. Novotny[2]
[1] Dept. of Physics, University of Zilina, Slovakia
[2] Dept. of Microelectronics, Slovak University of Technology, Bratislava, Slovakia, E mail: pudis@fyzika.uniza.sk

angle α represents the sample orientation in the *xy* plane (Fig. 1). The optical field periodicity Λ is then determined by

$$\Lambda = \frac{\lambda}{2\sin\theta}, \qquad (2)$$

where λ is the wavelength of the interfering beams.

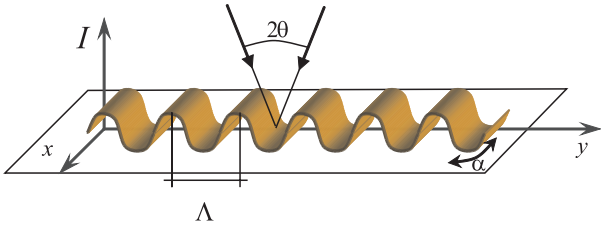

Fig. 1 In-plane intensity distribution of two interfering beams containing angle 2θ for defined sample rotation α according eq. (1)

The schematic in-plane distribution shown in Fig. 1 documents only 1D field distribution. The multiexposure process is necessary for the preparation of 2D periodic structures. In case of double exposure at different angles of sample orientation α, the exposure dose is accumulated and the total exposure is the sum of the partial exposures $I_{tot}(x,y) = I_1 + I_2$ what finally forms 2D optical field distribution.

2.1. Experiment

Periodic structures can be prepared on different metal and semiconductor surfaces by interference lithography. In this experiment the interference optical field is formed by the interference of two coherent beams of the Argon ion laser operating at 488 nm. A positive photoresists AZ 5214E layer is used as a mask [11]. The 10x expander was used for improving the exposure homogeneity in the exposed area with a diameter of 5 mm which resulted in the exposure intensity of 25 mW/cm^2 both laser beams.

For the patterning of GaAs samples, n-doped GaAs substrates were covered with 0.7 μm thick photoresist film as a mask. The photoresist film was spin-coated with post-baking at 103 °C for 50 seconds. After the exposure and photoresist development, the samples were etched by Reactive ion etching (RIE) in CCl4/He based plasma in ROTH & RAU MICROSYS 350 machine [10]. Only a weak absorption is documented for this type of employed photoresist in the region of the Ar laser wavelength, which effects insufficient polymerization of the photoresist at short exposition times. Then the sample exposure was realized at exposition time in the range of 10-12 min. Finally the structure quality was examined by an atomic force microscope (AFM).

2.2. Results and discussion

2D photonic structures with square symmetry were prepared on GaAs surface using a double exposure process with sample in-plane rotation between the exposures at angle α = 90°. The period of 2D photonic structure was set in the experiment to be Λ = 2.0 μm.

The distribution of 2D optical field in a double exposure process typically can be described by a sinus function in *xy* plane [1]. The sinusoidal shape was formed into the exposed photoresist layer with the depth of approximately 600–700 nm in the developing process with duration of 25–30 s [11]. Additional developing starts a formation of the open regions in the photoresist mask (30–40 s). The additional developing process (>40 s) enlarges the open regions. Photoresist masks prepared in this way with different shaped open regions were used for the formation of 2D structures onto GaAs surface.

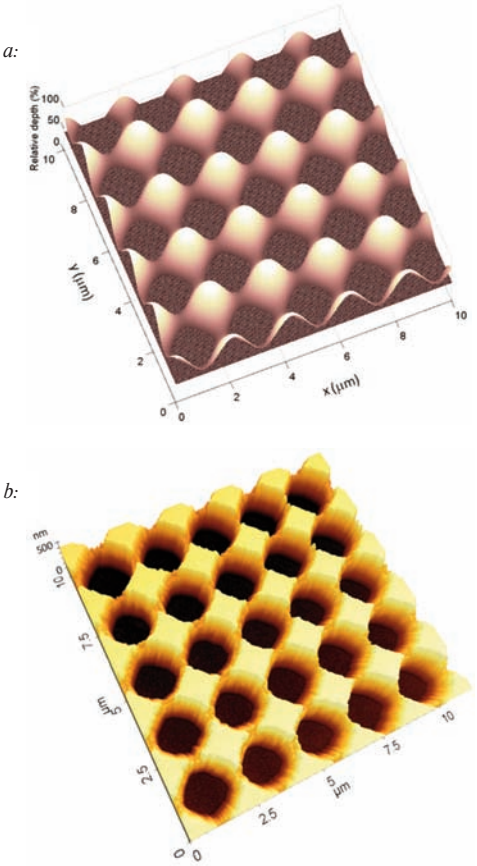

Fig. 2 a) Simulation of the open regions (dark area) in the photoresist mask, b) AFM image of prepared 2D photonic structure in the GaAs substrate

The following RIE process preserves the shape of the photoresist mask in GaAs substrate. Fig. 2a demonstrates a simulation of photoresist patterning on the GaAs surface after developing. AFM image (Fig. 2b) shows the real etched structure in GaAs substrate with the removed regions. These regions correspond to the nearly

square shape of the photoresist mask (Fig. 2a). By etching the deep structures (app. 500 nm), the final shape of structure reflects also the photoresist mask thickness. It is evident on the barriers overetching, where the thickness of photoresist mask is the lowest. This method allows the formation of open regions of different size depending on the developing time, as well as on the time of RIE process and experiment geometry [10, 11].

3. Nanoimprint in PMMA

Nanoimprint lithography has two basic steps as shown in Fig. 3. The first is the imprint step in which a mold with nanostructures on its surface is pressed into a thin resist cast on a substrate, followed by the removal of the mold. This step duplicates the nanostructures on the mold in the thin resist layer. The second step is the pattern transfer where an anisotropic etching process, such as RIE, is used to remove the residual resist in the compressed area. This step transfers the thickness contrast pattern into the entire resist [5].

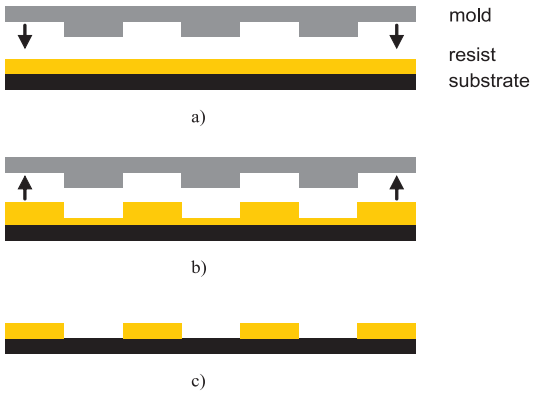

Fig. 3 Schematic of nanoimprint lithography process: a) imprinting by pressing the mold, b) mold removal, c) residual resist removal by anisotropic etching process [5]

3.1 Experiment

In our experiment, GaAs was used as the mold material. The mold was patterned by two-beam interference holographic lithography shown in Fig. 2b. The period of the prepared mold structure was 2.0 μm and the intrusion of about 550 nm. Because of the small pressure shrinkage coefficient, the acetone solution of polymethyl methacrylate (PMMA) was used as the resist. The PMMA layer thickness was kept thicker than the mold intrusion to prevent the mold from contacting the substrate. The PMMA structure quality was examined by AFM after the process.

3.2 Results and discussion

The period of the imprinted PMMA structure is 2.0 μm and the depth is of about 250 nm as shown in AFM image (Fig. 4).

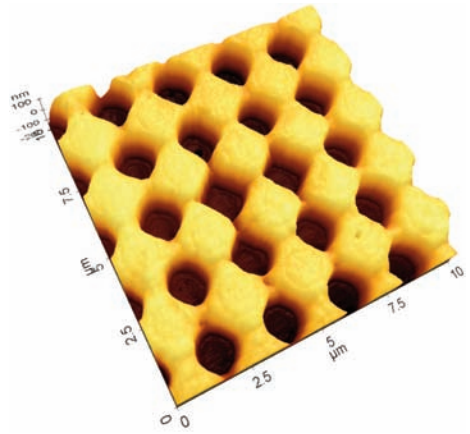

Fig. 4 AFM image of 2D periodic structure prepared in thin PMMA layer

When comparing the imprinted PMMA with the mold characteristics (Fig. 2b), the structure period is left unchanged, but the depth is lower than the mold intrusion. The fact is caused by the presence of air during imprinting. However, nanoimprint using GaAs mold may be a promising technique achieving better than submicrometer resolution if applied in vacuum.

4. Nanopatterning Using NSOM Lithography

Among different types of existing methods for fabrication of nanostructures, near-field scanning optical microscope (NSOM) lithography is one of the favored techniques. The patterning of nanostructures is done through a direct writing process which is performed by the optical near-field produced at the tip of a fiber probe. Therefore, the fabrication of nanostructures in a size below the diffraction limit of the light source that poses the ultimate resolution limit in conventional optical lithography is possible [6]. Also there is no need for mask preparation as it is in photolithography, and the patterning can be performed in air. On the other hand, as the interaction between the optical near-field and the sample surface is a photochemical process, conventional materials used in far-field optical lithography, for example photoresists, can be used [6, 7, 12].

4.1. Experiment

We focused on experimental investigation of NSOM lithography for the preparation of structures using a conventional nanopositioning stage and a fiber probe. A schematic diagram of the experimental arrangement is shown in Fig. 5. A 473 nm continuous wave DPSS laser was used as the light source. The laser beam was focused into conventional optical fiber, which was coupled to the fiber probe. Even though interesting results can be obtained using the contact mode [6, 12], we arranged non-contact mode of NSOM lithography. In the non-contact mode the fiber was fixed on the 3D nanopositioning piezosystem to realize the 3D movement of

the fiber probe over the sample. Two different types of fiber probe were used, a conventional optical fiber of 10 μm core diameter and the metal-coated fiber tip with a submicrometer aperture on the output side.

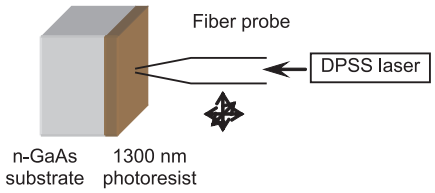

Fig. 5 Experimental arrangement for NSOM lithography

The positive photoresist AZ 5214E was used for patterning. For the sample preparation, the 1300 nm thick photoresist film was spin-coated on a GaAs substrate. The patterning of the photoresist was carried out by moving the fiber probe over the sample while the laser light was irradiated through the fiber probe aperture. After exposure, the sample was developed in AZ 400K developer for 30 s, rinsed in DI water. The structure quality was examined using an optical microscope. Dektak 150 Stylus Profiler using Vision 3D advanced analysis software was used to determine topography of dots prepared by metal-coated fiber tip.

4.2. Results and discussion

The patterning of dots as well as lines was tested using the conventional optical fiber of 10 μm core diameter. This fiber probe was placed approximately 10 μm from the sample surface. Different structures prepared by NSOM lithography are shown in Fig. 6. The lattice in Fig. 6b was created by exposure of 5 horizontal and 5 vertical lines with 50 μm pitch step. When using the 10 μm core diameter optical fiber, the line width of 12 μm was achieved. This line widening is caused by a divergence of the irradiated optical field at the end of the fiber probe.

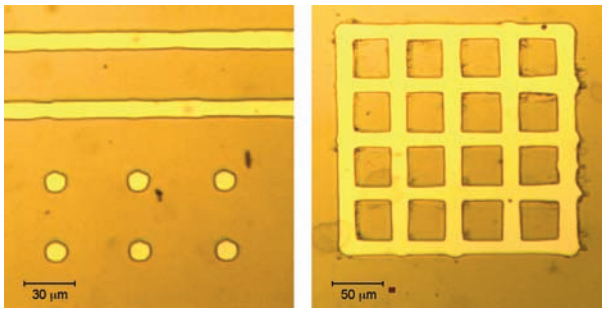

a) *b)*

Fig. 6 a) Lines and dots; b) lattice exposed by optical fiber

To shrink the line width of the structure and to improve the technique resolution, the metal coated fiber tip with a smaller aperture was used. The results using the metal coated fiber tip demonstrate the resolution improvement to be lower than 3 μm. An array of 3 by 3 dots was exposed as shown in Fig. 7. The exposure time was set to one, two and three seconds for each dot in the 1st, 2nd and 3rd line, respectively.

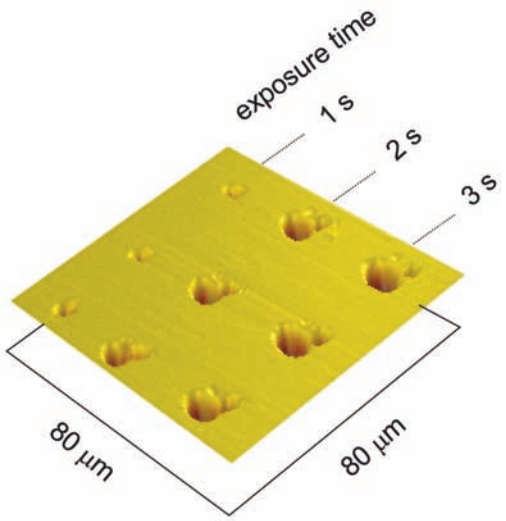

Fig. 7 Dektak image of dots exposed by NSOM lithography using the metal coated fiber tip

Dektak image shown in Fig. 7 documents a dependence of dots diameter on the exposure time. The longer exposure time forms the dots of a higher diameter. The smallest dots of a diameter lower than 3 μm were achieved at 1 s exposure time. The diameter of prepared open regions is then function of the exposure time, because of the gaussian shape of the optical field of the metal coated fiber tip. Therefore, by keeping shorter exposition times the submicrometer resolution is expected. On the other side, the exposed area reflects a non-homogeneity of the prepared fiber tip. Then, the final pattern slightly differs from circular shape as it is documented in Fig. 7.

5. Conclusion

The subject of the paper was the investigation of techniques for the fabrication of planar periodic structures and their possibilities to fabricate periodic structures in the photoresist material, GaAs and PMMA surfaces. The two beam interference method was presented as an effective tool for the fabrication for 2D periodic structures with a small periodicity by using the standard photoresist. The shape and period of the formed structure can be simply adjusted by experiment geometry. This method was successfully examined for the preparation of 2D periodic structures with a period of 2 μm in thin photoresist film deposited on the GaAs surface.

The patterned 2D periodic structure on GaAs substrate was used as a mold for the nanoimprint technique. The inverse structures were successfully imprinted in PMMA layer.

The fabrication of microstructures was examined by NSOM lithography as well. The planar pattern consisting of dots and lines was examined by NSOM lithography using a standard optical fiber probe as well as using a metal coated fiber tip, where the resolution better than 3 μm was achieved.

The variability of presented techniques opens wide possibilities to form submicrometer periodic structures on different surfaces of organic and semiconductor materials, which favors these lithography techniques for applications in the region of photonic and electronic devices.

Acknowledgement

This work was partly supported by the Slovak National Grant Agency No. VEGA 1/0868/08, 1/0220/09, 1/0689/09 and 1/0683/10. The authors wish to thank for the support to the R&D operational program Centre of excellence of power electronics systems and materials for their components. The project is funded by the European Community, ERDF – European regional development fund.

References

[1] LAI, N.D., LIANG, W.P., LIN, J.H., HSU, C.C., LING, CH. H.: *Opt. Express* 13, 2005, pp. 9605–9611.
[2] KIM, S. H., LEE, K.D., KIM, J.Y., KWON, M.K., PARK, S.J.: *Nanotechnology* 18, 2007, p. 055306.
[3] VITTORIO, M. DE, TODARO, M.T., STOMEO, T., CINGOLANI, R., COJOC, D., FABRIZIO, E. DI: *Microelectron. Eng.,* 2004, pp. 73–74.
[4] MURPHY, P.F., MORTON, K.J., FU, Z., CHOU, S.Y.: *Appl. Phys. Lett.* 90, 2007, p. 203115.
[5] CHOU, S.Y., KRAUSS, P.R., RENSTROM, P.J.: *J. Vac. Sci. Technol. B* 14, pp. 4129–4133.
[6] WEGSCHEIDER, S., KIRSCH, A., MLYNEK, J., KRAUSCH, G.: *Thin solid films* 264, 1995, pp. 264–267.
[7] KWON, S., CHANG, W., JEONG, S.: *Ultramicroscopy* 105, 2005, pp. 316-323.
[8] DRYAKHLUSHIN, V.F., KLIMOV, A. YU., ROGOV, V.V., VOSTOKOV, N.V.: *Appl. Surf. Sci.* 248, 2005, pp. 200–203.
[9] LIN, Z.CH., YANG, CH.B.: *Scanning* 28, 2006, pp. 32–41.
[10] PUDIS, D., SKRINIAROVÁ, J., MARTINCEK, I., KOVAC, J. JR., TARJANYI, N., HASCIK, S.: *J. Electr. Eng.* 60, 2009, pp. 166–169.
[11] SKRINIAROVA, J., PUDIS, D., MARTINCEK, I., KOVAC, J., TARJANYI, N., VESELY, M., TUREK, I.: *Microelectron. J.* 38, 2007, pp. 746–749.
[12] TIAN, F., YANG, G., BAI, J., XU, J., HOU, CH., LIANG, Y., WANG, K.: *Opt. express* 17, 2009, pp. 19960–19968.

S. Jurecka – I. Jamnicky *

STUDY OF THE DENSITY OF STATES DISTRIBUTION IN THE SiO_2/Si STRUCTURE

Interface properties of Al/SiO_2/Si MOS structures with NAOS oxide layer were analyzed by the construction of the capacitance-voltage model with the interface states. Energy distributions associated with the localized states in silicon band gap were modeled by the Gaussian distribution. Energy levels of localized states and the densities of interface states were determined. The results correspond with the results of the interface states study performed by the acoustic deep-level transient spectroscopy.

1. Introduction

High quality ultrathin SiO_2 layers with unique structural and electrical properties were prepared on n-type silicon substrate by the nitric acid oxidation of silicon method (NAOS) [1–3]. The interfacial properties between silicon and SiO_2 layer severely impact the carrier mobility and influence the electrical properties of the structure. The interface defects need to be well characterized in order to improve the quality of the whole semiconductor device. Chemical impurities or defects in periodical crystal lattice structure of silicon create the perturbations of the lattice. The periodicity of crystal lattice is important for the band structure properties. Many defects cause bound states in the energy band gaps of a given crystal. It is very difficult to calculate the energy levels of these bound states and, therefore, various specific approximations are used. The states in the band gap can be divided into shallow states close to the edges of the band gap and the deep states, which lie near the middle of the band gap. Defect states in the band gap influence the properties of the semiconductor by modifying the mobility of charge carriers and by acting like donors or acceptors.

Typical interface state densities in metal-oxide-semiconductor (MOS) structures can be on the order of 10^{11} - 10^{13} $eV^{-1}cm^{-2}$, depending on materials and processing. A simply way to evaluate the interface trap density includes capacitance-voltage (C–V) measurements at low frequencies. The leakage current in thin dielectric film disturbs these low frequency C–V measurements. In order to model the C–V curve including the interface state behavior, the energy distribution and frequency response of the interface state should be described properly.

In our work we constructed a simple physical model to describe frequency dependent C–V curves of Al/SiO_2/Si MOS structure with NAOS oxide layer and with interface states. The model is based on a superposition of several types of energy distributions describing the density of interface states which enables computation of the frequency response of these interface states.

2. Model of Capacitance curves for MOS Structure with Interface States

The total charge density in the semiconductor ρ is given by equation

$$\rho = q\left(p - n + N_d^+ - N_a^-\right) , \qquad (1)$$

where p and n are hole and electron densities, N_d^+ and N_a^- are the densities of the ionized donors and acceptors, relatively. The total space charge density Q_S as a function of the surface potential Φ_S is shown in Fig. 1.

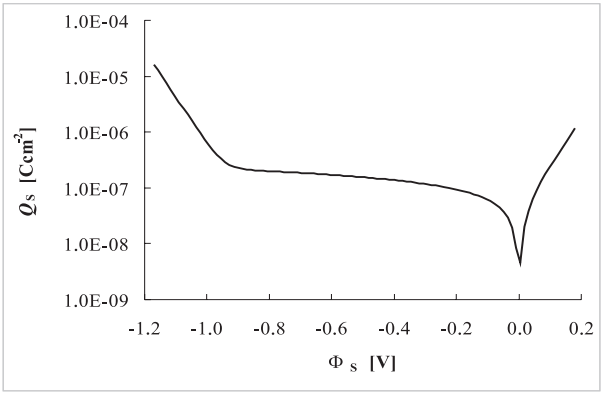

Fig. 1 The total space charge density Q_S in MOS structure

* S. Jurecka[1], I. Jamnicky[2]
[1] DEF FEE, Universtiy of Zilina, Liptovsky Mikulas, Slovakia
[2] DP FEE, University of Zilina, Slovakia, E-mail: jurecka@lm.utc.sk

Solution of the Poisson equation with this charge density leads to the capacitance of MOS structure without the interface states C_c [4]. Important electrical effect of the deep states in the band gap is the emission and capture of charge carriers. The defects play role of recombination and trapping centers, influence the carrier lifetimes and cause various transient processes. In the case of an n-type of semiconductor in deep depletion mode the presence of holes is negligible. Trap states interact only with electrons and define the semiconductor-oxide interface properties. Both neutral and positively charged traps can capture an electron. A negatively charged trap does not capture an electron; it remains negative and behaves as fixed charge in the MOS structure. Charge capture/emission processes connected with the interface states can be modeled by the equivalent effective capacitance C_{ite} associated with the interface states [5]

$$C_{ite} = \frac{dQ_{ite}}{d\Phi_S} = qD_{it} \tag{2}$$

where Q_{ite} is total charge at the effective interface state, Φ_S is a surface potential, q is an unit charge and D_{it} is the interface state density. We compute the D_{it} by superposition of several distributions

$$D_{it} = D_{itu} + D_{it\,\mathrm{exp}} + \sum_i D_{it} G_i \tag{3}$$

Distribution D_{itu} describes the uniform distribution of interface states across the band gap of semiconductor

$$D_{itu} = D_u, \tag{4}$$

where D_u is constant. Distribution $D_{it\,\mathrm{exp}}$ describes an exponential change of interface state density as the energy level becomes shallower to the band edge

$$D_{it\,\mathrm{exp}} = D_{\mathrm{mid}} \exp\left(\frac{E_t - E_i}{\alpha}\right), \tag{5}$$

where D_{mid} is the density of interface states at the midgap, α is constant, E_t and E_i are energy level and intrinsic Fermi level, respective. Distributions D_{itG} are used for the description of interface states localized in its energy levels. The Gaussian distribution is used in this work

$$D_{itG} = D_{G0} \exp\left(-\left(\frac{E_t - E_{t0}}{2\sigma}\right)^2\right). \tag{6}$$

Here, D_{G0} is the maximum energy of localized interface state, E_{t0} is the central energy of localized state, and σ is the standard deviation. We use superposition of several Gaussian distributions localized in different central energies E_{t0_i} with different maxima D_{G0_i} and standard deviations σ_i.

The capture/emission times of interface states affects the frequency response of the capacitance. The effective equivalent capacitance and interface state density determined experimentally change with energy level and frequency. We measured capacitance of MOS structure at various frequencies and we fitted experimental capacitances by theoretical models of capacitance curves with the interface states. These theoretical capacitances were computed by considering the equivalent circuit of actual MOS structure as shown in Fig. 2. The equivalent effective capacitance associated with the interface states C_{ite} and C_c is connected in parallel.

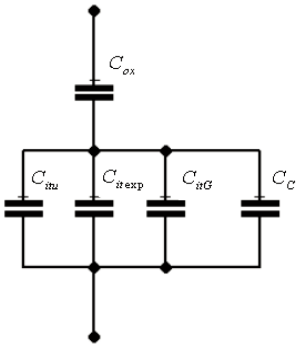

Fig. 2 Equivalent circuit for the MOS structure with interface states. C_{ox} is capacitance of NAOS oxide layer, C_{itu}, $C_{it\,exp}$ and C_{itG} are capacitances associated with D_{itu}, $D_{it\,exp}$ and D_{itG}, respectively

3. Experiment

Silicon MOS structure was prepared at n-type (10 Ωcm) Si(100) substrate. The substrate was cleaned by the RCA method and etched in diluted hydrofluoric acid. Ultrathin SiO_2 layer with ~2.5 nm thickness was then prepared by the NAOS method and finally the Al layer was formed. Electrical measurement of MOS capacitance was performed using FLUKE programmable automatic RCL meter at frequencies 1, 10, 100 and 1000 kHz.

4. Results and Discussion

The details of experimental C–V curves for given MOS structures are shown in Fig. 3. The influence of the interface states

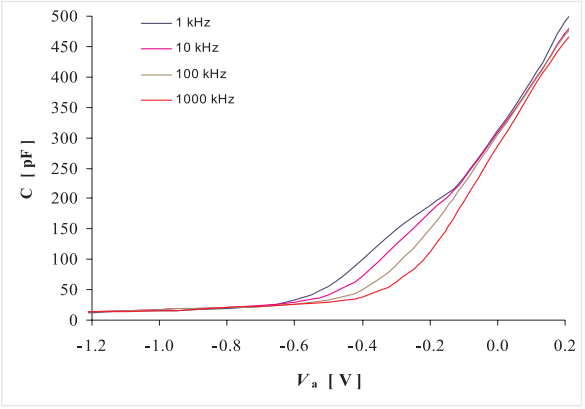

Fig. 3 C–V curves measured at Al/SiO_2/Si MOS structure with NAOS SiO_2 layer prepared at n-type silicon substrate

occurring at the semiconductor/oxide boundary can be observed in the depletion region of C–V curves. Experimentally determined MOS capacitance and theoretical model of MOS capacitance with the interface states at frequency $f = 1$ kHz are compared in Fig. 4.

Mean value of energy of localized states modeled by D_{itG_1} is in this case $E_{itg10} - E_i = -0.39$ eV, value of density of states associated with this energy level is $D_{itG_{10}} = 1{,}11.10^{13}$ eV^{-1}cm^{-2}.

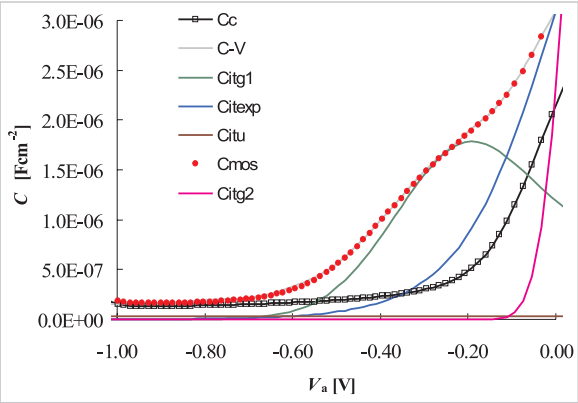

Fig. 4 Theoretical model of the capacitance of real MOS structure at frequency 1 kHz. C_{mos} is capacitance with the interface states, C_c is capacitance without D_{it}, C-V is experimental capacitance curve, C_{itg1}, $C_{it\ exp}$, C_{itu} are capacitances associated with D_{itG1}, $D_{it\ exp}$, D_{itu} respectively

Identical modeling procedure was used for the determination of energy levels and densities of interface states associated with these energies from the capacitance curves measured at a set of different frequencies. Frequency behavior of localized interface

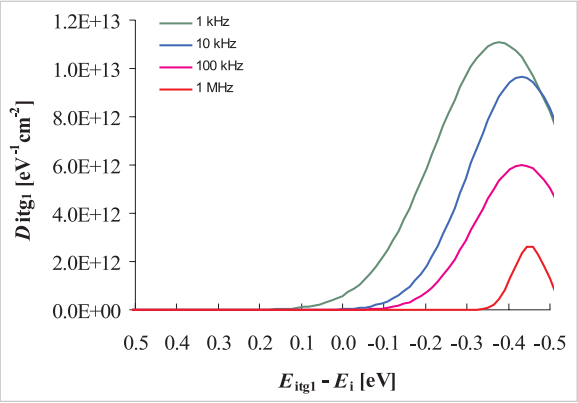

Fig. 5 Theoretical models of the densities of localized states modelled by the Gaussian distribution D_{itG1} at frequencies 1, 10, 100 and 1000 kHz

states described by the distribution extracted from the capacitance curves is shown in Fig. 5.

The frequency shift of the D_{itG1} distribution depends on the emission time of the interface states. The distribution of the interface state density is asymmetric; the density above midgap is lower. At lower frequencies the distributions are higher due to the effective excitation of recombination and trapping centers. The energy levels and corresponding densities of localized interface states in the energy gap of silicon substrate are shown in Table 1.

Results of the density of localized interface state analysis. Table 1

frequency	$E_{itg10} - E_i$	D_{itg10}
kHz	eV	eV^{-1}cm^{-2}
1	− 0.39	$1.11 . 10^{13}$
10	− 0.43	$9.67 . 10^{12}$
100	− 0.45	$6.01 . 10^{12}$
1000	− 0.46	$2.62 . 10^{12}$

Localized states described by the D_{itG2} distribution do not fall into the energy gap of Si and are not shown in Table 1. Densities of deep interface states in silicon energy gap are extremely reduced in MOS structure with NAOS SiO_2 oxide layer. This result corresponds very well with the results of the interface states study in the MOS structures by the acoustic deep-level transient spectroscopy [6].

5. Conclusions

Density of interface states in MOS structure with ultrathin NAOS SiO_2 layer was determined by the capacitance-voltage measurements at various frequencies. Different frequency responses of C–V curves were experimentally observed and theoretical model for explaining of these experimental results was constructed. Theoretical model of C–V curves is based on computation of equivalent capacitance of MOS structure corresponding to the density of interface states. This approach is motivated by simple physical assumptions and enables modeling of the frequency response of the charge trapping processes. Densities of states in MOS structure were modeled by the superposition of several distributions. Localized interface states modeled by Gaussian distribution provide good description of frequency behavior of C–V curves. Energy levels of interface states determined by extraction of Gaussian distribution from theoretical capacitance model are localized close to the valence band. The densities of deep interface states in silicon band gap are extremely reduced in MOS structure with NAOS oxide layer.

Acknowledgement

This work was supported in part by the Slovak grant agency under grant APVV 0577 – 07 and ITMS 26220120003.

References

[1] ASUHA A., YUSA T., MAIDA O., KOBAYASHI, H.: *Appl. Phys. Letts.* 80, 2002, pp. 4175.
[2] KOBAYASHI, H., ASUHA, A., MAIDO, O., TAKAHASHI, M., IWASA, M.: *J. Appl. Phys.* 94, 2003, pp. 7328.
[3] IM S-S., TERAKAWA S., IWASA H., KOBAYASHI H.: *Appl. Surf. Sci.*, 254, 2008, pp. 3667–3671.
[4] SZE S. M., NG K. K.: *Physics of Semiconductor Devices.* John Willey & Sons, New Jersey, 2007.
[5] INOUE N., LICHTENWALNER, D. J., JUR. J. S., KINGON, A. I.: *Jap. J. of Appl. Phys,* Vol. 46, 10A/2007, pp. 6480–6488.
[6] BURY, P., KOBAYASHI, H., TAKAHASHI, M., IMAMURA, K., SIDOR, P., CERNOBILA, F.: *Cent. Eur. J. Phys.* 7(2), 2009, pp. 237–241.

Juliana Knocikova *

ALTERATIONS IN SIGNAL DYNAMICS DURING REGULATION OF AIRWAY REFLEX RESPONSE

Regulatory airway mechanisms were studied on the basis of phrenic nerve activity which was compared during eupnea and aspiration reflex (AspR). Due to changing degrees of signal stationarity, discrete wavelet transformation enabling multiresolution analysis was performed, followed by calculation of wavelet energy and wavelet entropy parameters.

The higher rate of wavelet energy was detected in lower frequency components during AspR in contrast to eupnea. Moreover, quiet inspiration is characterized by higher wavelet entropy comparing to the AspR, indicating the probability of its random character and varying degree of system disorder during transient between different respiratory responses.

Key words: biosignal processing, respiratory control, reflex, wavelet energy, entropy

1. Introduction

Since the early days of neuroscience research, understanding the regulation of physiological processes has become a fully multidisciplinary task, highly dependent on the usage of principles from mathematics, physics and computer science in many aspects of view. As a question resulting from the information theory, regulation on respiratory reflex responses is conditioned by a degree of synergy related to complex multilevel and multibehavioral neuronal networks in the rostral ventrolateral medulla. Generation of respiratory activity and its modulation towards the organism's requirements remains still not fully explained.

Information resulting from the control mechanisms is carried through nerves and muscles to achieve desired response and expressed in neurogram qualities, including timing, intensity, frequency composition and many others. Thus, the principal thesis of this approach is to suggest an optimal processing method considering fundamental irregular nature of biological signals.

Electrical signals resulting from different airway reflex responses have been traditionally analyzed via simple frequency analysis derived from the Fourier transformation. Power spectral analysis proved differences presented in power spectrum during eupnea (quiet inspiration) and other forms of inspiratory activity [1, 2]. However, Fourier transformation has many limitations in the case of electrophysiological data analysis [3], thus method involved in activity determination both in time and frequency domain appears to be necessary [4].

The intent of this work is to extract differences in phrenic neurogram between normal quiet inspiration and aspiration reflex (AspR) – strong inspiratory activity, without subsequent active expiration that could be, contrary to other airway defense reflexes, elicited in any phase of respiratory cycle and characterized by ability to interrupt severe functional disorders [5]. Thus, this specific reflex response could probably represent a model of the brainstem neuronal network reconfiguration [6].

In this paper, the motor behavior of different respiratory responses was described as a function of energetic distribution over time – frequency domain. The action potentials recorded from respiratory nerve output were analyzed during quiet inspiration and aspiration reflex to describe changes of dynamics related to its spectral features. Discrete wavelet transformation allowing multiresolution analysis was used to decompose original phrenic nerve recording into particular scale rates enabling determination of wavelet energy relating to separate frequency components. Moreover, the wavelet entropy parameter was calculated to illustrate a degree of system order/disorder, reflecting merits of respiratory activity generation and control.

2. Material and methods

2.1 Data recording and preprocessing

Phrenic nerve activity was recorded from five adult cats of both genders anesthetized by pentobarbital (initial intraperitoneal dose (35–40) $mg.kg^{-1}$). Aspiration reflex was elicited mechanically by touching the nasopharyngeal mucosa. An elastic nylon fibre (0.4 mm) was introduced through a pharyngostomy to elicit appropriate reflex. The electrical activity from right phrenic nerve was scanned using bipolar silver electrode which was connected to

* **Juliana Knocikova**
Department of Physics, Faculty of Electrical Engineering, University of Zilina, Slovakia, E-mail: knocikova@fel.uniza.sk

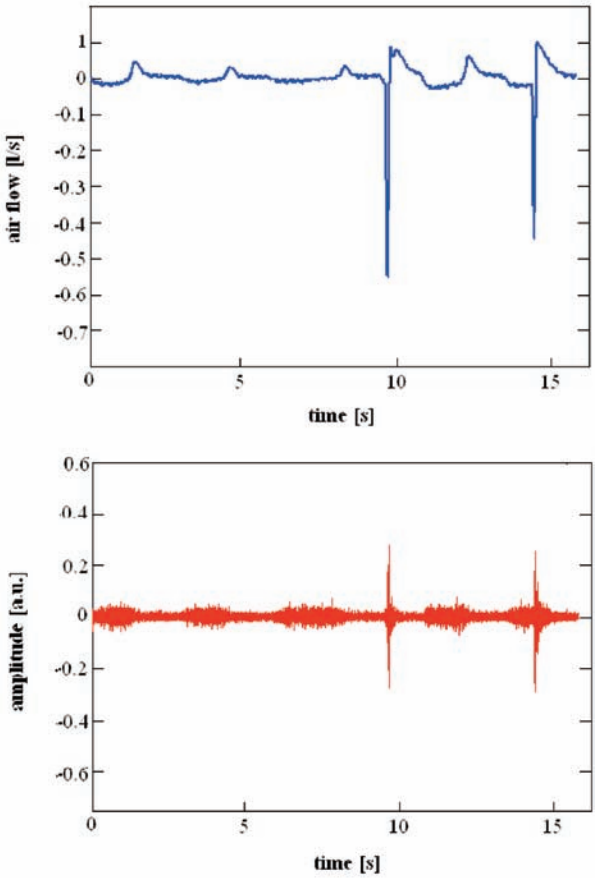

Fig. 1 Air flow and phrenic nerve recordings during quiet inspiration bursts followed by short strong inspiratory activity of AspR.

a low-noise amplifier. Neurograms were digitalized and sampled using minimum sampling rate of 2 kHz. These procedures have been described previously in details [2,7].

Nerve recordings (Fig. 1.) were pass-band filtered and frequency components from interval (30 – 1000) Hz were analysed. 50 Hz frequency was cut off through a stop-band elliptic filter to reduce impact of power supply noise on energy of correspondent frequency bands. The wavelet energy and entropy were calculated in 10 eupneic and 10 AspR bursts, only the single bursts of electrical phrenic nerve activity were considered.

2.2 Data analysis

Discrete Wavelet transformation (DWT)

The basic principle of the discrete wavelet function consists in signal decomposition into set of wavelets, small oscillations with limited duration and mean value equal to zero. DWT exploits a wavelet basis functions and exhibits zero redundancy. DWT coefficients could be calculated using the following formula:

$$\psi_{m,n}(p) = \frac{1}{\sqrt{s_0^m}}\psi\left(\frac{t - np_0 s_0^m}{s_0^m}\right), \quad (1)$$

where $m, n \in Z$.

Integers m and n control the wavelet dilation and/or translation; s_0 is a fixed dilation step parameter set at a value greater than 1 and p_0 is the location parameter set at a value greater than zero. Usually, a common choice for discrete wavelet parameters s_0 and p_0 is 2, known as the dyadic grid arrangement.

During DWT, lower frequencies of original signal (approximate coefficients) are separated from higher frequencies (detail coefficients) via low and high pass filtration. Number of data is then doubled. Approximate coefficients could be filtered again (Fig. 2.) to obtain approximate and detail coefficients at a higher frame (Fig. 3.) resulting in scale accommodation (scale 2^n for n – frame). In this study, decomposition at 8 level of approximate and detail coefficients was used. During this procedure, daubechies 3 was employed as a mother wavelet.

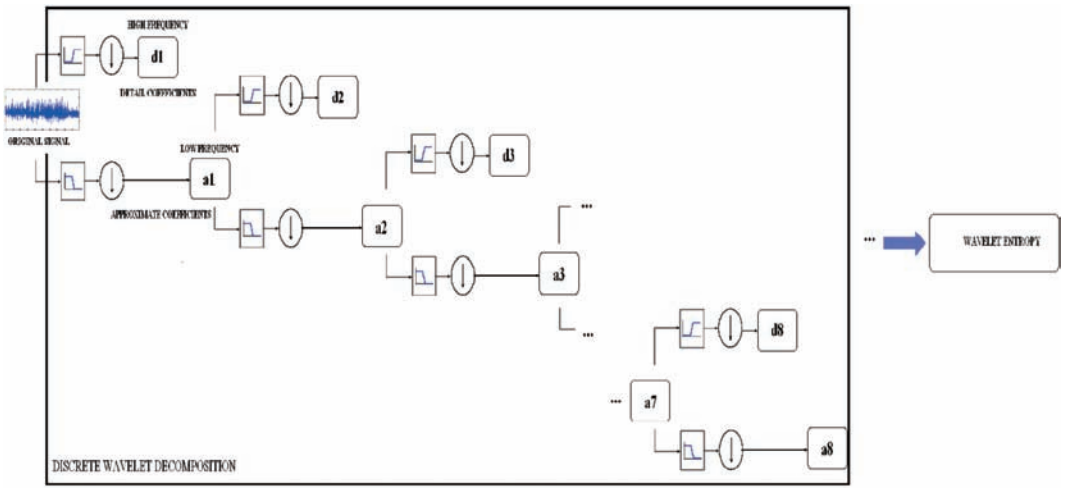

Fig. 2 Discrete wavelet decomposition of original phrenic signal at 8 level approximate and detail coefficients

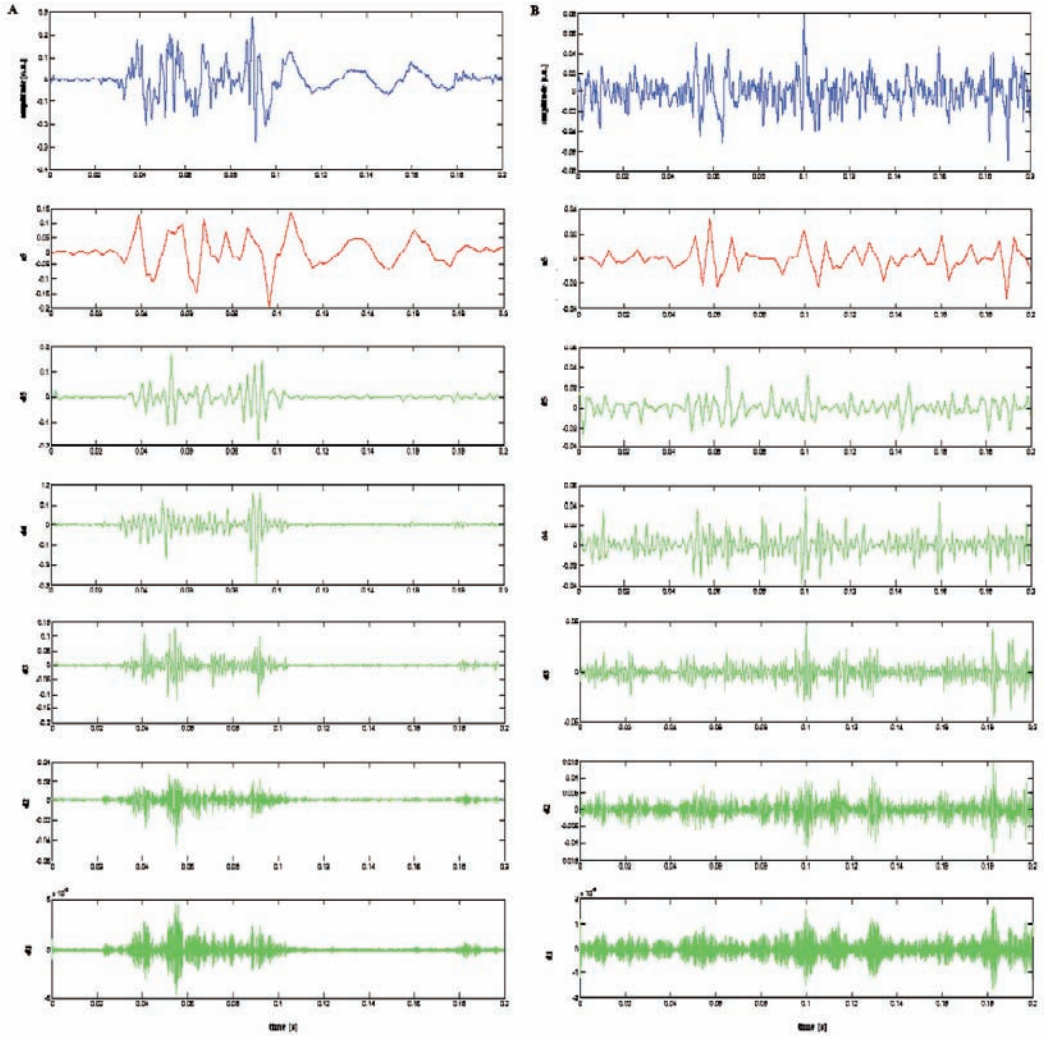

Fig. 3 Result of discrete wavelet decomposition of original activity (blue) during AspR (A) and eupnea (B). a – approximate coefficients, d – detail coefficients

Daubechies 3 is often used in biosignal analysis for detection of transient oscillations. Daubechies wavelet showed profitable properties for pattern classification during analysis of brain function [8]. Dynamical changes of the phrenic nerve electrical activity in time and frequency analyzed in this study probably reflect information about specific neuronal components involved in the generation of inspiratory activity.

Wavelet energy and wavelet entropy

For wavelet coefficients $c_s(k)$ at each resolution level s, the wavelet energy at each time sample k is obtained as:

$$E(k) = \sum_{s=1}^{S} |c_s(k)|^2 \tag{2}$$

The total wavelet energy is then computed as:

$$E_{TOT} = \sum_{s=1}^{S}\sum_{k=1}^{N} |C_s(k)|^2 = \sum_{s} E_s \tag{3}$$

Relative wavelet energy parameter quantifying the distribution of energy over appropriate scales is:

$$P_s = \frac{E_s}{E_{TOT}} \tag{4}$$

Thus, the wavelet entropy is defined as:

$$WE = -\sum_{s=1}^{S} p_s \log_2[p_s] \tag{5}$$

2.3 Statistics

All analyzed parameters were compared between two groups – phrenic bursts during aspiration reflex and quiet inspiration. 10 eupneic and 10 AspR bursts of phrenic electrical activity were

considered. The statistical evaluation of data was realized through unpaired t- test and Mann-Whitney test. Suitable test (parametric or nonparametric) has been chosen due to the fulfilment of condition for normal data distribution. Differences were considered significant for $p < 0.05$.

3. Results

Discrete wavelet transformation disclosed significant differences in time – frequency energetic distribution between both behaviors. During eupnea, the energy was distributed uniformly over the burst duration. However, energy of AspR was cumulated especially around the maximal intensity interval ($p < 0.05$).

Prominent energetic differences were detected in frequency domain. While AspR was characterized by strong energetic accumulation at lower frequencies corresponding to the approximate coefficients ($p < 0.0001$, Fig. 3), the eupneic activity showed increasing wavelet energy at higher frequency components ($p = 0.0022$), corresponding to interval (125 – 250) Hz.

Parameter wavelet entropy showed significant differences between analyzed groups (Fig. 4.). AspR resulted in its decreasing ($p = 0.0023$).

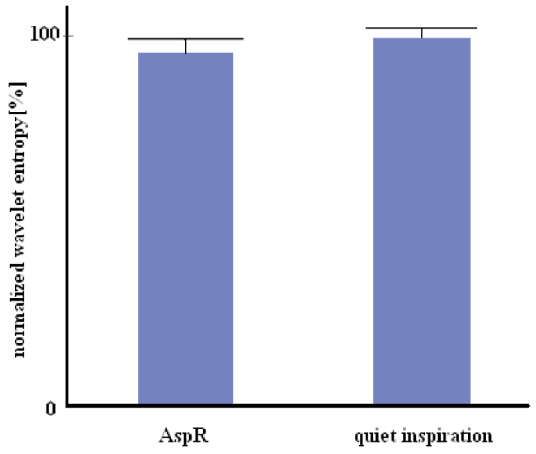

Fig. 4 The wavelet entropy measure normalized to averaged entropy of quiet breathing (mean ± standard deviation). AspR results in wavelet entropy decreasing ($p = 0.0023$).

4. Discussion

The most important finding of this study is that the time – frequency distribution of energy derived from phrenic nerve activity shows differences between two inspiratory activities. Lower frequencies are markedly involved in energy creation during aspiration reflex under comparison with eupnea. Moreover, eupnea results in increasing of wavelet entropy parameter.

As stated in Material and methods, we considered neural activities within the range of (30- 1000) Hz. With regard to analysis of the respiratory nerve outputs, the most interesting frequency range is above 30 Hz, including the high frequency oscillations in cat. These activities were described as the most distinguished signs of respiratory neurogram spectra, significantly contributing to the total power of inspiration [9].

In every sense, there is a lack of information regarding to spectral characteristics in AspR and their comparison with other defensive airway reflexes. Moreover, frequency components of respiratory outputs depend markedly on different experimental conditions and methodical approaches and major part of papers deals with different animal model, type of anesthesia or filtering methods significantly affecting the signal spectra. Previous studies of the cat phrenic nerve activity confirmed markedly different power spectra in AspR and eupnoe using Short Fast Fourier Transform [2]. This important identification was based on detection of typical high frequency oscillations and their position in power spectra as a solitary spectral characteristics. Therefore, analysis based on determination of wavelet entropy and time – frequency distribution of whole energy involved in phrenic bursts provides complementary findings in the field of spectral behavior of defensive airway reflexes.

The method of wavelet transformation, widely used for analysis of nonstationary and fast transient signals, represents effective alternative towards Fourier transformation. The most important advantage of the wavelet transformation consists in continuous changes of the mother wavelet (an alternative of window in Fast Fourier Transformation) according to its scale and time position. With regard to adapting length of the weighing function, wavelet transformation provides an adequate time and frequency localization of signal features by using short windows at higher frequencies and long windows at lower frequencies. An optimal time-frequency resolution [10] is reached by scaling and translation of mother wavelet function – a short duration oscillatory curve with zero-mean value [11]. Consequently, analyzed signal is decomposed into modified version of mother wavelet [12]. Therefore, lower frequencies (slow oscillations) are better distinguishable in frequency domain while higher frequencies (fast oscillations) are a better time distinguishable because of narrower window function [13].

Relative energy associated with different frequency segments of neurogram exhibits significant differences in analyzed recordings. Approximate coefficients representing lower frequency components are dominant in creation phrenic signal during aspiration reflex. Similar findings were observed in adult decerebrate rats [14] during gasp – aborted breath, accompanied by strange vocalizations and muscles twitching. Loss in high frequency oscillations could suggest possible reconfiguration of the respiratory network when switching from eupnea. Relationships between aspiration reflex and gasping have been previously studied because of their similar manifestation and possible implications in clinical practice, especially potential for resuscitation effect [6]. Presented method of wavelet energy computation acknowledged other behavioral similarities, including distribution of energy over different scale/

frequency segments related to phrenic neurogram in aspiration reflex and gasping development.

Wavelet entropy is a measure estimated by the wavelet coefficients to provide quantitative information about the order/complexity of analyzed signals [15]. As a method of time – series processing, entropy can describe dynamical cause associated with manifestation of different neurogram stages. Higher wavelet entropy value detected in eupneic activity reflects higher probability of system disorder comparing to AspR. From this point of view, quiet breathing sounds like more random, irregular behavior. Probably, the total wavelet entropy may reflect synchrony level of neural firing [16]. Other investigators suppose that entropy could be an effective tool for measuring diffusion energy over neurons or degree of synaptic activity.

Decreased signal complexity during coughing and swallowing reflex in contrast to eupnea was investigated on the basis of the phrenic approximate entropy determination [17]. Similarly, implication of wavelet entropy analysis in this study certified random eupneic mode. Thus, reduced signal complexity probably results from synchronous activity of a homogeneous group of neurons during airway reflex response.

5. Conclusion

An important conclusion derived from this study is a presence of different time – frequency distribution of energy related to both analyzed respiratory behaviors. Lower wavelet entropy is resulting from transient from eupneic activity to aspiration reflex. This decreasing could be explained as a changing degree of neural firing synchronization. Finally, these findings indicate specific processes at a level of central integration of aspiration reflex with potential impact on understanding the running of respiratory control mechanisms.

Acknowledgement

The author would like to thank to all co-workers (Department of Med. Biophysics, Comenius University, Slovakia) for participating in data recording.

References

[1] YANAURA, S., KAMEI, J., GOTO, K., HOSOKAWA, T., MISAWA, M., HUKUHARA, T.: *Analysis of Efferent Discharges of the Phrenic Nerve During the Cough Reflex,* Jpn J Pharmacol, 1982, 32: 795–801.

[2] TOMORI, Z., FUNG, L. M., DONIC, V., DONICOVA V., St JOHN W. M.: *Power Spectral Analysis of Respiratory Responses to Pharyngeal Stimulation in Cats: Comparisons with Eupnoea and Gasping.* J Physiol, 1995, 485: 551–559.

[3] KNOCIKOVA, J., POLIACEK, I., CAP, I., BARANI, H., JAKUS, J.: *Wavelet Analysis of Electrical Activities from Respiratory Muscles during Coughing and Sneezing in Anaesthetized Rabbits.* Acta Vet Brno, 2009, 78: 387–397.

[4] O'NEAL, M.H., SPIEGEL, E. T., CON, K. H., SOLOMON, I. C.: *Time-frequency Representation of Inspiratory Motor Output in Anesthetized C57BL/6 Mice in Vivo.* J Neurophysiol. 2005, 93: 1762–1775.

[5] TOMORI, Z.: *In: Cough and Other Respiratory Reflexes,* Vol. 12, Ed. BASEL, H.H. Karger, p. 356, 1979.

[6] TOMORI, Z., BENACKA, R., DONIC, V., TKACOVA, R.: *Reversal of Apnoea by Aspiration Reflex in Anaesthetized Cats.* Eur Respir J, 1991, 4: 117–1125.

[7] TOMORI, Z., POLIACEK I., KNOCIKOVA, J., JAKUS, J., DONIC, V.: *Distinct Generators of Aspiration and Expiration Reflexes, their Localizations, Mechanisms and Effects.* ERS Congress. – Berlin: [s.n.]. 2008, p. 144

[8] KIM M. S., CHO Y. CH., BERDAKH A., SEO H. D.: *Analysis of Brain Function and Classification of Sleep EEG using Daubechies Wavelet,* Sensors and Materials, 2008, 20: 1–14.

[9] COHEN, M. I., SEE W. R., CHRISTAKOS C. N., SICA A. L.: *High-frequency and Medium-frequency Components of Different Inspiratory Nerve Discharges and their Modification by Various Inputs.* Brain Res, 1987, 417: 148–152.

[10] NAJMI, A. H., SADOWSKI, J.: *The Continuous Wavelet Transform and Variable Resolution Time-frequency Analysis.* The Johns Hopkins APL Technical Digest, 1997, 18: 134–140.

[11] DAUBECHIES, I.: *The Wavelet Transform, Time-frequency Localization, and Signal Analysis.* IEE Trans Info Theory, 1990, 36: 961–1005.

[12] GOUPILLAUD, P., GROSSMANN, A., MORLET, J.: *Cycle-octave and Related Transforms in Seismic Signal Analysis.* Geoexploration, 1984, 23: 85–102.

[13] MALLAT, S.: *A Theory for Multiresolution Signal Decomposition: the Wavelet Representation.* IEEE Trans Patt Anal Mach Intell, 1989, 2: 674–693.

[14] MARCHENKO, V., ROGERS, R. F.: *Selective Loss of High-frequency Oscillations in Phrenic and Hypoglossal Activity in the Decerebrate Rat during Gasping.* Am J Physiol Regul Integr Comp Physiol, 2006, 291: R1414–R1429.

[15] PINCUS, S. M., GOLDBERGER, A. L.: *Physiological Time-series Analysis: What does Regularity Quantify?* Am J Physiol, 1994, 266: H1643–H1656.

[16] ZHENG, X., SUN, M., TIAN, X.: *Wavelet Entropy Analysis of Neural Spike Train.* Congress on Image and Signal Processing, 2008, 1: 225–227.

[17] DRAGOMIR, A., AKAY, Y., CURRAN, A. K., AKAY, M. *Investigating the Complexity of Respiratory Patterns during the Laryngeal Chemoreflex.* J Neuroeng Rehab, 2008, 5:17.

Yoshinori Takeichi – Marian Dzimko – Uwe Winkelmann *

THE EFFECTS OF MoO_3 POWDER LUBRICATION ON TRIBOLOGICAL PROPERTIES OF SLIDING PAIR EXPOSED TO HIGH TEMPERATURE

The effect of molybdenum trioxide MoO_3 powder on the tribological properties of sliding pair exposed to the temperature up to 700 °C was examined. The experiment showed that MoO_3 powder placed directly on the sliding surface of main tribological body influenced and reduced friction values of tested materials. Especially in a temperature range from 500 to 700 °C a clear minimum of friction coefficient around 600 °C was observed. The X-ray diffraction analysis of friction and wear tracks that appeared on specimens showed mixture of different elements which are the product generated during tribological processes at high temperature.

Keywords: aluminium bronze, molybdenum trioxide, high temperature, $Cu_3Mo_2O_9$, solid lubricant

1. Introduction

In this experimental work the tribological properties of solid lubricant coated stainless steel in contact with aluminium bronze under high temperature condition were studied. It is one of the capable materials which can be used at high temperature because of their thermal stability up to around 300 °C. However, at the temperature of over 400 °C, high friction coefficient and poor wear resistance are noted that why their lubricity properties are required to be further improved. On the other hand, the lubricity of many kinds of metal oxide at high temperature was studied. It was reported that MoO_3 showed superior lubricity at high temperature of about 700 °C [1], therefore it was expected that MoO_3 layer placed on the active friction surface enhances friction properties of aluminium bronze at high temperature.

2. Material and Sample Description

2.1 Molybdenum Trioxide MoO_3

Molybdenum trioxide MoO_3 is chemical compound. This compound is produced on the largest scale of any molybdenum compound. It occurs as the rare mineral molybdite. Its chief application is as an oxidation catalyst and as raw material for production of molybdenum metal. The oxidation state of molybdenum in this compound is +6 [2]. MoO_3 is produced industrially by burning molybdenum disulfide, the chief ore of molybdenum:

$$2\ MoS_2 + 7\ O_2 \rightarrow 2\ MoO_3 + 4\ SO_2. \quad (1)$$

The laboratory synthesis entails the acidification of aqueous solutions of sodium molybdate with perchloric acid [3]

$$Na_2MoO_4 + H_2O + 2\ HClO_4 \rightarrow$$

$$\rightarrow MoO_3(H_2O)_2 + 2\ NaClO_4. \quad (2)$$

The dihydrate loses water readily to give the monohydrate. Both are bright yellow in colour. Molybdenum trioxide dissolves slightly in water to give “molybdic acid.” In base, it dissolves to afford the molybdate anion [2]. In the gas phase, three oxygen atoms are double bonded to the central molybdenum atom. In the solid state, anhydrous MoO_3 is composed of layers of distorted MoO_6 octahedra in an orthorhombic crystal. The octahedra share edges and form chains which are cross-linked by oxygen atoms to form layers. The octahedra have one short molydenum-oxygen bond to a non-bridging oxygen [4]. Molybdenum trioxide has widespread industrial use. Its major use is as an additive to steel and other corrosion-resistant alloys. It is also used in the production of molybdenum products, as an industrial catalyst, a pigment, a crop nutrient, a component of glass, ceramics and enamels, a flame retardant for polyester and polyvinyl chloride resins, and as a chemical reagent. [5] Because of MoO_3 layered structure (see Fig. 1) MoO_3 is of interest for intensive tribological experimental investigations conducted at elevated and high temperatures. Physical and chemical properties are listed in Table 1.

Fig. 2 shows SEM image of MoO_3 powder used in experimental investigation of friction properties for the tribological pair composed of coated stainless steel specimen rubbed against aluminium bronze.

* **Yoshinori Takeichi[1], Marian Dzimko[2], Uwe Winkelmann[3]**
[1] Department of Mechanical Engineering, Toyohashi University of Technology, Toyohashi Aichi, Japan, E-mail: takeichi@mech.tut.ac.jp
[2] Faculty of Mechanical Engineering, Department of Design and Machine Elements, University of Zilina, Slovakia
[3] Institute for Mechanical Engineering (IfM), University of Applied Sciences Magdeburg-Stendal, Magdeburg, Germany

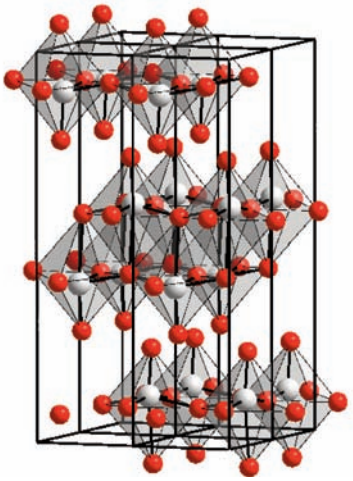

Fig. 1 Crystal structure of MoO_3 [2, 5]

Physical and chemical properties Table 1

Appearance	White or slightly yellow to slightly bluish powder
Odour	Odourless
Solubility	0.107 g/100 g water @ 18 °C
Density	4.69 g/cm^3, solid
Boiling Point	1150 °C
Melting Point	795 °C begins to sublime at 700 °C
Crystal structure	Orthorhombic

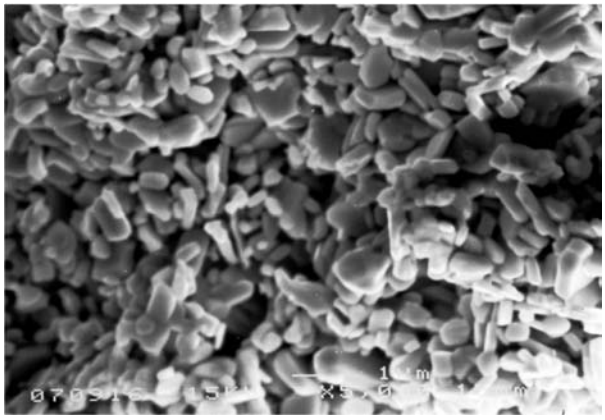

Fig. 2 SEM image of MoO_3 powder

2.2 Aluminium Bronze

Aluminium bronze, C6191 (JIS H 3250, Japanese Industrial Standards), with excellent fatigue resistance, corrosion resistance and wear resistance was chosen as material under test. The compositions of C6191 are shown in Table 2. It is copper based alloy which includes about 10 % aluminium and 3 to 5 % iron.

Compositions of aluminium bronze C6191 Table 2

Content	Cu	Al	Fe	Mn	Ni
Dens. %	81–88	8.5–11	3–5	0.5–2	0.5–2

2.3 Stainless Steel

Stainless steel, SUS304 (JIS G 4303) was used as a counterpart material for the friction test.

3. Specimens

It is well known that the oxide powders are difficult to adhere to metal surface. In the case of executed experiments the sample preparation was done as follows.

1. The sliding nominal surface of specimen was polished and then slightly sandblasted. The surface roughness (*Ra*) was measured with values around 1.0 μm.
2. The specimen was put into a glass container filled with acetone in which a defined amount of MoO_3 powder was mixed well. To achieve stable dispersion of MoO_3 powder in acetone, the ultrasonic vibration for 3 minutes was adapted. The container with the specimen was warmed up to 45 °C to evaporate acetone.

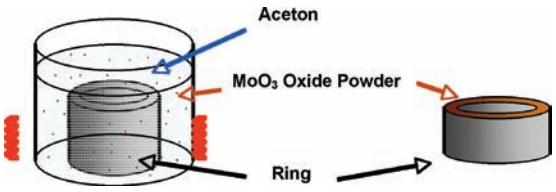

Fig. 3 Sample preparation procedure – coating

By this method finally the MoO_3 powder was uniformly accumulated on the sliding surface of the stainless steel specimen. In this way prepared specimens were used as a MoO_3 coated specimens. See Figs. 3 and 4.

3. The amount of accumulated MoO_3 powder on the specimen nominal surface was estimated by measuring the weight of the specimen before and after coating treatment. An average mass of adherent powder was controlled to be between 5 and 6 mg.

Stainless steel was used as a ring specimen and some of them were coated with the MoO_3 powder. The outer and inner diameter of the ring specimen was 20 and 15 mm, respectively.

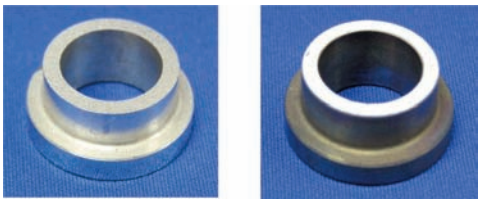

Fig. 4 Stainless steel ring specimen sandblasted uncoated and coated

Aluminium bronze was used as a disk specimen and its thickness was about 5 mm. Fig. 5 shows the form of an alloy rod and the prepared disc.

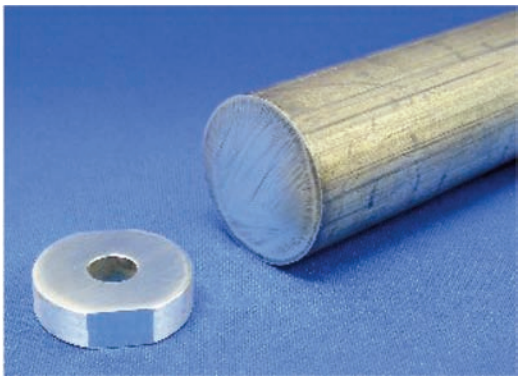

Fig. 5 Aluminium bronze disc specimen uncoated

4. Friction Test

To perform the friction test the ring-on-disk tribometer with a furnace in which the ring and disk specimens were mounted was used. The common load for all the experiment was set at 61.8 N which evocated to the median contact pressure of 0.46 MPa at the nominal surface of ring and disc. The ring specimen rotated at 60 rpm so the speed corresponded to the sliding speed of 55 mm/s. During performed experiments the approximate sliding distance reached about 200 m. For each temperature range starting at the room temperature (R.T.) and increasing step by step up to 700 °C new specimens were used. In this way the initial conditions for testing the high temperature lubrication ability of the coating remained the same for the whole experimental work. The tribometer was thoroughly described in [6, 7]. Figure 6 shows the plotted friction coefficient for the uncoated and coated specimens. It can be seen that the friction coefficient in the case of uncoated pair steadily increased from values around 0.25 to values of 0.72 corresponding to the increase of temperature from R.T. to 600 °C. By reaching the temperature of 700 °C the test was terminated because friction force exceeded the upper limit of this tribometer. The trend of the friction coefficient curve for the pair represented by MoO_3 coated stainless steel specimen and aluminium bronze can be divided into two different parts. The first part is characterised by a steady increase of values of the friction coefficient starting from 0.19 to 0.56 well corresponding to the increase of the temperature from R.T. to 400 °C. The second part is characterised trough a decrease of the coefficient of friction to the level of 0.44 with increase of the temperature up to 600 °C, followed by an increase of the friction coefficient again to the value of 0.57 by increasing temperature to 700 °C. This increase of the coefficient of friction around the 700 °C can be partly seen as the influence of beginning MoO_3 sublimation.

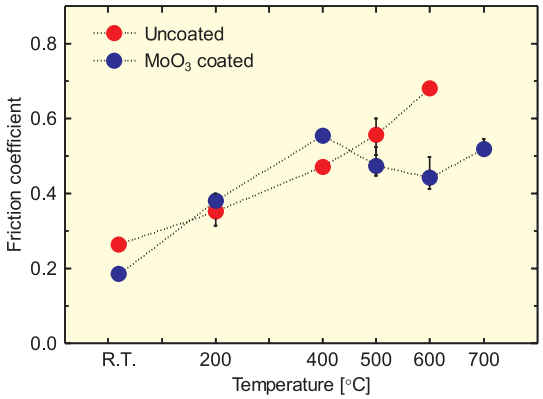

Fig. 6 Friction coefficient for the aluminium bronze disk and coated and uncoated MoO_3 stainless steel ring

From Figs. 7 and 8 the difference of adhesion appearing can be clearly seen. While for uncoated surfaces of both specimens a large amount of adhesion was observed (started at temperatures around 400 °C) for the MoO_3 coated stainless steel ring a large adhesion was observed only at temperature of 400 °C.

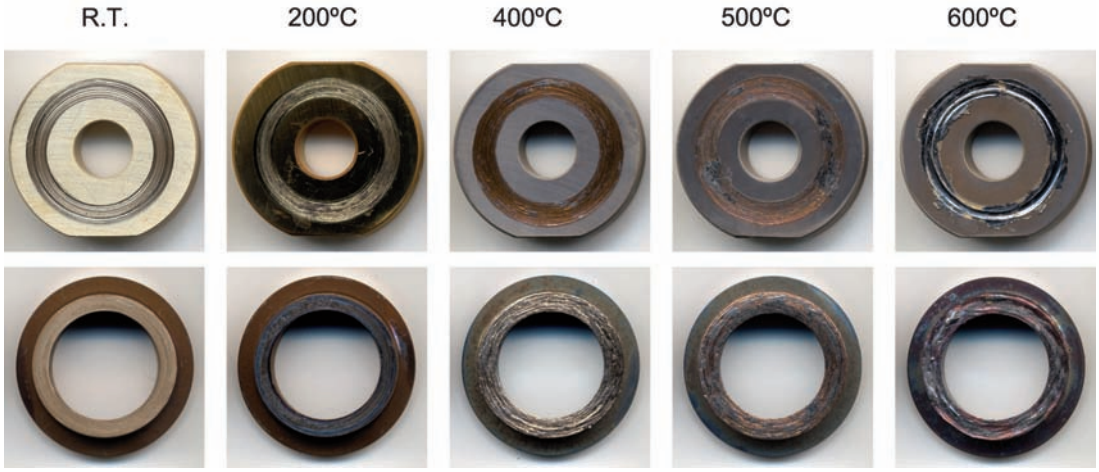

Fig. 7 Uncoated sliding surfaces of stainless steel ring and aluminium bronze disk after experiments at different temperatures

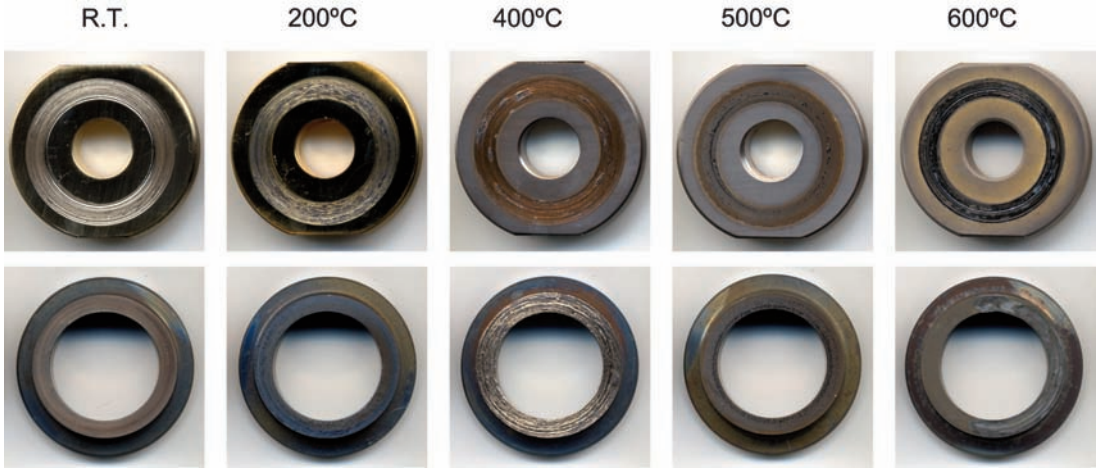

Fig. 8 MoO_3 powder coated sliding surfaces of stainless steel ring and aluminium bronze disk after experiments at different temperatures

5. X-ray Diffraction Analysis

For better understanding of friction and lubrication processes realised inside the contacted areas the XRD (X-ray diffraction) analysis was used. Some of the obtained results of the friction track on the aluminium bronze disk specimen, pressed and rubbed against the stainless steel ring coated with MoO_3, are presented in Fig. 9.

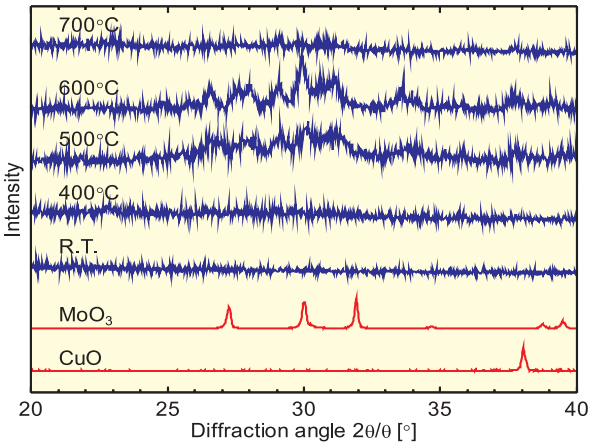

Fig. 9 XRD spectra obtained from the friction track resulting from temperatures R.T. to 700 °C of the aluminium bronze rubbed against MoO_3 coated stainless steel ring, for MoO_3 powder and for CuO powder

The diffraction peaks obtained from MoO_3 powder and CuO powder are also shown in the same figure as reference. To obtain significant data cobalt target X-ray source was chosen. This was necessary because aluminium bronze contains a few % irons as indicated in Table 2. In this range of diffraction angle, no peak of aluminium bronze could be registered. The analysis of specimen used and tested at higher temperatures of 500 and 600 °C shows several peaks with certain intensity. Fig. 9 shows that similar peaks are obtained also from the specimens tested at 700 °C, though the diffraction intensity is small. This comparison with the diffraction peaks obtained from MoO_3 and CuO powder leads to the conclusion that the peaks obtained from the friction track on the aluminium bronze are not resulting directly from MoO_3 or CuO powders.

In our previous work [6, 7] we conducted peak identification with the diffraction peak intensity in the database. The XRD spectrum obtained from the friction track of aluminium bronze slid against the MoO_3 coated ring at 600 °C and the diffraction peak intensity of $Cu_3Mo_2O_9$ in the database (JCPDS 01-070-1495) were compared. It can be suggested that the emerged material on the friction track of aluminium bronze is $Cu_3Mo_2O_9$ because the diffraction peak position and intensity of database are in good agreement with the obtained XRD spectrum. This can indicate selective transfer of interacting elements during tribological process at high temperatures. Also it can be considered that MoO_3 reduced friction of the tested pair by changing into $Cu_3Mo_2O_9$. Wahl et al. reported [8] that the ion-beam deposited amorphous Cu-Mo coating on alumina substrates showed low friction coefficient at 530 and 650 °C. They suggested that the amorphous Cu-Mo coating changed to crystalline oxide $CuMoO_4$ and that the softened oxides worked as high temperature lubricant. Though $Cu_3Mo_2O_9$ has different crystal structure from $CuMoO_4$, it is possible that $Cu_3Mo_2O_9$ having similar ingredient with $CuMoO_4$ is softened and shows superior lubricity at high temperature.

6. Conclusions

Molybdenum trioxide MoO_3 powder in the form of an adhered layer supplied to the sliding interface between aluminium bronze and stainless steel reduced the friction coefficient of both materials at high temperature. The effect of abrasion and adhesion shifted to the temperature range of 500 and 600 °C. Copper-molybdenum oxide, which was supposed to be $Cu_3Mo_2O_9$, was generated during the tribological contact process by sliding aluminium bronze and stainless steel in presence of MoO_3 powder.

Acknowledgement

This work was carried out under the support of The Ministry of Education, Culture, Sports, Science and Technology (MEXT), Japan. Grant-in-Aid for Young Scientists (B): 21760112 and by VEGA project V08-036-00 of the Ministry of Education, Slovak Republic.

Exchanges were realised with the support of the National scholarship scheme of the Ministry of Education and Slovak Academic Information Agency SAIA, s.r.o. Slovak Republic.

The authors wish to thank Mrs. Naoki Okamoto, and Mr. Takashi Chujyo, Masao Uemura, Ivan Havetta, Hirotomo Kobayashi for their support during the intensive experimental work.

References

[1] PETERSON, M. B., MURRAY, S. F., FLOREK, J. J.: *Consideration of Lubricants for Temperatures above 1000 °F*, ASLE Trans., 2/1960, 225–234.

[2] http://en.wikipedia.org/wiki/Molybdenum trioxide (02.02.2010)

[3] HEYNES, J. B. B.; CRUYWAGEN, J. J.: *Yellow Molybdenum(VI) Oxide Dihydrate,* Inorganic Syntheses, 1986, vol. 24, pp. 191. ISBN 0-471-83441-6

[4] WELLS, A.F.: *Structural Inorganic Chemistry, Oxford: Clarendon Press,* ISBN 0-19-855370-6, (1984)

[5] http://www.chinatungsten.com/Molybdenum/Molybdenum-Trioxide.html (02.20.2010)

[6] PETERSON, M. B., MURRAY, S. F., FLOREK, J. J.: *Consideration of Lubricants for Temperatures above 1000 °F*, ASLE Trans., 2/1960 225–234.

[7] TAKEICHI, Y., CHUJYO, T., OKAMOTO, N., HAVETTA, I., DZIMKO, M., UEMURA, M.: *Wear and Frictional Properties of Aluminium Bronze Alloy Lubricated with Molybdenum Trioxide at High Temperature,* Synopsis of 17th International Colloquium Tribology in Esslingen 2010, ISBN-Nr. 3-924813-80-9

[8] TAKEICHI, Y., CHUJYO, T., OKAMOTO, N., UEMURA, M.: *Effects of Molybdenum Trioxide on the Tribological Properties of Aluminium Bronze under High Temperature Conditions,* Japanese Society of Tribologists, Japan Tribology Online, vol. 4, 5/2009, pp. 135–139

[9] WAHL, K. J., SEITZMAN, L. E, BOLSTER, R. N., SINGER, I. L., PETERSON, M. B.: *Ion-Beam Deposited Cu-Mo Coatings as High Temperature Solid Lubricants,* Surface and Coating Technology, 89/1997, 245–251.

Iveta Kremenova – Marian Galovic *

PROPOSAL OF KEY FACTORS FOR USER-ORIENTED WEB APPLICATIONS

The paper deals with issues regarding the identification of key-factors for a successful creation of a user-oriented web application. Described are methods of identification, sources of information and contents of each category. The categories are Search, Display, Home Page and Navigation. The categories are broken-down into a table form. The paper also presents the results of several web applications testing based on new identified key factors. The testing was performed by the Department of Communications using a sample of web pages.

1. Introduction

The aims of the user-oriented application design are to satisfy all its users and to ensure their positive experience while using the application. Achieving these aims requires thorough understanding of the target user group needs. It is necessary to obtain the largest possible amount of information about the users, the tools they use at work, their working environment, as well as their expectations and requirements.

The users never spend more than 50 % of their on-line time with any web application. We can expect that, prior to using our web site, the users have visited several more or less similar sites. Each user is individual in their level of abilities to learn, gain experience and correlations from previous tasks. These characteristics determine the user's vision of how an application should work. Cumulation of users' experiences from their previous Internet work leads to subconscious comparing of the positive and negative characteristics of the web applications visited with the current application. Such cumulation of experiences brings about the user's increased requirements, demands and expectations of web applications. [1]

Procedures leading to the creation of user-oriented applications are referred to as User Centered Design (UCD), a proposal for the user. This approach consists of the steps, methods and tools that facilitate creators the prevention and/or problem-solving, especially in the usability of web application proposal. [8]

2. Theoretical background to tackle

User-oriented application is nowhere precisely defined. Many authors cover issues by one expression – usability, which of course covers a number of factors. Usability is also part of ISO 9241 – *Ergonomic requirements for office work with visual display terminals* (VDTs). *ISO 9241-11* definition refers to the origin of usability, which is described by users, their tasks and objectives, environment, equipment, and measuring by criteria of efficiency, performance and satisfaction. However, there is a summary of activities on which it is possible to determine what should be done in a specific situation to ensure the usability. *ISO 9241-11* provides recommendations on how to organize the usability evaluation during development process, which would become a guide or structure for developers. The scheme is flexible and can be universally used as a guide when designing applications. Responsibility for the decision of what usability consists is left up to the creator. [9]

With user-oriented design called user-centered or user-friendly also deals the *ISO 13407* standard – human-centred design process for interactive systems standard, which it describes as a multidisciplinary activity. It includes human factors and ergonomics knowledge and techniques to increase efficiency, productivity and user satisfaction [10].

Usability of web applications is a very important factor for ensuring the achievement of their success. Usability issues have to be integrated into their design and development applications. It is necessary to systematically define the requirements for usability, including methods of evaluation.

3. Identifying key factors for user-oriented web applications

Alike users' increasing requirements on web applications, the owners' expectations are growing of these applications, since the investment costs of their development increase gradually. The higher cost is induced by increasing complexity of the solution. In order for the web application to provide both the functions expected, and thus bring benefit for its user as well as for its owner, the appli-

* **Iveta Kremenova, Marian Galovic**
Department of Communications, Faculty of Operation and Economics of Transport and Communications, University of Zilina, Slovakia,
E-mail: Iveta.Kremenova@fpedas.uniza.sk

cation must meet certain criteria. Obviously, the owner can only benefit from the application if its users are satisfied. We have defined key factors, and identified them based on data and information from the following sources:

- consultations with experts in web application code development,
- consultations with experts in web graphic design,
- consultations with experts in web applicability and accessibility,
- consultations with experts from universities,
- observation of users working with the Internet,
- consultations with various user groups of web applications, and own research.

The first source for proposing the key factors was ***consultation with experts*** and *analysis of the data and information obtained* from the Prague marketing agency GFK Praha [11] The agency performs user tests and evaluates important web-application features with possible critical impact on the application's success with its users. GFK Praha utilizes quantitative research using eye-tracking technique, i.e. observing, recording and evaluating the human eye movement over particular applications and various tasks.

With such tests, the ideal number of tested persons is always crucial for individual tests. According to Jacob Nielsen and Thomas Landauer, the number of undetected problems in case of a test with test persons is as follows:

$$N(1-(1-L)^n)$$

where N is the total number of errors in the proposal, L is the number of errors detected by one Test Person (TP) during one test run, and n is the number of test persons (TPs). Empirically attested typical value L is 31 %, from which the following graph (Fig. 1) can be derived. [1]

Fig. 1 shows the web application errors detection in dependency on the number of test persons (TPs), where Test Person 1 (TP1) is able to detect 31 % of the errors. TP2 undergoing the same test repeats some of the errors but also detects more errors undetected by TP1. TP3 repeats the errors made by TP1 and TP2, and hence the number of newly detected errors decreases at a constant value of L. The more persons are used for the test; the lower is the contribution by every other person to the total number of detected errors. With five TPs it is possible to detect 85 % of errors.

Fig. 1 Dependency of error detection on the number of test persons

Therefore, the use of three to five TPs is suitable for continuous tests, thus ensuring that the test be quick, undemanding and sufficiently efficient. In case of so-called large tests, the number of TPs should be re-considered. However, Fig. 1 proves that no major improvement is brought about by TP numbers larger than 15.

Agency GFK Praha also performs quantitative research on a group of 8–12 users. Again, Fig. 1 shows that this number is adequate, and any further increase of the TP number would not bring a sufficient increase in the number of detected errors to balance the elevated cost of such testing, as it is time and money intensive.

A different way of testing web applications is to have them tested by an expert in the given field, according to pre-defined criteria, i.e. factors. Based on these factors, it is also possible to identify and propose changes needed for the application improvement. We attempted to propose such criteria on the basis of thorough analyses of multiple web sites.

Another information source for identification and proposal of key factors was ***verbal communication with users and questionnaire research***. The target groups were users with varying grades of education and level of computer and Internet skills. Each participant in the research works with the Internet every day at home and at work or school. Advanced and expert PC and Internet users use various versions of Opera or Mozilla Firefox browsers. Less skilled users prefer the browser under Windows operation system that is Internet Explorer of various versions. Participants in the research identified certain key requirements and errors for a user-oriented web application, and these were completed with the information from web application development experts. Fig. 2 shows 4 categories (groups) of factors and their sequence. The groups include individual factors affecting the given category.

Division of factors in 4 basic groups, based on following assumptions:

- *Search* – user must be able to find the web application in order to work with it,
- *Display* – user must see the web application displayed in order to work with it,

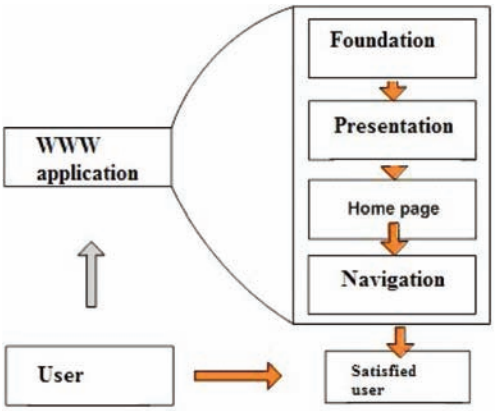

Fig. 2 Basic groups for classification of key factors

- *Home Page* – user must be able to use the home page in order to work with the web application without limitations,
- *Navigation* – user must be able to use a navigation feature in order to work with the web application without limitations.

Fig. 2 also show a graphic representation of the sequence of defined factor groups. Obviously, infringement of individual factors can be critical for the web application success in every phase.

Then, we defined other criteria for web application assessment, which are summarized in *Table 1*. The table includes factors considered as crucial, and classified into 4 basic groups.

Proposed key factors include ***measurable indices*** with primary or secondary effect on accessibility and on the following user's work with the web application.

Not included are immeasurable factors and factors regarding subjective opinions (judgment) by individual users and their habits. For example, the level of information architecture, complexity of the navigation, and applied colors (even if the contrast is measurable, each user subjectively perceives it differently). For these factors, a user test is more suitable.

Key factors of user-oriented web applications Table 1

Category	Criterion	Partial criterion
Search	Title	
	Correct reference nomenclature	
	Reference to similar pages	
	Proper URL name	
	Key words	
	Splash page	
	Frames	
	Google page rank	
Display	Browsers	IE 6
		IE 7
		Mozilla
		Firefox
		Opera
	Validity	HTML/XHTML
		CSS
	Display on PDA	Opera Mobile
		Internet Explorer Mobile
		Mobile page version
	Blind friendly – correct document flow	
	Resolution	800x600
		1024x768
		1280x1024
	Functionality	JS off
		Flash off
		CSS off
	Print version	
	Correct display of characters	
	Home page size	
HOME PAGE	Text alternative of the pictures (alt tribute)	
	Text size in IE - large/small	
	No reference opening in new windows	
	Error messages with wrong URL	Database
		Server
	HELP or FAQ prompt	
	Clarity of the Home page focus	
	Contact	
	Subpages under HOME PAGE, within navigation	
Navigation	Web application map	
	Search	present – absent
		diacritics
		internal
		advanced
	Use of standard controls	
	Return to HOME PAGE from every subpage	
	Navigation bar	
	Dictionary of terms	
	Operating via keyboard	
	Language version	

Individual factors and methods of their testing with selected web applications could be further characterized in details. Due to the vast scope of the issue, however, we do not present in this paper all the activities performed. More results are available in the above-mentioned doctorate thesis.

4. Experimental results of web applications testing

We can conclude that, based on the key factors identified, we performed tests at the Department of Communication of web applications with various subjects and contents. We tested selected applications by

- universities, ministries, regional capitals, organizations providing economic information, banks, postal administrations, electronic commerce, reporting (on-line newspapers, TV) and on-line information (time tables).

Fig. 3 presents the facts from the testing.

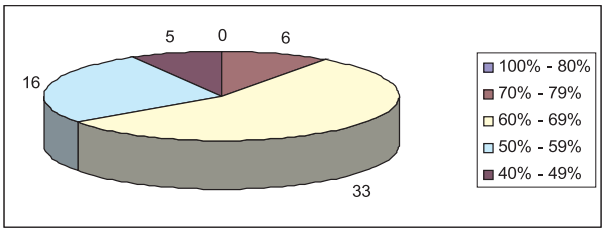

Fig. 3 Graphic representation of web application test results based on the key factors identified

The test included 60 web applications. None of the tested applications complied with 80 %–100 % of our identified factors (see Fig. 3). 33 of the tested web applications complied with 60%-69 % of the factors.

The variety of applications included in the research proves that they are used by various user groups. Therefore, no segmentation can be made in order to modify the key factors according to target groups. The results are not very attractive, as the key factors also included measurable factors not having a subjective characteristic of their assessment. Other drawbacks were detected utilizing a user test. The characteristics of such drawbacks varied substantially depending on individual target group and application. When identifying factors or methods for proposing applications according to selected segment of users, the users from a different segment are always disadvantaged. The subject of this paper, however is not such a segmentation, but rather to show the opportunity to establish the basis for further search, for example, in the field of changing the factors according to individual segments of users.

The test of selected applications with different focus on the defined factors proved that the issue of user-oriented applications is still an open and highly up-to-date one. This is apparent as none of the tested applications complies with all the defined criteria.

5. Evaluation and conclusions

Proposal of user-oriented web applications leads to the respect of the standards. The result will increase their accessibility, usability, compatibility with various platforms, browsers and terminal equipment [6].

In identifying factors or procedures for design applications according to the selected segment of users, will always be disadvantaged the user from another segment. Finally, this article may be said that scientific research has created a basis for further investigation, e.g. in the area of changing factors depending on different segments of users.

Creation of a modern web application does not consist only of designing the look and writing the source code for feature control. The proposal and creation of web applications constitute a complex process that includes multiple various activities. Graphic presentation design is only a part of the whole process chain, although it belongs to the basic and obvious criteria for evaluation of the application by its users. Even the best web application loses its value, if its content is poor or inadequate. Therefore, the content is always the most important feature.

As a field of further exploration we propose designing a methodology for testing factors with subjective influence on particular users of web applications.

References

[1] NIELSEN, J.: *Designing web Usability: The Practice of Simplicity,* SoftPress s.r.o. ISBN: 80-86497-27-5, 2002
[2] GALOVIC, M.: *Draft Creation to User-oriented Web Applications (in Slovak),* Doctoral thesis, EDIS ZU, Zilina, 2008
[3] KREMENOVA, I., ROSTASOVA, M.: *Marketing in Services (in Slovak)* Marketingovy informacny system EDIS–ZU, Zilina, ISBN 80-8070-358-2, 2005
[4] KREMENOVA, I., KOVACIKOVA, M.: *Designing of Technological Processes and Postal Services (in Slovak)*, EDIS, ZU, Zilina, ISBN 978-80-8070-904-4, 2008.
[5] GALOVIC, M., FABUS, J., KREMENOVA, I., *The mistakes of The Web presentations*, In: EUNIS 2005: 11th multidisciplinary conference: Manchester, 21.–24. June 2005: University of Manchester, 2005.
[6] GALOVIC, M., KREMENOVA I., FABUS, J.: *Ergonomic requirements for web sites,* In: EUNIS 2007: 13th multidisciplinary conference: Grenoble:France, 26. – 29. June 2007: Grenoble Universites, 2007.
[7] MURUGESAN, S.; GINIGE, A.: *Web Engineering: Introduction and Perspectives,* Southern Cross University and University of Western Sydney, Australia, 2005
[8] POWELL, T.: *Web Design: The Complete Reference – Second Edition,* The McGraw-Hill Companies, Inc. 2002, 0-07-222442-8
[9] ISO 9241 *Ergonomic requirements for office work with visual display terminals* (VDTs), 1998.
[10] ISO 13407 *Human-centred design processes for interactive systems,* 1999.
[11] www.gfk.sk/imperia/md/contnt/gfkslovakia/brochures/gfk_temax.maj.pdf.

Bohang Liu – Tong Zhang – Qingbing Li – Lijuan Wang *

AN TRAFFIC CONTROL METHOD BASED ON THE REAL-TIME DETECTOR DELAY

This paper puts forward a new single intersection control optimization method based on real-time delays by using the new technology of traffic detection. With this method the delay data (including parking delay, acceleration and deceleration delays) of vehicles and speed of the vehicles at the stop bar in every cycle can be detected real-timely. Thus, we can change the cycle length, total split, yellow time and all red time according to the analysis of the reasons of delay changes so as to optimize the traffic signal timing. Compared with traditional methods, this method can effectively deal with the situation that the traffic control scheme does not conform to the actual situation, resulting from the change of the road capacity under the conditions of rain, snow or fog, etc. The good effect can be seen in the example of this research as it effectively reduced delay by 19 % on average.

Keyword: real-time detector delay, traffic control, traffic control results

1. Introduction

As there are numerous factors influencing the results of traffic control which can not all be detected, only the parameters such as traffic volumes and the queue length are detected in the classic method, assuming that the parameters such as the road traffic capacity, friction coefficient, vehicle sight distance on road are constant. The classic method can adapt to most weather cases but rain, snow and fog, when the parameters like road friction coefficient are changed, the control optimization system can not be self-adjusted effectively to adapt to the variation of parameters, and so great vehicle delay will be caused. Since the influencing factors can not all be detected, a new single intersection traffic control optimization method is proposed from another standpoint in this paper relying mainly on the traffic control results (delay) of traffic control.

2. Research Status

A traffic control theory has developed for nearly one hundred years, and many encouraging achievements have been made. The upgrade of Anchorage Signal System was finished [1], the Adverse Weather Traffic Signal Timing was researched [2, 3, 4, 5], the SCOOT System has been studied [6, 7], and the SCATS System was studied [8, 9].The adaptive signal control strategies have been improved endlessly [10].

Despite of lots of achievements gained, the research is all about how to control traffic in accordance with the detected factors such as traffic volume and queue. As for the effect of the control, the system can not detect or evaluate it by itself, let alone changing its strategy according to the effect.

3. Contents

3.1. Basic Principle

The traditional control method can change a traffic control scheme by detector factors real-timely which influence the traffic control. Due to the diversity of the influencing factors and the real conditions, only the main factors (such as traffic volumes) can be detected. Adaptive control (as shown in Figure 1) is considered to be the most advanced traffic control form, which can only achieve the adoption to input (traffic flow), but can not adjust the control strategy according to the output (mainly delays) appropriately. This paper presents a new idea which detects the control results mainly (as shown in Figure 2). Its research contents include the detection of delay, analysis of the reasons which cause the delay and the adjustment of the control parameters.

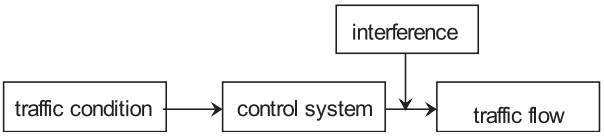

Fig. 1 Schematic diagram of the adaptive control

* **Bohang Liu[1,2], Tong Zhang[3,4], Qingbing Li[1,2], Lijuan Wang[1,2]**
[1] School of Traffic and Transportation, Shijiazhuang Railway Institute, Shijiazhuang, Hebei, China, E-mail: Liubohang@126.com
[2] Traffic Safety and Control Lab of Hebei Province, Shijiazhuang, Hebei, China
[3] The Road Bureau of Sanmenxia, Henna, China
[4] Sanmenxia polytechnic, Henna, China

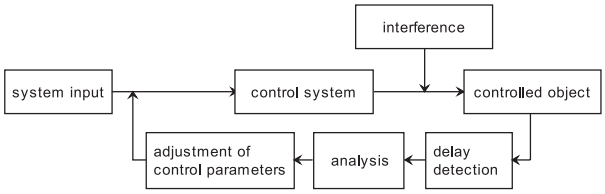

Fig. 2 Schematic diagram of traffic control based on the real-time detector delay

3.2 Detection of delay

The delay caused by control can be calculated with the following equation (1) according to the classic method.

$$d = d1 + d2 + d3 \tag{1}$$

In which, d is the delay caused by signal control, $d1$ is the average delay, $d2$ is the stochastic additional delay, $d3$ is the additional delay caused by the queuing of previous vehicles.

Normally, no previous vehicles should exist when vehicles arrive at the signal intersection, that is, the additional delay caused by the queuing of previous vehicles shouldn't exist. Thus the delay in every lane when designing an intersection can be calculated with the following equations:

$$d = d_1 + d_2 \tag{2}$$

$$d_1 = 0.5C(1-\lambda)^2/1 - \min[1,x]\lambda \tag{3}$$

$$d_2 = 900T\left[(x-1) + \sqrt{(x-1)^2 + T\frac{8eX}{CAP}}\right] \tag{4}$$

Where,

C – the time of cycle;
λ – split of the calculated lane;
x – saturation of the calculated lane;
CAP – capacity of the calculated lane (pcu/h);
t – time of duration of the analyzed interval, taken as 0.25h;
e – correction coefficient of the signal control in a single intersection;

The system delay is detected real-timely in this paper based on video traffic detector system, and Fig. 1 illustrates the principle:

As shown in Fig. 1, vehicles generally experience four steps and cause three delays in the signal intersection, the four steps are decelerating, parking, accelerating and leaving at a normal speed; the three delays are deceleration delay, parking delay and acceleration delay. Vehicles in the areas of D1 are decelerating and D2 are parking and D3 are accelerating. At present, the technology of traffic video detection is getting more mature with each passing day [11,12], which can track trajectory and real-time status of a single vehicle. The main steps are extracting background, identifying characteristics of a vehicle's contour and tracking the feature points and so on. The commonly used methods are Kalman filtering, hidden Markov filtering, extended Kalman filtering, Particle swarm filtering and others. As introduced in reference 13, the accuracy of tracking can reach 98 % in the case of no block and 92 % in the case of block. Therefore, the average delay is put forward in this paper on that basis, which can be expressed by equation (5):

$$d = \sum_{i=1}^{n} d_i/n = \sum_{i=1}^{n}(t_{i1} - t_{i2})/n \tag{5}$$

In which,

d – the average delay of vehicles at the signal intersection
d_i – the actual delay of every vehicle;
t_{i1} – time for the vehicle to travel from a picture edge of video detection to the stop bar;
t_{i2} – time for the vehicle to travel from a picture edge of video detector to the stop bar under ideal conditions;
n – number of vehicles;

The headway used in calculating road capacity can be calculated with the equation below:

$$t_i = \sum_{j=3}^{n-m-1} t_j/(n-3-m) \tag{6}$$

Where,

t_i – the average time for the other vehicles except the first two vehicles to pass; that is the headway
t_j – the headway between vehicles J and $J+1$ in this lane and this cycle;
n – the number of vehicles passing a lane in one cycle;

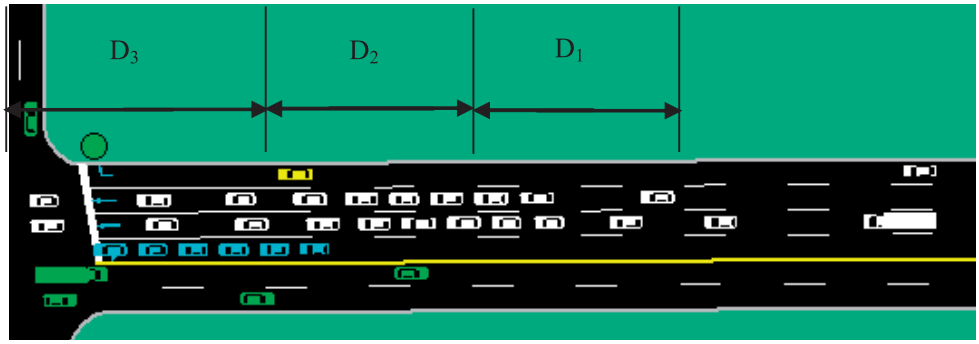

Fig. 3 Principle diagram of delay generation

m – the number of vehicles passing separately at the later period of the green light; the headway can't be used in calculating road capacity in this period;

The speed of vehicles passing the stop bar can be achieved by calculating the average while the acceleration and deceleration parameters can be achieved by tracking.

3.3. Analysis of the causes for delay

The delay changes can result from two reasons, (1) the traffic volumes changes; (2) changes of other factors.

It is the most common situation that the traffic delay changes due to the change of traffic volumes, which can be dealt with by classic adaptive control. There are many processing methods, like TRB method, the TRRL method and the United States HCM manual method. The algorithm is very mature and widely used and we don't list them individually.

It is indicated that there are other factors affecting traffic operation in the intersection, if the traffic volumes doesn't change much but the detected delay changes dramatically. Usually they are rain, snow or fog, and these adverse weathers can be considered as having effect on the capacity of entrance lanes vehicle speed and acceleration.

The classical control method is used in the first situation, therefore only the second situation is discussed in the content of 3.4 and 3.5.

3.4 Analysis of signal timing Principle

Figure 4 illustrates the adjustment principle of the traffic control system mentioned in 3.3, which is under the second condition. Namely, if the detected real-time delay increases, in most cases, it is because the weather factors make the road friction coefficient and sight distance of the driver decrease, thus the phase intervals and the cycle are impacted.

(1) Phase Change Interval

$$y + r = \delta + \frac{v}{2a + G} + \frac{w + L}{v} \tag{8}$$

Where $Y + AR$ = Sum of the yellow and all red time intervals T = perception/reaction time of driver in seconds (typically taken as 1.0 second) V = approach speed in feet per second a = deceleration rate t per second w = Width of intersection L = length of vehicle gr = approach grade, percent of grade divided by 100 (add for up-grade and subtract for downgrade)

Because the length of the intersection is not changed and the vehicle speed decreases, the phase change interval will be increased.

(2) Cycle:

$$c = \frac{1.5L + 5}{1 - Y} \tag{9}$$

Where, c is the signal cycle; L is the lost time; and Y is the saturation;

The equation to calculate the lost time is as follows:

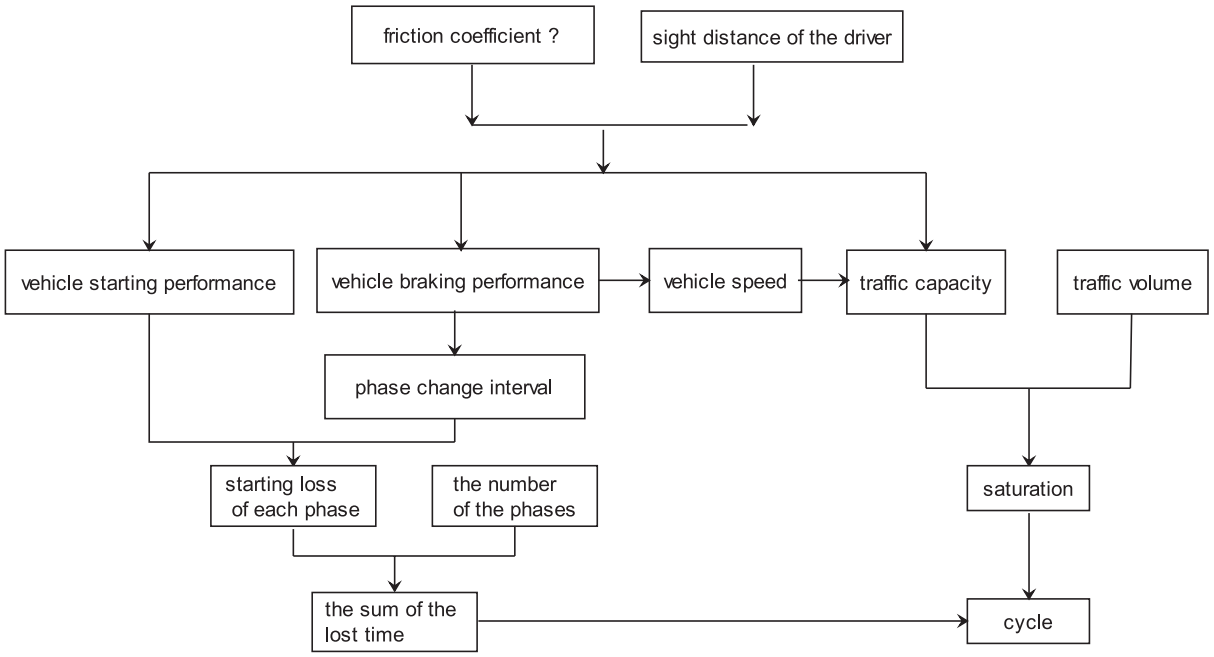

Fig. 4 Relationship between friction coefficient and signal timing parameters

$$L = \sum(l + I - A) \quad (10)$$

In the equation: L is total lost time in one cycle (s); l is startup lost time; I is the phase change interval; and A is the yellow time. A

Y is the accumulation of each phase saturation;

The others are the same as above.

The cycle should be adjusted to bigger due to the increased phase change interval.

3.5 Adjustment of Control Parameters

According to the above analysis, the adjustment plan of the Interval time of the green and the cycle can be confirmed when we can identify when the detected real-time delay increases.

After the timing scheme has been recounted as above, it will be applied in the intersection control and the delay of the new scheme will be detected. The detected delay will decrease in most cases. If the delay increases or if there is no obvious change it means that the analysis of the cause of delays is wrong. The vehicle delay variation may be caused by a pedestrian or a non-motor vehicle. It should be re-analyzed and re-timed.

4. Case Analysis

One intersection in Shijiazhuang City of China was taken as an example to be analyzed. Traffic flow in this intersection was stable in the experiment, and the basic situation of traffic flow in each entrance is shown in Table 2. In the morning of the experiment the weather was normal, the pavement was dry, the pavement friction coefficient was 0.8 and the normal scheme was used in traffic signal, as shown in Table 3. After snow in the afternoon, the traffic control departments used snow melting agents in the trunk road (Yuhua Road) and the road friction coefficient was 0.6, while the secondary road (Tiyu Street) was not processed and the road friction coefficient was 0.4. The system used the algorithm presented in this paper. Several cycles detected showed that after the snow, with a similar number of vehicles, the real-time detection of the vehicles' delay increased. Judging that the road capacity and the speed of vehicles may change, the system calculated the headway and the speed of the vehicles at the stop bar. The new traffic signal timing programs are generated after a re-calculated cycle, total split, the interval of yellow time and green time as shown in Table 3. Table 4 demonstrates effect comparisons among the cases. Obviously, the delay caused by the scheme offered in this paper is shorter than using conventional timing scheme under the conditions of snow. The experiment of the timing scheme adjustment is manual due to limited experimental conditions.

Basic situation of the intersection — Table 2

Entrances	East entrances	West entrances	South entrances	North entrances	Sum
Volume of traffic	2160	2090	452	502	5204
Number of lanes	4	4	2	2	12
Capability	4187.00	4215.00	2178.00	2098.00	12678.00
v/c	0.52	0.50	0.21	0.24	–

Adjustment of control parameters — Table 1

1	Interval time of the green	First	Detected headway increases	Interval increases
			Detected headway decreases	Interval decreases
			Not the above situations	No adjustment
		Second	Vehicle delay in the intersection increases after the last adjustment	Adjustment in the opposite direction
			Vehicle delay decreases in the intersection after the last adjustment	Adjustment in the same direction
			Vehicle delay increases in the intersection after the adjustment in both directions	Stop adjustment
2	Cycle	First	The headway or the traffic volume increases	Cycle increases
			The headway or the traffic volume decreases	Cycle decreases
			Not the above situations	No adjustment
		Second	Vehicle delay in the intersection increases after the last adjustment	Adjustment in the opposite direction
			Vehicle delay decreases in the intersection after the last adjustment	Adjustment in the same direction
			Vehicle delay decreases in both directions	Stop adjustment

Signal timing scheme — Table 3

Entrances	First phase time (traffic in east and west)	Yellow time	All red time	Second phase (traffic in south and north)	Yellow time	All red time	Cycle
Under the normal timing scheme	35	3	0	16	3	0	57
Timing scheme under the condition of snow	89	3	1	41	3	1	138

Delay comparison of the intersection Table 4

Delay per vehicle	East entrances	West entrances	South entrances	North entrances	Average
Under normal condition	8.1	7.2	14.7	17.9	9.4
Normal scheme under the condition of snow	23.6	20.2	56.4	45.2	27.4
This scheme under the condition of snow	19.9	16.1	25.9	27.6	22.3

5. Conclusion

This paper puts forward a new single intersection control optimization method based on real-time delays, by using the new technology of traffic detection. With this method the delay data (including parking delay, acceleration and deceleration delay) of vehicles and the speed of the vehicles at the stop bar in every cycle can be detected real-timely. We can thus change the cycle length, total split, yellow time and all red time according to the analysis of the reasons of delay changes, so as to optimize the traffic signal timing. This method breaks away with the traditional one which detects the influencing factors one by one. It detects the control results directly and analyzes the reasons of how they come into being. Compared with traditional methods, this method can effectively deal with the situation that the traffic control scheme does not conform to the actual situation resulting from the change of the road capacity under the conditions of rain, snow, fog, etc. The good effect can be seen in the example of this research as it effectively reduced delay by 19 % on average.

References

[1] LOCHMUELLER, B. and Associates: *Anchorage Signal System Upgrade-Final report.* 1995

[2] MAKI, P. J.: *Adverse Weather Traffic Signal Timing,* P.E. 69th Annual Meeting of the ITE, Las Vegas, 1999

[3] PARSONSON, P. S.: *Flashing Operation and Signal Timing for Adverse Weather,* NCHRP Synthesis of Highway Practice, 1992, pp. 46–47.

[4] BOTHA, J. L., KRUSE, T. R.: *Flow Rates at Signalized Intersections under Cold Winter Conditions,* J. of Transportation Engineering, 1992, pp. 439–450.

[5] GILLAM, W. J., WITHILL, R. A.: *UTC and Inclement Weather Conditions,* IEE Conference, 1992, pp. 85–88

[6] HUNT, P. B., ROBERTSON, D. I., BRETHERTON, R. D., WINTON R. I.: *SCOOT-A Traffic Responsive Method of Coordinating Signals;* TRRL Report LR1014, Crowthorne, 1981

[7] HANSEN, B., MARTIN, P., PERRIN, J.: *SCOOT Real-Time Adaptive Control in a CORSIM Simulation Environment,* Transportation Research Board (TRB), 2000 Annual Conference, Washington, D. C., January 2000 (accepted for Publication in TRR)

[8] LOWRIE, P. R.: *SCATS, Sydney Co-ordinated Adaptive Traffic System, A Traffic Responsive Method of Controlling Urban Traffic*, Roads and Traffic Authority Sydney, NSW, Australia, 1990.

[9] LOWRIE, P. R.: *The Sydney Co-ordinated Adaptive Traffic System Principles, Methodology Algorithms,* Int. conference on Road Traffic Signaling, London, 1982, pp. 67–70.

[10] GARTNER, N. H., STAMATIADIS, C., TARNOFF, P. J.: *Development of Adaptive Signal Control Strategies for Intelligent Transportation Systems: A Multilevel Design*, Presented at the 74th Annual meeting of the Transportation Research Board, 1995.

[11] KOLLER D, WEBER J, MALIK J.: *Robust Multiple Car Tracking with Occlusion Reasoning,* Proc. of European Conference on Computer vision (ECCV), Berlin-Heidelberg; Springer-Verlag, 1994, pp. 189–196

[12] ROMBERG, J. K, CHOI, H, BARANIUK, R. G.: *Bayesian Tree-structured Image Modeling Using Wavelet-domain Hidden Markov Models*, IEEE Transactions on Image Processing, 2001, pp. 1056–1068.

COMMUNICATIONS – Scientific Letters of the University of Zilina
Writer's Guidelines

1. Submissions for publication must be unpublished and not be a multiple submission.
2. Manuscripts written **in English language** must include **abstract** also written in English. The submission should not exceed **10 pages** with figures and tables (format A4, Times Roman size 12). The **abstract** should not exceed 10 lines.
3. Submissions should be sent: **by e-mail** (as attachment in application MS WORD) to one of the following addresses: *komunikacie@uniza.sk* or *holesa@uniza.sk* or *vrablova@uniza.sk* or *polednak@fsi.uniza.sk* **with a hard copy** (to be assessed by the editorial board) **or on a CD** with a hard copy to the following address: Zilinska univerzita, OVaV, Univerzitná 1, SK-010 26 Zilina, Slovakia.
4. Abbreviations, which are not common, must be used in full when mentioned for the first time.
5. Figures, graphs and diagrams, if not processed by Microsoft WORD, must be sent in electronic form (as GIF, JPG, TIFF, BMP files) or drawn in contrast on white paper, one copy enclosed. Photographs for publication must be either contrastive or on a slide.
6. References are to be marked either in the text or as footnotes numbered respectively. Numbers must be in square brackets. The list of references should follow the paper (according to **ISO 690**).
7. The author's exact **mailing address of the organisation where the author works, full names, e-mail address or fax or telephone number,** must be enclosed.
8. The editorial board will assess the submission in its following session. In the case that the article is accepted for future volumes, the board submits the manuscript to the editors for review and language correction. After reviewing and incorporating the editor's remarks, the final draft (before printing) will be sent to authors for final review and adjustment.
9. The deadlines for submissions are as follows: September 30, December 31, March 31 and June 30.

COMMUNICATIONS

SCIENTIFIC LETTERS OF THE UNIVERSITY OF ZILINA
VOLUME 12

Editor-in-chief:
Prof. Ing. Pavel Polednak, PhD.

Editorial board:
Prof. Ing. Jan Bujnak, CSc. – SK
Prof. Ing. Otakar Bokuvka, CSc. – SK
Prof. RNDr. Peter Bury, CSc. – SK
Prof. RNDr. Jan Cerny, DrSc. – CZ
Prof. Eduard I. Danilenko, DrSc. – UKR
Prof. Ing. Branislav Dobrucky, CSc. – SK
Prof. Dr. Stephen Dodds – UK
Dr. Robert E. Caves – UK
Dr.hab Inž. Stefania Grzeszczyk, prof. PO – PL
Prof. Ing. Vladimír Hlavna, PhD. – SK
Prof. RNDr. Jaroslav Janacek, CSc. – SK
Prof. Ing. Hermann Knoflacher – A
Dr. Ing. Helmut Konig, Dr.h.c. – CH
Dr. Zdena Kralova, PhD. – SK
Prof. Ing. Milan Moravcik, CSc. – SK
Prof. Ing. Gianni Nicoletto – I
Prof. Ing. Ludovít Parilak, CSc. – SK
Ing. Miroslav Pfliegel, CSc. – SK
Prof. Ing. Pavel Polednak, PhD. – SK
Prof. Bruno Salgues – F
Prof. Andreas Steimel – D
Prof. Ing. Miroslav Steiner, DrSc. – CZ
Prof. Ing. Pavel Surovec, CSc. – SK
Prof. Josu Takala – SU
Doc. Ing. Martin Vaculik, CSc. – SK

Address of the editorial office:
Zilinská univerzita
Office for Science and Research
(OVaV)
Univerzitna 1
SK 010 26 Zilina
Slovakia
E-mail: komunikacie@nic.uniza.sk,
polednak@fsi.uniza.sk

Each paper was reviewed by two reviewers.

Journal is excerpted in Compendex and Scopus

It is published by the University of Zilina in
EDIS – Publishing Institution of Zilina University
Registered No: EV 3672/09
ISSN 1335-4205

Published quarterly

Single issues of the journal can be found on:
http://www.uniza.sk/komunikacie